



12-2002

## Numerical simulation of freezing shear driven rivulets using an enthalpy method formulation

Clark G. Wiberg  
*University of Tennessee*

Follow this and additional works at: [https://trace.tennessee.edu/utk\\_graddiss](https://trace.tennessee.edu/utk_graddiss)

---

### Recommended Citation

Wiberg, Clark G., "Numerical simulation of freezing shear driven rivulets using an enthalpy method formulation. " PhD diss., University of Tennessee, 2002.  
[https://trace.tennessee.edu/utk\\_graddiss/6331](https://trace.tennessee.edu/utk_graddiss/6331)

This Dissertation is brought to you for free and open access by the Graduate School at TRACE: Tennessee Research and Creative Exchange. It has been accepted for inclusion in Doctoral Dissertations by an authorized administrator of TRACE: Tennessee Research and Creative Exchange. For more information, please contact [trace@utk.edu](mailto:trace@utk.edu).

To the Graduate Council:

I am submitting herewith a dissertation written by Clark G. Wiberg entitled "Numerical simulation of freezing shear driven rivulets using an enthalpy method formulation." I have examined the final electronic copy of this dissertation for form and content and recommend that it be accepted in partial fulfillment of the requirements for the degree of Doctor of Philosophy, with a major in Mechanical Engineering.

Roy J. Schulz, Major Professor

We have read this dissertation and recommend its acceptance:

Accepted for the Council:

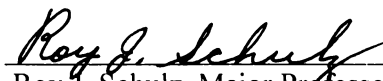
Carolyn R. Hodges

Vice Provost and Dean of the Graduate School

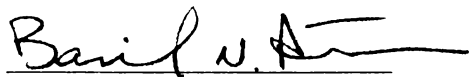
(Original signatures are on file with official student records.)

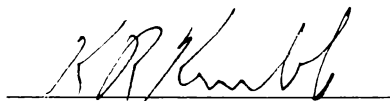
To the Graduate Council:

I am submitting herewith a dissertation written by Clark George Wiberg entitled "Numerical Simulation of Freezing Shear Driven Rivulets Using an Enthalpy Method Formulation." I have examined the final paper copy of this dissertation for form and content and recommend that it be accepted in partial fulfillment of the requirements for the degree of Doctor of Philosophy, with a major in Mechanical Engineering.

  
Roy J. Schulz, Major Professor

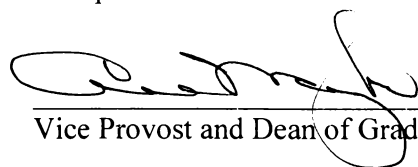
We have read this dissertation  
and recommend its acceptance:

  
\_\_\_\_\_

  
\_\_\_\_\_

  
\_\_\_\_\_

Accepted for the Council:

  
Vice Provost and Dean of Graduate Studies



NUMERICAL SIMULATION OF FREEZING SHEAR  
DRIVEN RIVULETS USING AN ENTHALPY  
METHOD FORMULATION

A Dissertation  
Presented for the  
Doctor of Philosophy  
Degree  
The University of Tennessee, Knoxville

Clark George Wiberg  
December 2002

## **DEDICATION**

This dissertation is dedicated to my angel wife, Janell, who has been like the Polar Star throughout this journey.

## ACKNOWLEDGEMENTS

I wish to express gratitude to many of the faculty who exercised skill in teaching the principles of many subjects associated with Mechanical Engineering. I thank my Doctoral Committee for their encouragement and assistance in the pursuit of this degree. A special thanks is due Dr. Schulz, my Major Professor, for his patience, encouragement and introducing me to world of ice accretion analysis and modeling.

I thank the Arnold Engineering and Development Center (AEDC), Arnold Air Force Base, for providing the funding for this research. I am grateful to Dr. Dennis Lankford and Tom Tibbals of AEDC for their guidance and mentoring ways. A special thanks is also given to Mr. Tom Irvine and his associates of the Icing Research Branch at NASA Glenn Research Center for graciously assisting and allowing me to conduct experimental work in the Icing Research Tunnel.

Deep gratitude is extended to my family, both immediate and extended, for their unwavering love, support, encouragement and thoughtfulness. A particular expression of love and appreciation is extended to my angel wife, Janell, for her steady and unwavering love, support and faith in me. Additionally, my Heavenly Father, towards whom I have a deep sense of gratitude, has abundantly blessed me with understanding and perspective in all my worthy endeavors.

## ABSTRACT

A numerical simulation of freezing shear driven rivulets is presented herein. The physics of the freezing process is captured in the simulation through application of the “enthalpy method”; a formulation well suited for the Stefan class of problems. The associated system of fully implicit finite difference equations was solved using the Gauss-Seidel iterative technique. The enthalpy method formulation is first applied to the case of a “stationary” freezing rivulet, but with a convective boundary at the free surface. The “stationary” simulation is utilized as a subset of the more complex “traveling”, or shear driven, simulation. The freezing process of shear driven rivulets was divided into three distinct modes based upon macro-scale observations of freezing rivulet flow on a NACA 0012 airfoil. From such observations, a non-dimensional empirical parameter was developed which establishes the bulk rivulet halt criterion for a freezing rivulet during runback.

An experimental simulation of freezing shear driven rivulet flow was conducted, and the results compared to their numerical counterparts to facilitate a validation of the numerical simulation with its accompanying physical models. The experimental effort simulated freezing shear driven rivulet runback on a flat plate. The experiment was conducted in the Icing Research Tunnel (IRT) at NASA Glenn Research Center; a facility wherein environmental parameters can be effectively changed and monitored with exceptional accuracy.



The key features of bulk rivulet halt distance, the distance at which the frozen portion of the rivulet front halts during runback, and the extension of the rivulet downstream until the bulk rivulet is completely frozen were studied and compared. The comparative results reveal reasonably good agreement between the numerical and experimental simulations. Herein, the numerical halt distance predictions vary from the experimental results by an average of 27%, where the range of variation is 0.9% to 45%. Given the complexities associated with the simulation of shear driven freezing rivulet runback, and the necessity to apply simplifying assumptions to render the problem manageable, agreement within 50 % between predicted and measured results is considered reasonable. In addition to the reasonable correlation between numerical predictions and experimental results for the rivulet front halt distances, other phenomena included in the numerical models were experimentally observed.

A study revealed the primary effect that the wall temperature and the freestream velocity have on the extent of the bulk rivulet travel. The wall temperature affects the freezing potential (Stefan number), while the freestream velocity affects the shear force driving the rivulets.

## TABLE OF CONTENTS

CHAPTER I: INTRODUCTION AND BACKGROUND .....	1
Research Objective .....	4
Approach.....	4
Ice Accretion Background .....	6
Ice Accretion Process and Phases .....	6
Glaze Ice Accretion Zones.....	9
Surface Water Behavior Considerations.....	14
CHAPTER II: FUNDAMENTALS OF THE FREEZING RIVULET MODEL .....	17
Freezing Rivulet Geometry .....	17
Rivulet Formation and Resultant Geometry .....	18
Physical Conditions and Assumptions.....	19
The Stefan Problem.....	22
The Enthalpy Method .....	24
Advantages of the Enthalpy Method.....	27
CHAPTER III: EXPERIMENTAL SIMULATION OF FREEZING SHEAR DRIVEN RIVULETS .....	31
Experimental Simulation Configuration .....	32
Test Apparatus .....	32
Instrumentation .....	38
Test Parameters .....	39
Test Procedure .....	41
Rivulet Contact Angle Determination .....	43
Experimental Results.....	44
Conclusions and Remarks.....	48
CHAPTER IV: STATIONARY FREEZING RIVULET NUMERICAL SIMULATION .....	52
Computational Formulation.....	52
Computational Domain.....	53
Primary Model Assumptions .....	55
Governing Equations .....	59
Physical Domain .....	59

Computational Domain.....	63
Discretization and Numerical Solution Technique .....	65
Discretization .....	67
Numerical Solution Technique .....	72
Thermo-Physical Properties.....	79
Freezing Stationary Rivulet Results.....	80
Phase-Change Front Propagation.....	80
Surface Heat Transfer Rate Results .....	90
Remarks .....	97
CHAPTER V: FREEZING RIVULET RUNBACK NUMERICAL SIMULATION... 101	
Freezing Rivulet Runback Modes.....	101
Mode #1 – Freezing Rivulet Runback without Frozen Deposition .....	102
Mode #2 – Extension of Liquid Mass Beyond Halted Frozen Mass until Rivulet Leading Edge Completely Freezes .....	105
Mode #3: Liquid Mass Extension Beyond Halted Frozen Mass until Choke Condition is Achieved.....	106
Governing Equations .....	109
Discretization of Governing Equations.....	111
Rivulet Velocity Profile .....	114
Phase-Change Cell Thermal Resistances.....	116
Freezing Rivulet Runback Results.....	118
Phase-Change Front Profiles at Halt.....	119
Rivulet Runback Length .....	127
Comparison of Predicted and Experimental Results .....	129
Parametric Study Results .....	130
Conclusions.....	137
Summary .....	138
CHAPTER VI: CONCLUDING REMARKS .....	139
LIST OF REFERENCES .....	143
APPENDIX.....	147
APPENDIX: COEFFICIENTS AND INTEGRAL FUNCTIONS – ANALYTICAL RIVULET VELOCITY FIELD .....	148
VITA.....	150

## LIST OF TABLES

Table	Page
Table 1. Experimental Bulk Rivulet Halt Distances.....	49
Table 2. Rivulet Conditions and Parameters for the Stationary Rivulet Cases .....	81
Table 3. Rivulet Conditions and Parameters for the Runback Rivulet Cases.....	119
Table 4: Halt Length, Frozen Fraction and Equivalent Mass Length of Freezing Rivulet Runback for Simulation Cases.....	128
Table 5. Comparison of Numerical and Experimental Bulk Rivulet Halt Distances ....	129
Table 6: Parametric Results for the Wall Temperature, $T_w$ .....	131
Table 7. Parametric Results for the Freestream Temperature, $T_{inf}$ .....	132
Table 8: Parametric Results for Freestream Velocity, $U_{inf}$ .....	133

## LIST OF FIGURES

Figure	Page
Figure 1. Glaze Ice Accretion Smooth/Rough Zone Transition Front.....	11
Figure 2. Typical Glaze Ice Shape Accretion Zones on a 1-in. Cylinder for a 2-min. Exposure .....	13
Figure 3. Rivulet Runback on a B1-B Inlet Vane in the Icing Research Tunnel (IRT) at NASA Glenn Research Center.....	16
Figure 4. Rivulet Cross-section and Fundamental Geometric Parameters .....	21
Figure 5. Moving Phase-Change Interface for a 1-D Stefan Problem .....	23
Figure 6. Flat Plate Test Article in the IRT Test Section.....	34
Figure 7. Flat Plate Test Article in the IRT Test Section– Close-up of Supply Tubes....	34
Figure 8. Interface Between the Rivulet Water Supply Tubes and the Flat Plate .....	35
Figure 9. Schematic of Valve System with Modified Atomizer Head .....	36
Figure 10. Rivulet Water Reservoir, Ice Bath and Associated Plumbing.....	37
Figure 11. Flowmeter Panel – Flowmeter in each Rivulet Water Supply Line .....	40
Figure 12. Rivulet 1-C at Rivulet Front Halt Distance .....	45
Figure 13. Rivulet 3-C at Rivulet Front Halt Distance .....	45
Figure 14. Rivulet 4-C at Rivulet Front Halt Distance .....	46
Figure 15. Rivulet 7-A at Rivulet Front Halt Distance .....	46
Figure 16. Rivulet 7-C at Rivulet Front Halt Distance .....	47
Figure 17. NACA 0012 Rivulets Running Back – Halt and Extension Phenomena .....	47
Figure 18. Rivulet - Physical Domain (Contact Angle, $\beta = 38^\circ$ ).....	54
Figure 19. Rivulet - Computational Domain .....	56
Figure 20. Computational Domain with Discretized Cell Index Notation .....	66
Figure 21. Five-Cell Computational Stencil With Gauss-Seidel Iterative Notation.....	73
Figure 22. Graphical Representation of Equation (4.34).....	77
Figure 23. Freezing Stationary Rivulet Solution Flow Chart .....	78
Figure 24. Case 1-C Stationary Freezing Rivulet .....	82
Figure 25. Case 3-C Stationary Freezing Rivulet .....	83
Figure 26. Case 4-C Stationary Freezing Rivulet .....	84
Figure 27. Case 7-C Stationary Freezing Rivulet .....	85
Figure 28. Case 9-C Stationary Freezing Rivulet .....	86
Figure 29. Case 3-C_a: Case 3-C Rivulet With Adiabatic Wall Boundary Condition....	87
Figure 30. Case 3-C_b: Case 3-C Rivulet With No Mass Transfer (Evaporation/Sublimation) At The Free Surface .....	88
Figure 31. Case 1-C Free Surface Heat Flux .....	91
Figure 32. Case 1-C Wall Heat Flux.....	91
Figure 33. Case 3-C Free Surface Heat Flux .....	92
Figure 34. Case 3-C Wall Heat Flux.....	92
Figure 35. Case 4-C Free Surface Heat Flux .....	93

Figure 36. Case 4-C Wall Heat Flux.....	93
Figure 37. Case 7-C Free Surface Heat Flux .....	94
Figure 38. Case 7-C Wall Heat Flux.....	94
Figure 39. Case 9-C Free Surface Heat Flux .....	95
Figure 40. Case 9-C Wall Heat Flux.....	95
Figure 41. Case 1-C Normalized Heat Flux Comparison.....	98
Figure 42. Case 3-C Normalized Heat Flux Comparison.....	98
Figure 43. Case 4-C Normalized Heat Flux Comparison.....	99
Figure 44. Case 7-C Normalized Heat Flux Comparison.....	99
Figure 45. Case 9-C Normalized Heat Flux Comparison.....	100
Figure 46. Rivulet Freezing Modes: (a) Mode #1, (b) Mode #2 and (c) Mode #3 .....	103
Figure 47. Case NASAIR: Predicted Phase-Change Front Profile at Halt.....	120
Figure 48. Case 1-C: Predicted Phase-Change Front Profile at Halt.....	121
Figure 49. Case 3-C: Predicted Phase-Change Front Profile at Halt.....	122
Figure 50. Case 4-C: Predicted Phase-Change Front Profile at Halt.....	123
Figure 51. Case 7-A: Predicted Phase-Change Front Profile at Halt.....	124
Figure 52. Case 7-C: Predicted Phase-Change Front Profile at Halt.....	125
Figure 53: Parametric Results for the Wall Temperature, $T_w$ .....	134
Figure 54: Parametric Results for the Freestream Temperature, $T_{inf}$ .....	135
Figure 55: Parametric Results for the Freestream Velocity, $U_{inf}$ .....	136

## NOMENCLATURE

$A_r$	- rivulet cross-sectional area
$a$	- capillary constant
$Bi_R$	- rivulet Biot number
$Br$	- Brinkman number
$c_l$	- liquid phase specific heat
$c_s$	- solid phase specific heat
$F_r$	- ice/wall interfacial friction force
$g$	- gravitational constant
$h$	- enthalpy
$h_{lv}$	- latent heat of vaporization
$h_{ls}$	- latent heat of fusion
$h_{ph}$	- latent heat variable (see equation 4.18)
$h_{sv}$	- latent heat of sublimation
$\bar{h}_\infty$	- average heat transfer coefficient at the rivulet/air free shear interface
$\bar{h}_m$	- average mass transfer coefficient at the rivulet/air free shear interface
$\bar{h}_w$	- average heat transfer coefficient at wall/rivulet interface
$K_t$	- Kutateladze number
$k$	- thermal conductivity
$L$	- characteristic length
$Le$	- Lewis number

$L_E$	- equivalent rivulet length
$L_H$	- bulk rivulet length at halt
$Ma$	- Mach number
$M_w$	- molecular weight
$\dot{m}''$	- mass flux
$Nu$	- Nusselt number
$Nu_n$	- non-freezing Nusselt number
$Nu_p$	- phase-change Nusselt number
$Pe$	- Peclet number
$Pr$	- Prandtl number
$R$	- rivulet radius of curvature
$Re$	- Reynolds number
$rh$	- relative humidity of the freestream air
$St_s$	- Stefan number
$T$	- temperature
$t$	- time
$Wi$	- non-dimensional rivulet halt parameter
$x$	- dimensional coordinate in the physical domain
$X$	- non-dimensional coordinate in the physical and computational domains
$Y$	- non-dimensional coordinate in the physical domain
$\beta$	- contact or wetting angle
$\gamma$	- ratio of specific heats
$\delta$	- rivulet thickness at zenith



- $\eta$  - non-dimensional/normalized coordinate in the computational domain
- $\lambda$  - recovery factor
- $\mu$  - dynamic viscosity
- $\xi$  - normalizing variable in coordinate transformation
- $\rho$  - density
- $\sigma$  - interfacial surface tension
- $\tau_i$  - shear stress at the rivulet free surface
- $\varphi$  - non-dimensional temperature
- $\psi$  - non-dimensional enthalpy

#### Subscripts

- a - air
- e - edge of gaseous medium boundary layer
- fs - free surface
- g - gas
- i - “i” direction (or interface)
- inf - freestream
- j - “j” direction
- l - liquid
- ls - liquid/solid
- lv - liquid/vapor
- sv - solid/vapor
- mp - melting point
- r - rivulet

rec - recovery

s - solid

sat - saturation

sv - solid/vapor

v - vapor

$\infty$  - freestream

### Superscripts

n - computational time step

p - Gauss-Seidel iteration number

# CHAPTER I

## INTRODUCTION AND BACKGROUND

Ice accretion on airframe and propulsion system surfaces has long been a fundamental problem within the aerospace industry. Flight in an adverse weather environment results in both safety and performance concerns for civilian, as well as, military aircraft. The growth of ice deposits, from the freezing of atmospheric supercooled water droplets, on lifting surfaces can significantly degrade the aerodynamic performance of an aircraft. In addition, the performance of an aircraft's propulsion system can be significantly reduced due to ice accretion and ingestion. For example, ingested snow, hail and sleet can cause fan and compressor blade erosion, and can accumulate on both spinning and stationary component surfaces, resulting in a severe Foreign Object Damage (FOD) potential, if shed as ice chunks. Ingestion of large volumes of water can affect the propulsion system's combustion stoichiometry even resulting in combustor flame out [1].

Since adverse weather conditions provide such a threat, it is critical that the operational limitations of aircraft are well known so that dangerous situations can be avoided. Prediction of the resultant accreted ice shapes and sizes, as well as their location on aircraft surfaces, is paramount to the understanding of an aircraft's operational limits in adverse weather conditions. Operational limits are often extended by employing de-icing or anti-icing mechanisms. For efficient and effective use of such mechanisms, the operational limits of individual aircraft systems must be known. Both ground and flight testing are used to determine system performance under adverse

conditions, and the specific limitations of the system. However, ground testing can not always reproduce in-flight conditions without lengthy, expensive and often numerous alterations in test parameters. Additionally, flight testing is dangerous and depends on being able to find, or produce with tanker aircraft, appropriate atmospheric icing conditions. Therefore, much effort has and continues to be focused on the development of computational tools for simulation and analysis of ice accretion phenomena. Ice accretion simulators coupled with Computational Fluid Dynamics (CFD) codes for flowfield resolution, play an increasingly major role in the design of ground and flight tests and the analysis and evaluation of the subsequent test data. To assist in the prediction surface loading due to ice accretion on lifting surfaces, the LEWICE [2] code has been developed by NASA Glenn Research Center and associated contractors. LEWICE is a two-dimensional multiphase computer code for the analysis of ice accretion on aircraft wings due to the impingement, runback and freezing of supercooled water droplets. However, LEWICE lacks the generality to compute ice accretion in turbine engines due to certain simplifying assumptions made in its development. LEWICE has found its greatest application to wing and stationary blade ice accretion prediction. Elsewhere, at the U.S. Air Force Arnold Engineering Development Center (AEDC), a preliminary suite of codes for implementing engine icing computations is in development, and includes a three-dimensional viscous flow solver for computing the flowfield through rotating machinery, and a code for computing particle/droplet fluxes to the surfaces. These are the ADPAC [3,4] (Advanced Ducted Propfan Analysis Code) and K-ICE [5] codes, respectively. A three-dimensional ice accretion code, denoted the PATRICE code, applicable to turbine engine icing is being developed by Dr. Dennis

Lankford and others at AEDC [1,6]. The PATRICE (Particle Accretion and Tracking for Rain and ICE) code utilizes the surface fluxes obtained from K-ICE to calculate the ice accumulation on three-dimensional surfaces. Incorporated in the PATRICE code are such physical phenomena as surface water run back, convection and conduction heat transfer and the heat and mass transfer associated with the phase change modes of evaporation, condensation and sublimation. These codes are representative of the significant progress that has been made in the accuracy of ice accretion predictions, however, several enhancements, including better physical models of surface phenomena, must be implemented.

Of significant concern to the ice accretion modeling community is the capability of accurately modeling accretion during glaze icing conditions (an explanation of glaze and rime icing will be presented shortly). Under such conditions, heat transfer mechanisms and rates, and surface flow with subsequent freezing play a major role in the resultant accreted ice sizes and shapes. Realistic predictions of accretion shapes and sizes cannot be overemphasized, since these features have a direct impact on the functionality of the substrate body (i.e. airfoils, inlets, etc.). The physical behavior of impinging supercooled water droplets on an accretion surface and subsequent surface flow in glaze conditions can be very complex. One such phenomenon, in glaze conditions, is the break up of thin liquid films into rivulets that runback and then subsequently freeze. Modeling the freezing of liquid water runback in the form of rivulets is the substance of this research.

## Research Objective

The fundamental objective of the subject research is to provide a significant enhancement to current ice accretion modeling methodologies for handling surface “runback”. Specifically, the numerical simulation of the freezing of shear driven surface runback in the form of rivulets was undertaken. Runback water in the form of rivulets is a common phenomenon in several icing, anti-icing and de-icing scenarios of aircraft surfaces. An understanding of where and to what spatial extent and rate runback water will freeze is critical to the aircraft manufacturer and anti-icing/de-icing system designers. Such a numerical simulation provides valuable physical insights and makes a significant contribution to the ice accretion modeling community. For example, the developments resulting from this research could be integrated into the PATRICE (Particle Accretion and Tracking for Rain and ICE) code being developed at AEDC.

### Approach

The approach followed to achieve the stated overall objective is divided into three stages, namely:

1. Numerically simulate the freezing of a **stationary rivulet** by application of an “enthalpy method” formulation (see Chapter II). The enthalpy method is a robust physics based approach for solving solidification or melting (Stefan) type problems, and is tested on this simplified model while retaining the inherent characteristics of the rivulet geometry. This simplified model includes all the applicable modes of energy transport except for those convective modes associated with a flowing rivulet (i.e., convected enthalpy and convection heat

transfer at the liquid-solid interface). This model provides considerable insight into the freezing process of rivulet geometry while validating the integrity of the enthalpy method. Many key physical elements of the stationary rivulet model find utility in the freezing runback model.

2. Investigate the hydrodynamic behavior of rivulet flow driven by shear loads at the free surface. Incorporate the applicable hydrodynamic behavior into the **traveling rivulet** model and apply the enthalpy method formulation to numerically simulate the freezing thereof. The insights gained from the above step and the energy transport mechanisms associated with the rivulet flow are incorporated.
3. Validate a model of freezing shear driven rivulet runback with experimental data obtained from freezing rivulet tests on a flat plate conducted in the Icing Research Tunnel (IRT) at NASA Glenn Research Center. Measure the length of rivulet runback and closely examine, via video recorder, the subsequent ice accretion on the rivulet after the rivulet front has halted. Give careful attention to finding out the conditions associated with halted rivulet flow. Conduct test cases involving various rivulet sizes, ambient and substrate temperatures and initial (uniform) rivulet temperatures.
4. Parametrically investigate those parameters that affect the runback length and the complete solidification of freezing runback rivulets. Such an analysis provides insight as to which parameters have the greatest impact on rivulet runback and the solidification thereof.

## **Ice Accretion Background**

A familiarity with the fundamental principles and physical phenomena associated with the ice accretion process is necessary to an understanding of the genesis of rivulet formation in glaze icing conditions. This section provides background information related to the ice accretion process, accretion phases and the formation of a “runback” zone, of which rivulet flow is an offspring.

### **Ice Accretion Process and Phases**

The source of the accreted material, namely ice, is supercooled water droplets contained in a gaseous medium (air) that impinge on a surface moving through the medium. Upon impingement, nucleation of the drops begins, thus initiating the freezing and accretion process. Droplet sizes that range from approximately 15  $\mu\text{m}$  to 40  $\mu\text{m}$  in diameter are found in cloud systems that typically constitute “adverse weather conditions” for aircraft. FAA publication FAR 25, Part C defines the generally accepted envelope of icing conditions for transport aircraft. This document covers both intermittent and continuous icing conditions.

The temperature of the accretion surface has a dominant effect on both the freezing and cooling processes of impinging supercooled droplets. The temperature attained by the accretion surface is determined by the balance between the rate at which energy is supplied to the surface and the rate of energy loss to the environment. Energy is supplied predominately by the liberation of latent heat as the impinging drops freeze. Energy is also supplied to the accretion surface from the kinetic energy of impinging



droplets and aerodynamic heating. Energy is removed from the surface by forced convection, by evaporation at the water/air interface (or sublimation as in rime icing conditions) and by sensible cooling of the newly formed ice deposit. Since the accretion surface temperature cannot exceed 0 °C (273.15 K), a critical Liquid Water Content ( $LWC_{cr}$ ) [7], where all of impinging drops will be just frozen, can be determined locally based on parameters affecting the local surface energy balance. If the actual LWC is lower than the critical value, all of the droplets will freeze and the accretion surface temperature will be below 0°C. If, on the other hand, the actual LWC is greater than the critical value, the excess water, which cannot be frozen in the region of impingement, can coalesce into beads, run back downstream, shed or even be incorporated into the ice structure producing a spongy accretion. Thus, these two conditions are referred to as the dry and wet growth regimes, or more commonly as, the rime and glaze regimes, respectively. The wet, or glaze regime, is of interest in the subject research since this environment is conducive to surface runback and rivulet formation.

In a dry (or rime) accretion process, when the LWC is below the critical value, the freezing and cooling of the droplets takes place in three distinct phases; *the initial freezing, the subsequent freezing* and *the cooling phase* [7]. A newly arrived droplet is nucleated, ice is formed, and latent heat transferred into sensible heat within the drop, which in turn, drives the droplet temperature rapidly toward 0°C. This is the *initial freezing phase*, and results in a droplet that is now a mixture of water and ice. As the freezing process continues within the *subsequent freezing phase*, the complete phase transition from water to ice is accomplished by removal of the excess latent heat of fusion

at a constant temperature at or near 0 °C. In the *cooling phase*, with the droplet completely frozen, the drop begins to cool by forced convection at the free surface interface and conduction into the underlying substrate. In a steady state condition the accretion cools until, on the average, the initial accretion temperature is regained before the arrival of the next droplet. However, a local wet (or glaze) accretion is a condition where, because of insufficient heat dissipation to the environment, the *subsequent freezing phase* cannot be completed locally. This is equivalent to a LWC above the critical value.

The degree of *subsequent cooling* of impinging droplets under glaze accretion conditions is determined by the rate at which latent heat can be dissipated to the environment. As more droplets impinge, they too are unable to completely freeze, thus a liquid film is formed. At the same time, however, the ice accretion deposit thickens as heat dissipation continues to chip away at the latent heat of the water mass, but at a rate insufficient to freeze all the water. This unfrozen water cannot be ignored, for it is influenced by external forces and microphysical phenomena which can cause it to bead, coalesce or move along the surface to a region where the heat transfer coefficient is higher or the local collection efficiency is lower, and subsequently freeze there. This can have a dramatic impact on the resulting accretion size and shape. Ice accretion rates can vary significantly over the body due to microphysical phenomena resulting in the development of various surface flow mechanisms. Local variances in ice accretion rates along a body can be categorized into zones [8-12].

## **Glaze Ice Accretion Zones**

The great challenge of glaze ice accretion modeling is incorporating into the model the temporal and spatial variations of the accretion surface characteristics and their effect on the accretion rate. The local heat transfer coefficient ( $h_c$ ) is a critical parameter that can vary significantly from one location to another on the accretion surface and vary locally with time as accretion proceeds. This variation in upstream ice accretion rates gives impetus to, and determines the extent of, the downstream surface water runback. Variations in the local heat transfer rates in rime icing conditions are essentially of little concern, since all the impinging water freezes locally on impact. Thus, the local accretion rates correspond directly to the mass flux of the impinging liquid. This is the reason rime accretion modeling tends to be a simpler and more straightforward problem. If one can accurately model the impingement of supercooled droplets and subsequent phase change thermodynamics, the accretion configuration follows a priori. Rime accretions layers therefore, thicken as they follow the contour of the substrate. In the glaze (or wet) case, surface roughness elements may result initially from surface tension effects causing small roughness beads that then grow due to a locally favorable heat and mass transfer [13]. These beads of water may be formed from water that has coalesced in a region different from where it originally impacted.

In an effort to find a more physical based way of determining realistic heat transfer coefficients, Hansman and Yamaguchi [9] discovered from experiments of glaze icing on cylinders, that distinct zones of surface roughness, with identifiable boundaries, were formed. These roughness zones give great insight into glaze icing phenomena and

the extent of improvements necessary for ice accretion heat transfer and runback models.

The surface roughness zones are summarized below.

- The *smooth zone* is a uniformly wet region close to the stagnation point consisting of a thin film of water at warm temperatures. There is no distinctly visible roughness, hence a smooth region. What water is able to freeze out in this zone forms a translucent ice layer below the surface water.
- The *rough zone* is characterized by a sudden transition to a significantly rougher surface with insufficient water to maintain a film. The initial transition from the smooth zone to the rough zone is controlled by the natural pre-accretion boundary layer transition. In cases where there is no runback from this zone, surface tension forces dominate causing runback water from the upstream smooth zone and impinging droplets to coalesce into beads. This is associated with a marked increase in the heat transfer coefficient, and subsequently, an increase in the accretion rate. The increased roughness due to the beads causes the boundary layer to “trip” and subsequently undergo transition to turbulent flow at the upstream edge of the beads. With the boundary layer now turbulent in the region of the beads, the enhanced heat transfer causes the beads to freeze forming rough ice. Now this area becomes dry and beads form on the upstream side of this new ice, thus moving the smooth/rough transition farther upstream [10]. As this process continues, the transition interface propagates toward the stagnation region. Observations indicate that the above transition propagation rate increases with increasing surface water flow. This phenomenon is shown beautifully in the grazing angle photograph of Figure 1 [12].

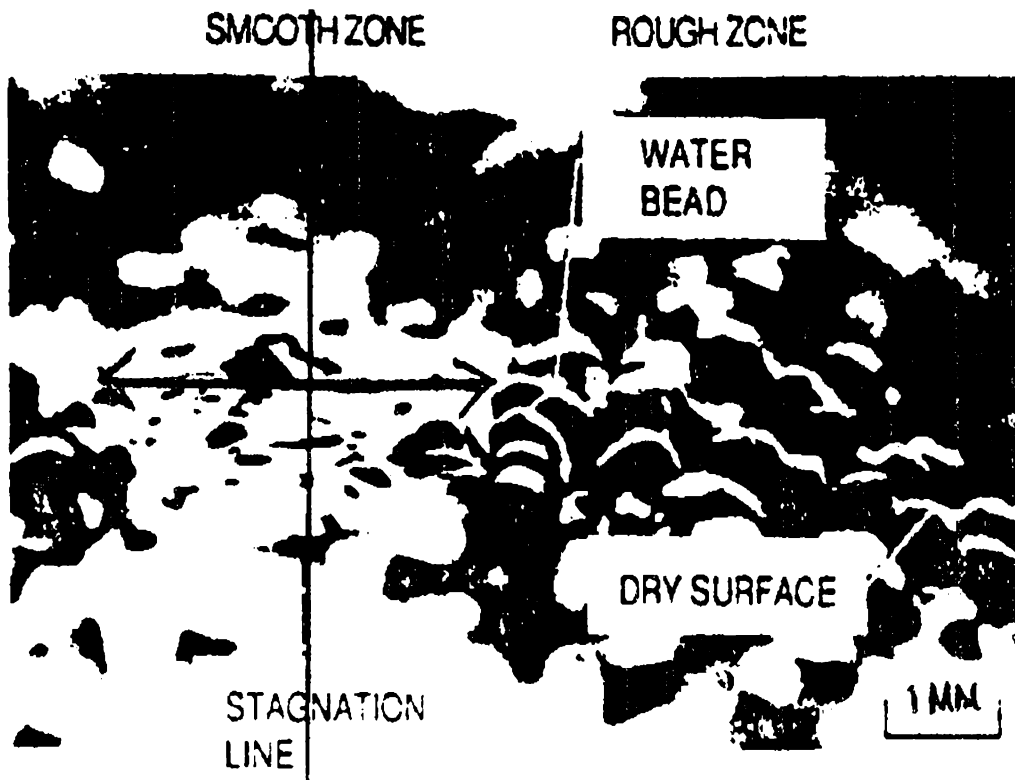


**Figure 1.** Glaze Ice Accretion Smooth/Rough Zone Transition Front

- Contained within the rough zone during times of particularly high water content is the *horn zone*. Some or all of the roughness elements in the rough zone can grow into protrusions, which themselves become macroscopic ice accretions. The result is increased heat transfer along with increased collection efficiency, wherein the protrusions begin catching droplets that otherwise would be swept by the body. These accretions then rapidly grow into the familiar horns common to many glaze icing accretions.
- At warm temperatures, or sufficiently high LWCs, when not all of the water in the rough zone is able to freeze, there can be runback aft of the rough zone. This constitutes the *runback zone* where water can move downstream in rivulets then stagnate at a point of flow separation or when a critical frozen fraction is reached. The latter is addressed in the subject research. As the water moves downstream it will typically freeze where the surface is cooler or has a higher heat transfer coefficient. Oft times it will freeze as rivulets or large coalesced water cells.

A segregation of the three distinct accretion zones described above is shown superimposed on a typical glaze accretion for a cylinder in Figure 2. The cylinder, at a temperature of  $-4.5\text{ }^{\circ}\text{C}$ , was exposed to an atmosphere traveling at 150 knots with a LWC of  $1.0\text{ g/m}^3$  and containing droplets with a mean volumetric diameter of  $30\mu\text{m}$ .

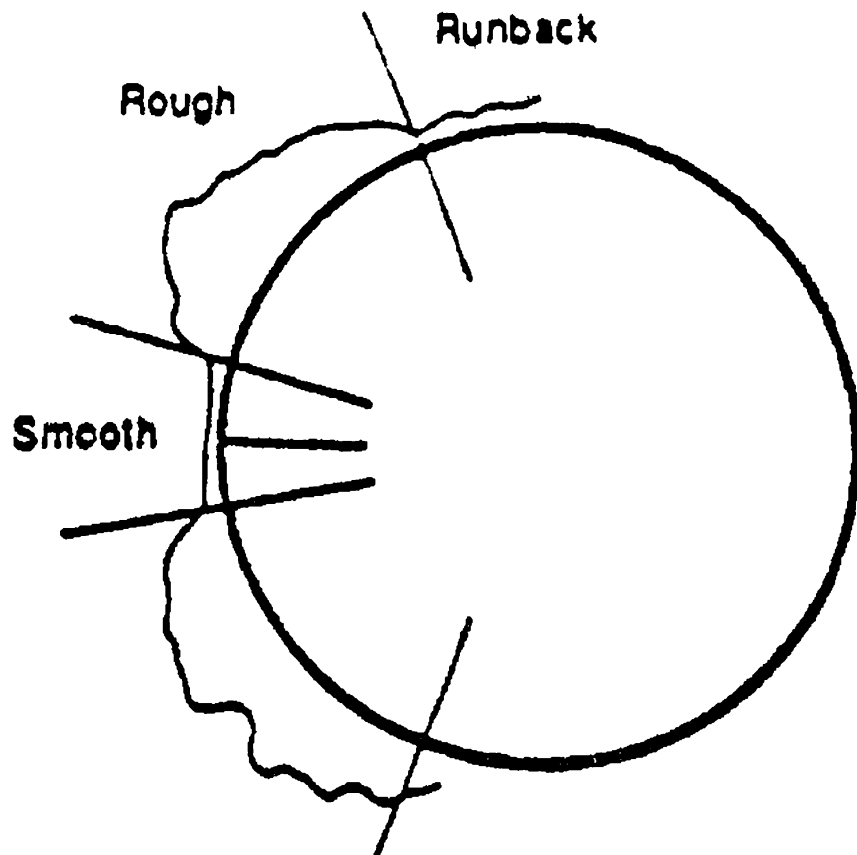


**Figure 2.** Typical Glaze Ice Shape Accretion Zones on a 1-in. Cylinder for a 2-min. Exposure

## **Surface Water Behavior Considerations**

Surface water behavior provides significant concerns in accretion modeling because the water can move and change shape. It affects both heat and mass transfer mechanisms, which directly influence the ice accretion rate. For water bead growth there are two main scenarios: first, bead growth at the smooth/rough transition interface continues until the heat transfer is increased sufficient enough to freeze all the water from impingement and upstream runback; and second, bead growth by liquid mass impingement and coalescence until external dynamic forces cause droplets to slide along or be shed from the surface [12].

The ability of water to spread, or wet the surface, decreases as the surface temperature decreases and increases as surface temperature increases. As the ice surface becomes less wettable, there is increased resistance to motion, and it requires greater forces to move the water along. Thermal gradients along the surface can be very important to the development of accreted surface roughness. Small variations in the surface temperature can restrict the motion of water and cause bead formation. Dry ice in the area around the beads can be cooled below 0 °C, increasing the barrier to water flow. Water impinging or running onto a cold dry surface will freeze quicker, and droplets that strike beads will be trapped within the bead while icing occurs at the lower surface of the bead.

Individual freezing of droplets is also noteworthy, since as a drop freezes before the impingement of another in the same place, a hummock with a shadowing effect is



formed [14]. This shadowing effect influences the local microscopic collection efficiency, which is a function of the local impingement angle and contact angle

Finally, in that region of the runback zone that is near the impingement limit of the supercooled droplets, a thin liquid film that once wetted the whole surface can become unstable due to surface tension forces and cause the film to breakdown. The film breakdown is manifest as individual streams or rivulets separated by dry regions. This phenomenon is clearly illustrated in Figure 3 [15] below, wherein rivulets have formed on a B1-B inlet vane and are driven back by free surface shear. Included in these observations is the subsequent formation of water beads and their travel downstream beyond the leading edge of the rivulets. Shear driven surface water runback in the form of rivulets, and the subsequent freezing thereof, is an important common phenomenon in glaze icing conditions, for which the development of a model and associated numerical simulation is detailed herein.

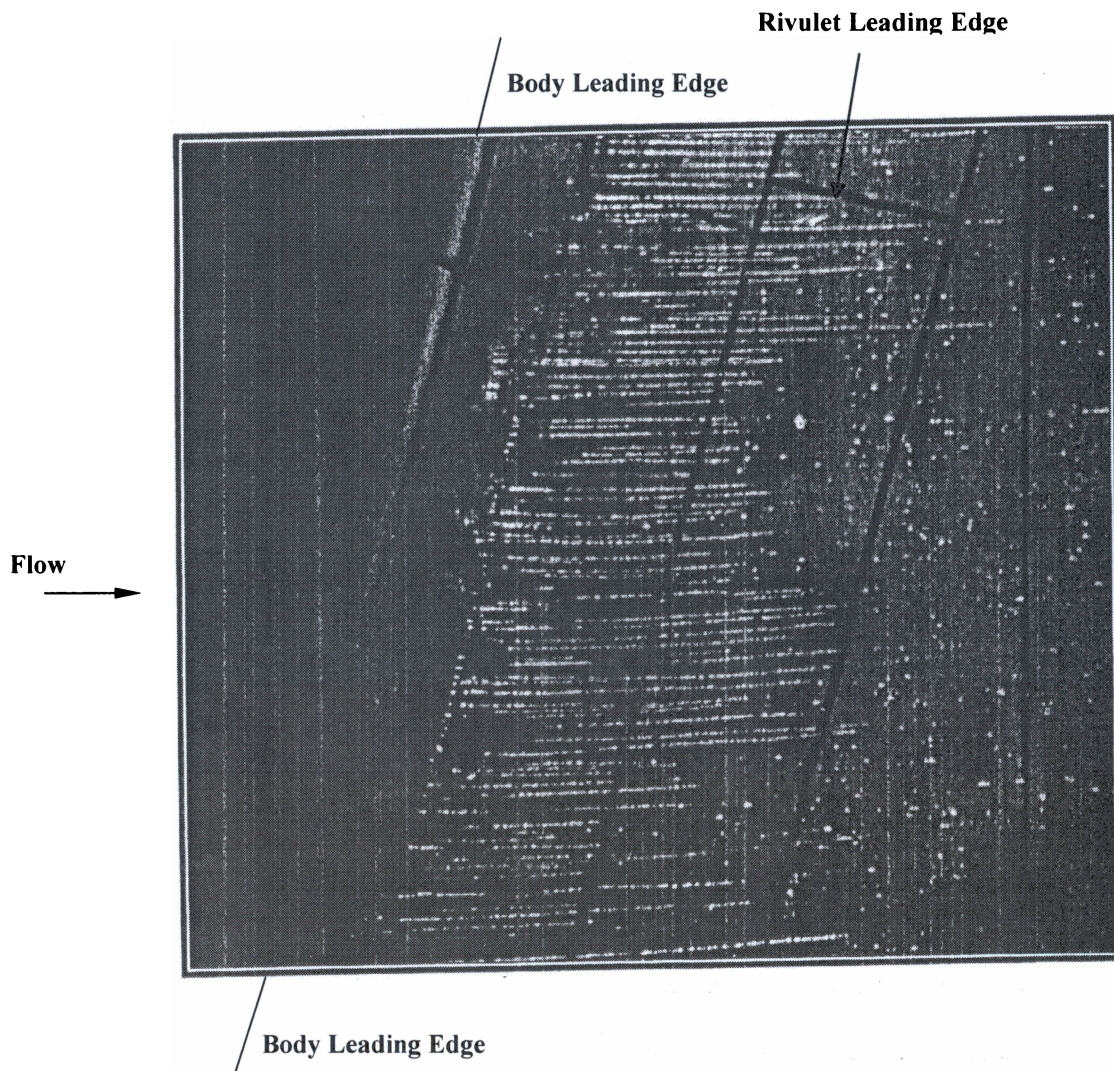


**Figure 3.** Rivulet Runback on a B1-B Inlet Vane in the Icing Research Tunnel (IRT) at NASA Glenn Research Center

## **CHAPTER II**

### **FUNDAMENTALS OF THE FREEZING RIVULET MODEL**

The flow of surface runback as rivulets, and their subsequent freezing downstream, is a common glaze ice accretion phenomenon on critical airframe and propulsion system surfaces. Knowledge of the amount and spatial extent of frozen surface runback is critical for aircraft designers. Many analytical and experimental investigations and simulations of freezing flow have been successfully undertaken, however, a review of the literature has revealed nothing with regards to the numerical simulation of freezing rivulet flow. A very nice treatment of rivulet runback on aircraft surfaces in glazing icing conditions was conducted by Al-Khalil [16]. Al-Khalil's work embodied the incorporation of rivulet flow into the simulation of an aircraft anti-icing system, wherein the temperature of the rivulets is maintained above the freezing point due to the application of a thermal energy load. Thus, the rivulets would continue to "run wet" downstream of their formation and not freeze. Several insights related to the characteristics of rivulet flow were gleaned from the work of Al-Khalil and applied to the subject analysis and simulation of freezing shear driven rivulet flow.

#### **Freezing Rivulet Geometry**

The fundamental geometry and associated parameters, including simplifying assumptions, of the freezing rivulet model are described in this section. The specific conditions, governing equations and modeling methodologies related to the stationary

and traveling freezing rivulet cases are addressed in detail in Chapters III and IV, respectively.

### **Rivulet Formation and Resultant Geometry**

In adverse weather conditions conducive to glaze ice accretion, where not all of the suspended supercooled water droplets freeze on impingement with a surface, a thin water film forms on the surface. Such a thin liquid film forms in the direct impingement region near the surface stagnation point. The impingement region is bounded by upper surface and lower surface limits, which are the last points on these surfaces aft of the stagnation point which are hit by water droplets [2]. In this region, water wets the entire surface by direct impingement of supercooled water droplets and the addition of water running back from upstream regions closer to the stagnation point [17]. The thin liquid film initially forms in the “smooth zone” as described in Chapter I and illustrated in Figures 1 and 2. The subsequent behavior of this liquid film is controlled by the interaction of surface tension, the shear force at the free surface and surface roughness.

The starting point in the numerical simulation of freezing rivulet flow is that point on the surface where the rivulets have first formed from the breakup of a shear driven, thin liquid film. Mikielewicz and Moszynski [18] apply conservation principles at the instant of film breakup, and show that for newly formed rivulets to be stable, the energy of the system should be a minimum. Therefore, the breakup of the water film into rivulets is considered to take place downstream of the impingement limits, wherein there is no surface flux due to droplet impingement. The size of individual rivulets is determined from the coupling of the upstream mass flow rate, minimum energy

principles and surface tension effects. Although the breakup of a thin liquid film is a primary source of rivulet flow, rivulets can also be formed from the coalescence of water beads in certain regions of the accretion surface, i.e. aft of the rough zone shown in Figure 2. Fundamentally, the freezing rivulet model herein considers the rivulet flow to be downstream of the droplet impingement limits, fully developed, driven by viscous shear at the free surface interface and free from the effects of surface waves and other aerodynamic distortions of the rivulet free surface. Thus, as the rivulet runs back and freezes, it is assumed to maintain a circular cross section as shown in Figure 4. Any reduction in rivulet mass due to evaporation or sublimation, or increase in rivulet mass due to condensation is modeled as a reduction or increase, respectively, in the rivulet radius of curvature (“R” in Figure 4.). Thus, mass subtraction or addition is applied uniformly over the rivulet surface, and the circular cross section is maintained. These key features of the model of rivulet flow provide simplification to the freezing rivulet model while maintaining a robust and physically realistic geometry. Clearly, in most runback situations, numerous rivulets run back, parallel to each other, separated by non-wetted surface; however only a single rivulet stream is of interest here. Thus, the analysis and results presented herein are applicable to each rivulet within a community of non-interacting, parallel rivulets on the substrate of interest.

#### Physical Conditions and Assumptions

The following conditions and assumptions apply to the subject simulation of freezing rivulet runback and form the basis upon which the geometry and associated

parameters are established. The resultant rivulet model cross sectional geometry with associated key parameters is illustrated in Figure 4.

- The rivulet forms and subsequently runs back downstream of the direct water droplet impingement region.
- The effect of gravity on the shape of the rivulet surface is negligible. This assumption is validated by the fact that the *capillary constant* ( $a$ ) is significantly larger than the characteristic dimension ( $\delta$ ) of the rivulet. The capillary constant is defined as [19]:  $a = (2 \sigma / g \rho)^{1/2}$ , where  $\sigma$ ,  $g$  and  $\rho$  are the liquid/gas interface surface tension, gravitational constant and density, respectively. The capillary constant for water at the melting point temperature of 273.15 K is approximately 4.0 mm. For the type of rivulet under investigation, the rivulet height ( $\delta$ ) ranges from 0.2 mm to 0.9 mm. Given that the capillary constant is considerably greater than this characteristic length, surface tension dominates and gravitational effects on the surface geometry can be neglected.
- The rivulet “wets” the surface of the substrate of interest. This implies that the contact angle  $\beta$ , the angle formed by the rivulet free surface as it intersects the substrate, is less than  $90^\circ$ .
- The flow inside the rivulet is fully developed and laminar. Surface waves are neglected.
- The effects of neighboring rivulets on the free shear layer of the subject rivulet are neglected, i.e., an individual rivulet can be analyzed independently.

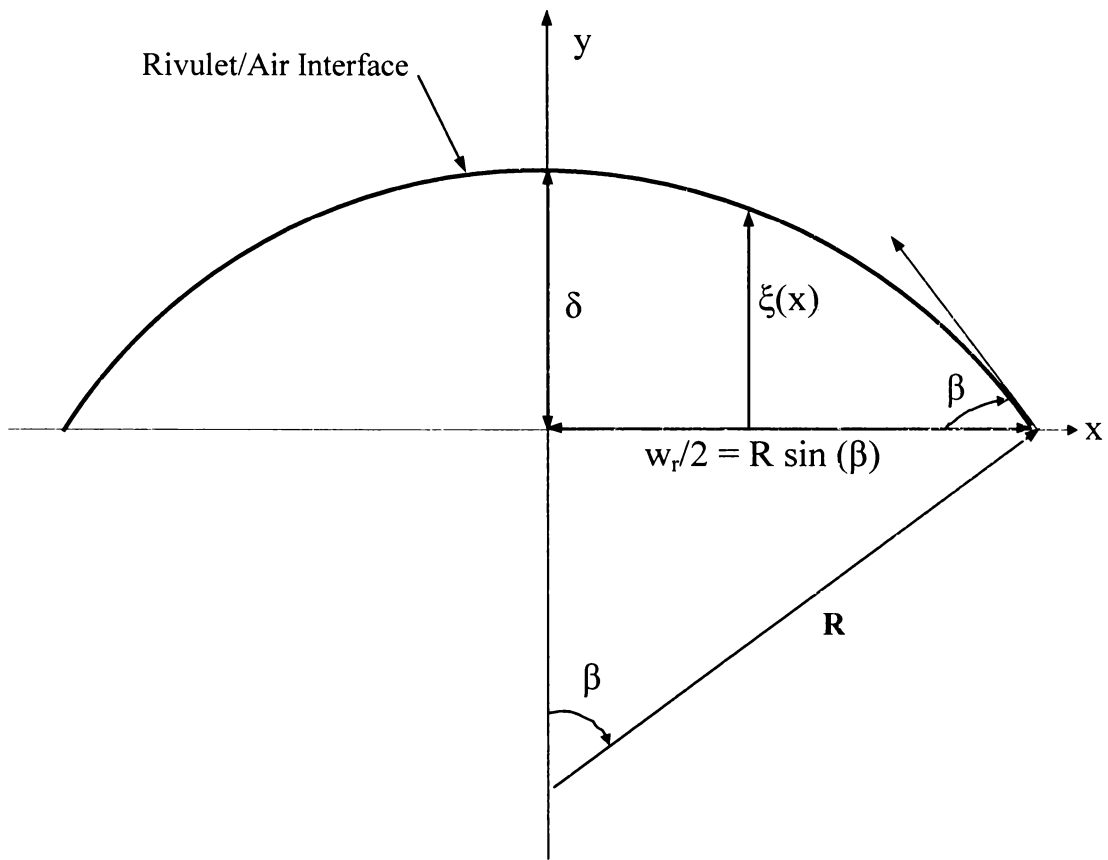


**Figure 4.** Rivulet Cross-section and Fundamental Geometric Parameters

- Any reduction or addition to the mass of the rivulet during the freezing process is manifest through a change in the rivulet radius of curvature. Thus, the rivulet maintains a circular cross section.

Given the circular cross section driven by the liquid/gas interface surface tension, the rivulet surface is defined by

$$\xi(x) = (R^2 - x^2)^{1/2} - R \cos(\beta), \quad \text{for } 0 \leq x \leq R \sin(\beta), \quad (2.1)$$

where  $R$  is the radius of curvature and  $\beta$  is the contact angle. From equation (2.1) and referring to Figure 4, one can see that at  $x = 0$ ,  $\xi(0) = R - R \cos(\beta) = \delta$ , and at  $x = R \sin(\beta)$ , the rivulet half width,  $\xi(R \sin(\beta)) = 0$ .

### **The Stefan Problem**

In its most basic form, the freezing rivulet problem is identified with a class of problems defined as Stefan-type. Stefan problems are simply a class of heat transfer problems involving solidification from a melt or melting of a solid, and include the hallmark “Stefan Condition” at the phase-change interface. The Stefan Condition simply states that the latent thermal energy release due to the displacement of the phase interface is equal to the amount of heat transferred to (or from) the interface. Thus, the Stefan Condition defines the energy balance across the phase interface and forms a moving boundary condition as defined below in equation (2.2), and illustrated in Figure 5, for a simple 1-D problem.



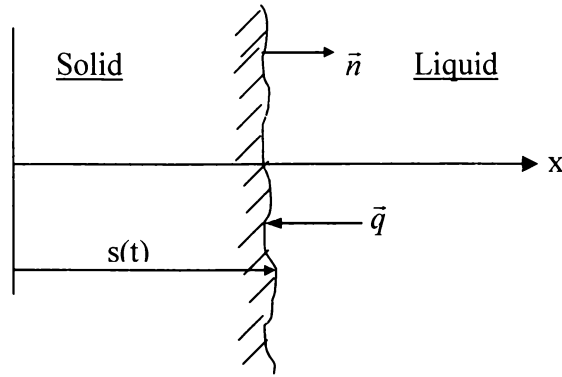


**Figure 5.** Moving Phase-Change Interface for a 1-D Stefan Problem

$$\rho h_{fs} \frac{ds}{dt} = [-\vec{q} \cdot \vec{n}]_{solid}^{liquid}. \quad (2.2)$$

Consider a material initially in the liquid phase ( $t \leq 0$ ) at a uniform temperature  $T_1 > T_{mp}$ , where  $T_{mp}$  is the phase-change temperature. The liquid is then instantaneously ( $t = 0$ ) subjected to a cold substrate maintained at a constant temperature  $T_2 < T_{mp}$ . Such conditions will cause a layer of solid to form on the substrate. If conditions exist such that the heat transfer and subsequent phase front propagation ( $s(t)$ ) are 1-dimensional, this Stefan problem can be described by the following pair of equations; one for the solid phase,

$$\frac{\partial}{\partial x} \left( k_s \frac{\partial T_s}{\partial x} \right) = \rho c_s \frac{\partial T_s}{\partial t}, \quad 0 \leq x < s(t) \quad (2.3)$$

and the other for the liquid phase,

$$\frac{\partial}{\partial x} \left( k_l \frac{\partial T_l}{\partial x} \right) = \rho c_l \frac{\partial T_l}{\partial t}, \quad x \geq s(t). \quad (2.4)$$

At the solid-liquid boundary, the following condition applies:

$$k_s \frac{\partial T_s}{\partial x} \Big|_{x=s(t)} - k_l \frac{\partial T_l}{\partial x} \Big|_{x=s(t)} = \rho h_{ls} \frac{ds(t)}{dt}, \quad x = s(t), \quad (2.5)$$

which is the classical Stefan Condition, and where

$$T_s = T_l = T_{mp} \quad \text{at } x = s(t).$$

The 1-dimensional Stefan Problem, governed by equations (2.3) – (2.5) above, is challenging to solve by analytical closed-form techniques due to the non-linearity introduced at the moving phase front boundary. This non-linearity, geometric in nature, rests in the fact that the regions, solid and liquid, in which the linear partial differential equations are to hold are unknown functions of time and must be found as part of the solution. Thus, not only is there a discontinuity in thermophysical properties at the interface, but also the solution becomes a function of the unknown phase front propagation speed.

### **The Enthalpy Method**

The class of Stefan problems for which analytical, closed-form solutions can be found are few [20], and the solutions obtained only apply to very restrictive conditions. Such restrictive conditions include: one dimensional, semi-infinite geometry, uniform initial temperature, constant imposed temperature at the boundary, and constant thermophysical properties in each phase [20]. Analytical techniques, such as the

Goodman Integral Method [21] and the Biot Variational Method [22] provide reasonable results for the solution of simple Stefan problems with certain restrictive conditions applied. Numerical techniques that are employed to solve the above governing equations require that the phase interface boundary,  $x = X(t)$ , be explicitly tracked. The capability of “front tracking” is an artifice that is difficult for the vast majority of available numerical solvers to implement.

However, there is one numerical method that is formulated in such a way as to avoid the necessity of tracking the phase-change interface. The enthalpy (or weak) solution approach to Stefan problems is based on the fact that the energy conservation law, expressed in terms of enthalpy (energy) and temperature, coupled with the appropriate equation of state, contains all the necessary information needed to determine the evolution of the phases [20]. The enthalpy method is sometimes referred to as the “weak” solution on the grounds that it is an approximation to the weak solution of the governing differential equations. The power of weak solutions, wherein “weak derivatives” are invoked, is found in the solution to problems that have inherent jump discontinuities. Inherent in Stefan problems is the jump discontinuity of thermophysical properties at the phase front; namely enthalpy and thermal conductivity. Therefore, the basic energy conservation law holds throughout the material, and the phases are subsequently distinguished by the application of the equation of state relating enthalpy and temperature. Thus, the enthalpy method is a “volume tracking” scheme rather than a “front tracking” scheme. In reality this method may be best characterized as a “front capturing” scheme, wherein the phase interface is not brought out explicitly but is

captured within a local volume or computational cell. The interface location may be obtained from the cell enthalpy as described below.

The enthalpy method is implemented by applying energy conservation to each control volume to obtain a discrete heat balance. From the heat balance, one can update the enthalpy of each cell. From the enthalpy equation of state, and knowing the latent heat of fusion, the state of the control volume can be determined (i.e., all solid, all liquid or part liquid and part solid...slushy). A “slushy” cell contains the phase interface, and the portion of the cell that is liquid (the liquid saturation quality) can be derived from the liquid mass fraction. That is, once the enthalpy method has solved for the enthalpy of a slushy cell, the liquid mass fraction of the cell can be ascertained and the phase interface predicted. Since a “slushy” volume or cell separates the two distinct phases, the accuracy of the enthalpy method in tracking the phase front is limited by the grid resolution, or size of a single computational cell. However, grid resolution becomes less of an issue since one can further define the location of the phase-change front within the slushy cell by utilizing the liquid (or frozen) mass fraction of the cell. In the vast majority of Stefan problems, such accuracy is sufficient and certainly acceptable within the scope of the subject problem. After application of the enthalpy formulation, the Stefan problem above is now described by

$$\frac{\partial}{\partial x} \left( k \frac{\partial T}{\partial x} \right) = \rho \frac{\partial h}{\partial t}, \quad x \geq 0 \quad (2.6)$$

where  $h$  is the enthalpy and  $k$  and  $\rho$  are functions of temperature. Through application of the appropriate equation of state, the relationship between enthalpy and temperature is shown to be

$$h = \begin{cases} c_s u, & u < 0 \\ c_l u + h_{ls}, & u > 0 \end{cases}, \quad \text{where } u = (T - T_{mp}), \quad (2.7)$$

and

$$u = \begin{cases} \frac{h}{c_s}, & h \leq 0 \quad (\text{solid}) \\ 0, & 0 < h < h_{ls} \quad (\text{interface or "mushy" cell}). \\ \frac{(h - h_{ls})}{c_l}, & h \geq h_{ls} \quad (\text{liquid}) \end{cases} \quad (2.8)$$

### Advantages of the Enthalpy Method

According to Voller and Cross [23], significant advantages of the enthalpy method are:

- there are no conditions to be satisfied at the phase interface boundary,  $x = X(t)$ ;
- there is no need to accurately track the phase interface boundary;

- there is no need to consider the phase regions on either side of the phase front separately, and
- if necessary, one can easily introduce a “slushy” region, wherein the phase-change occurs over a range of temperature rather than a single point.

The above advantages coupled with the fact that the enthalpy method is robust and has a direct physical interpretation to the solution of Stefan problems, render this method an excellent approach to the modeling of freezing rivulet runback. A Stefan problem formulated using the enthalpy method is amenable to solution by both explicit and implicit numerical methods. Herein, a robust implicit scheme is employed in the solution of the freezing rivulet runback problem.

This study examines rivulet solidification for cases where the liquid rivulet temperature is at or very near the freezing temperature, as would be typical for runback in glaze icing conditions. Under such conditions, only latent heat is removed from the liquid phase, whereas, in the solid phase, sensible thermal energy is removed via heat transfer. Because only latent heat is removed from the liquid phase, the problem is identified as a “One-Phase Stefan Problem” in which the solid phase is the only active (sensible) phase wherein a temperature gradient exists [20]. The “one-phase” Stefan problem can be nicely characterized by an insightful parameter called the Stefan number. For the “one-phase” freezing process, which is of greatest interest here, the Stefan number is defined by

$$St_s = \frac{c_s (T_{mp} - T_s)}{h_{fs}} \quad (2.9)$$

The Stefan number represents the ratio of sensible heat that must be removed, per unit mass, during the freezing process to the latent heat removed per unit mass. From such a ratio, one can readily get an indication of whether the process will be dominated by phase-change or by sensible heat conduction. The process of freezing rivulet runback is clearly dominated by phase-change, where the Stefan number ranges from 0.01 to 0.03 for the cases under consideration herein. Certainly, the Stefan number varies in relation to the  $\Delta T$  imposed. However, problems involving the freezing of water are generally dominated by phase-change

A few select cases where the liquid phase temperature is elevated above the melting point are treated in this study in an effort to validate the model through correlation with experimental data. Such cases are identified as “Two-Phase Stefan Problems”, wherein both phases are active with sensible heat removal. Freezing runback downstream of a de-icing or anti-icing region is an example of a scenario where the Stefan problem must account for two active phases. Herein, the rivulet temperature would be non-uniform with the potential for initiating a phase-change front at the rivulet free surface and propagating inward, toward the substrate. Such a scenario could conceivably invoke considerable complexity to the rivulet flow model by establishing an ice crust at the free surface. The runback rivulets examined in the subject study that are inherently “two-phase” Stefan problems are assumed to have an initial uniform temperature distribution,  $T_r > T_{mp}$ . The uniform temperature distribution reduces the

concern of phase front propagation from the free surface during the runback process, but does reveal some other interesting features to be discussed in Chapter V. However, during the freezing process of a “two-phase” stationary rivulet, phase fronts can propagate inward from both the cold substrate and the free surface boundary. This phenomenon will be clearly illustrated in Chapter IV, wherein the “stationary” freezing rivulet problem is discussed.



### **CHAPTER III**

#### **EXPERIMENTAL SIMULATION OF FREEZING SHEAR DRIVEN RIVULETS**

The experimental simulation of shear driven freezing rivulets provided qualitative and quantitative data used in the validation of the numerical simulation of freezing rivulet runback. The experimental simulation was conducted in the NASA Glenn Icing Research Tunnel (IRT), Cleveland, Ohio; a facility wherein the environmental parameters could be controlled with a high degree of fidelity. The experimental data from selected test cases were used to benchmark the numerical simulation in order to establish its validity and accuracy. In pursuit of this objective, answers to the following questions were desired.

- What are the distances rivulets of various sizes and various initial temperatures runback, under icing conditions, before the rivulet front halts?
- Does the halting of the rivulet front coincide with the commencement of freezing or does some freezing take place before the rivulet front completely stops?
- Once the initial rivulet front has halted, what is the behavior of subsequent runback water as it continues to flow from upstream?

## **Experimental Simulation Configuration**

The test configuration focused on a test article that would generate well-developed rivulet flow that would runback and freeze. A necessary requirement was to have a substrate upon which the macro physical phenomena of freezing rivulet runback could be observed. Furthermore, obtaining the distance the rivulet front traveled before the frozen portion halted was a primary test objective. The rivulets were introduced via small diameter tubes rather than employing the Icing Research Tunnel spray bar system. Since the focus was not on the mechanisms rivulet formation, but to experimentally simulate the freezing of fully developed rivulet runback, the means by which the rivulet flow was initiated was not critical.

### **Test Apparatus**

The appropriate freestream environment for the subject experiment was provided by the NASA Glenn IRT. The IRT is a closed-loop atmospheric tunnel that is uniquely equipped to support the low-speed testing of icing related models [24]. The test section is 6 ft. high, 9 ft. wide and 20 ft. long, wherein the velocity of air can be controlled from 50 mph to 430 mph. Although not employed with the subject test, the IRT has a unique spray bar system capable of delivering various liquid water contents (LWCs) and mean volumetric droplet (MVD) sizes. The reader interested in the scope of capabilities of the IRT is referred to Soeder, et al. [24] for details.

The test article designed to carry the rivulets was a simple “flat plate” configuration 12 in. wide, 48 in. long and 0.5 in. thick. The plate was constructed from

aluminum stock with a black anodized finish introduced for the purpose of enhancing the optical contrast. Also, a 1/8 in. leading edge radius was employed to provide a reasonably sharp leading edge and reduce blunt edge effects. Three liquid water supply tubes were introduced to the top surface from beneath on an angle pitched in the direction of the freestream airflow as shown in Figures 6 and 7. The tube openings were milled flat consistent with the plate to make a smooth transition for the water to the plate. Three tube sizes were selected; namely 0.050 inch O.D., 0.188 inch O.D. and 0.375 inch O.D. in an effort to facilitate the formation of rivulets of varying size. A close-up of the interface between the rivulet water supply tubes and the flat plate test article is shown in Figure 8. The supply tube openings intercept the flat plate surface 10 inches downstream of the leading edge at an approximate angle of 45 degrees. The 10-inch offset from the leading edge was deemed necessary to allow the airflow to sufficiently develop over the plate and reduce edge effects on the downstream rivulet runback. As shown in Figures 6-8, three rivulet paths were established with distance divisions marked adjacent to each path. The white distance markers made it possible to note the length of rivulet travel and subsequent halt via optical means.

A unique valve set was employed in the supply lines to make possible the introduction of the rivulet water, while at the same time supplying heated air to an annular jacket around the supply tubes. The heated air jacket was an added design feature that could be employed to regulate the water temperature and/or keep the portion of the supply lines that were exposed to the cold environment from freezing. Three independent Joucomatic<sup>TM</sup> solenoid type valves were fitted with modified atomizer heads



**Figure 6.** Flat Plate Test Article in the IRT Test Section

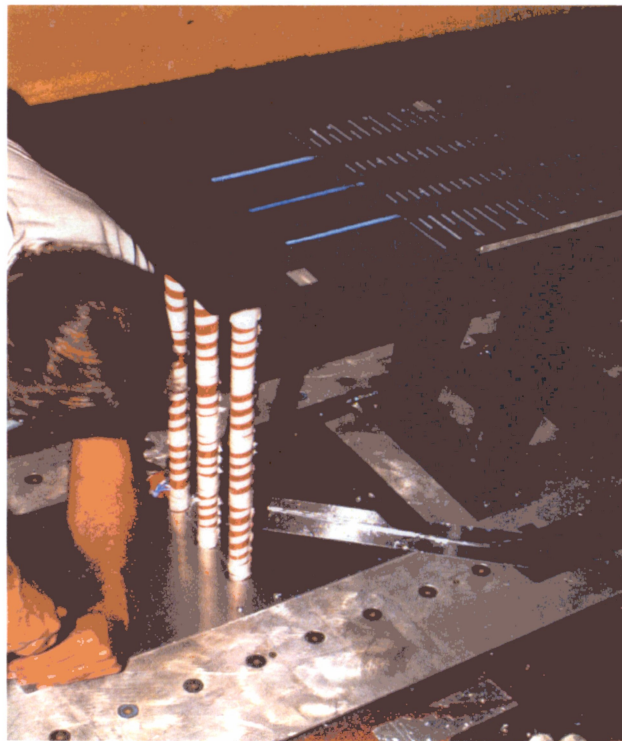


**Figure 7.** Flat Plate Test Article in the IRT Test Section– Close-up of Supply Tubes

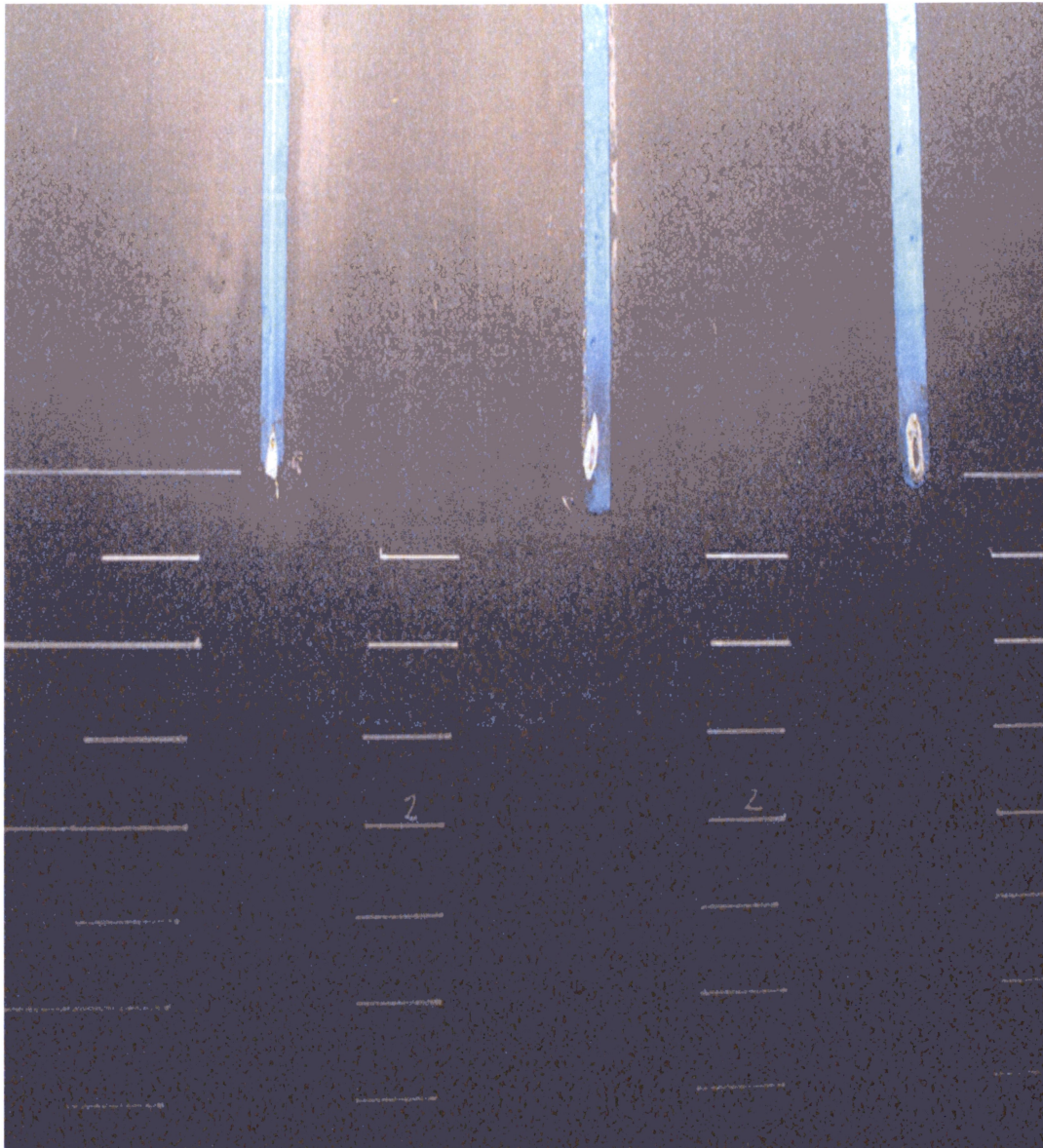


**Figure 8.** Interface Between the Rivulet Water Supply Tubes and the Flat Plate

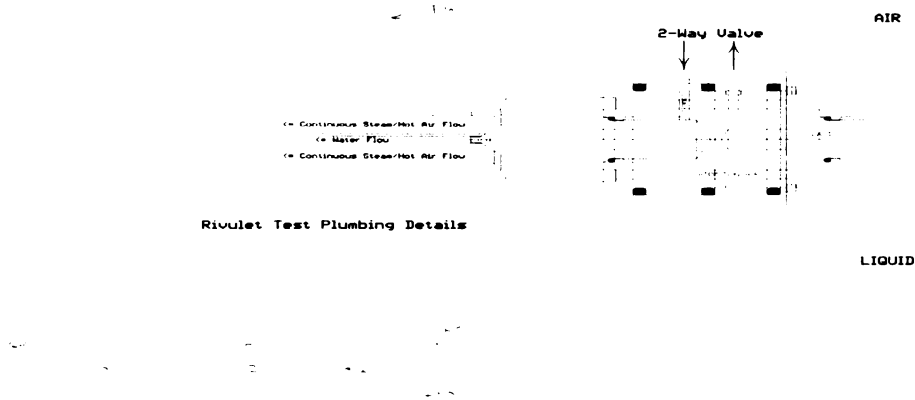


**Figure 9.** Schematic of Valve System with Modified Atomizer Head

to provide the rivulet water and an annular heated air jacket through a single valve system. A schematic of the valve system with the modified atomizer head is shown above in Figure 9. The valve systems were configured together in a manifold layout, with each being controlled independently from the IRT control room. The control valve systems were attached to the rivulet water and heated air supply lines, shown in Figures 6 and 7, immediately below the IRT test section.

The rivulet water was supplied from a pressurized reservoir located beneath the IRT test section, shown in Figure 10. Immediately downstream of the water reservoir, several feet of the main supply line were coiled for potential immersion in an ice bath, so as to form a heat exchanger to pre-chill the rivulet water.

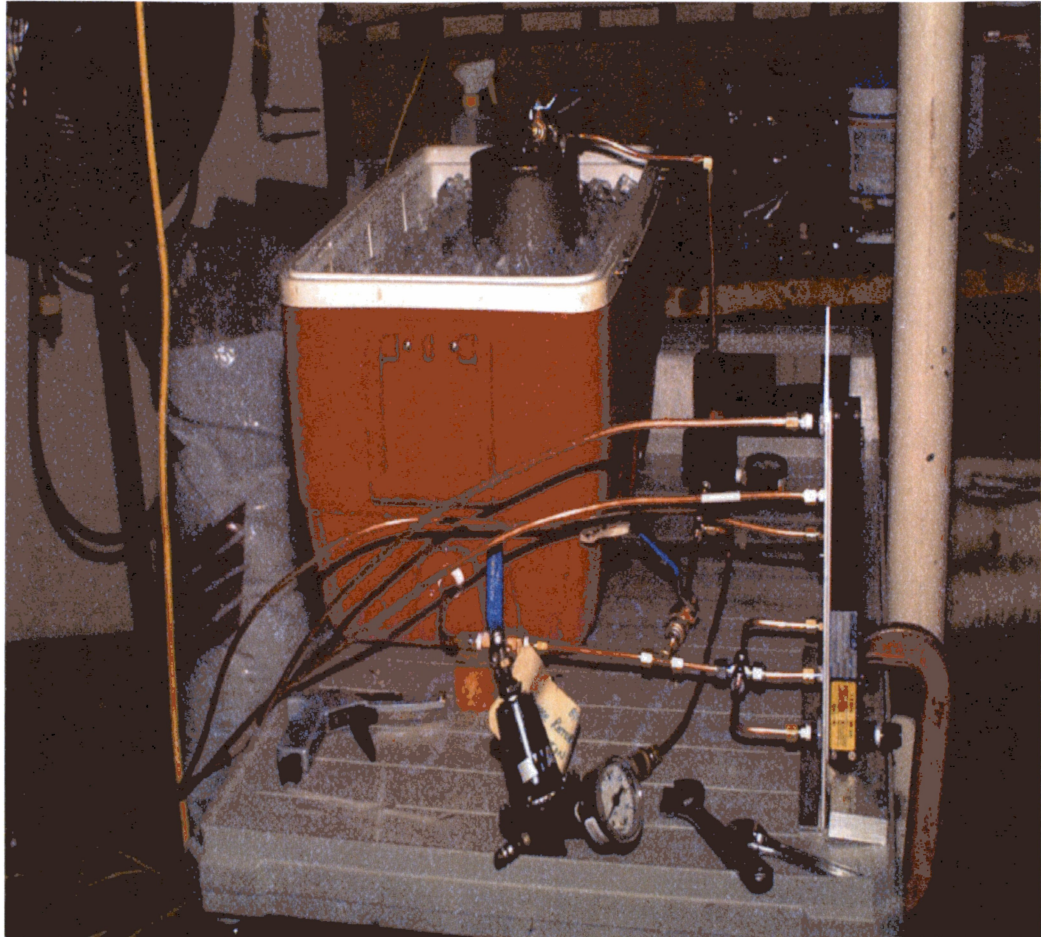


**Figure 10. Rivulet Water Reservoir, Ice Bath and Associated Plumbing**

Although shown in Figure 10, this pre-chill feature was found to be unnecessary during the conduct of the subject tests. The capacity to introduce shop air into the water supply line after a rivulet run, in order to purge the line of water and mitigate line-freeze, was also included.

### **Instrumentation**

The span of time between receipt of permission from NASA Glenn to perform this experiment and the actual conduct of the test was reasonably short. Given this contracted window of opportunity, the experiment was designed to garner as much qualitative data as possible via human observations and video recording. In addition, a necessary requirement was to measure certain key parameters for post-test evaluation and analysis. The circumstances noted above were the motivation to employ a relatively simple suite of instrumentation, primarily consisting of video recording equipment.

A suite of high and low speed video imaging equipment, on site at the IRT, was employed to capture, as well as possible, the physical phenomena associated with the freezing of rivulet runback. Three imaging, or camera, orientations were used; namely an overhead “pan”, an overhead “fixed” and a “graze” angle in the plane of the flat plate test article.

To capture the initial temperature of the rivulets before running back and freezing, type “T” Copper-Constantan thermocouples were inserted in the rivulet water supply tubes near the their opening onto the flat plate. The attempt was made to allow slight penetration of the tube wall by the miniature bead of the thermocouple junction. In



addition, a series of type “T” thermocouples were stationed along the flat plate test article to measure the temperature of the freezing surface. This temperature is equivalent to the wall temperature used in the numerical simulations discussed in the previous chapter.

Finally, three calibrated flowmeters were installed upstream of the solenoid valve systems. Pre-test calculations, based upon analytical formulations previously discussed, were used to determine the mass flow rate values that would produce the desired resultant rivulet size. At times, during the initial onset of rivulet flow, fine-tuning of the mass flow rate was necessary to achieve the appropriate continuous flow. Each flowmeter was selected to handle a different range of flows with an associated resolution. The flowmeter panel of the subject experiment is shown in Figure 11.

### **Test Parameters**

A test matrix was developed to examine the effect of the following test variables on freezing rivulet runback.

- Freestream air speed, and therefore the rivulet free surface interface shear stress and recovery temperature.
- Substrate surface finish, and therefore rivulet contact (wetting) angle
- The initial rivulet temperature (considered uniform) at the onset of runback.
- Freestream air temperature, and therefore the recovery temperature at the rivulet free surface.



**Figure 11.** Flowmeter Panel – Flowmeter in each Rivulet Water Supply Line

- Rivulet size, i.e., radius of curvature and width.
- Substrate, or freezing surface, temperature.

The relative humidity of the air stream was not a parameter of the test matrix, and therefore was not specifically controlled. However, for this experimental work the relative humidity of the air stream was maintained within a band from 80 and 88 %.

### **Test Procedure**

The overall test procedure first consisted of a preliminary calibration of steady state rivulet formation, thermocouple signal outputs and camera placement and lighting in a running wet (no freezing) mode. The air speeds during this phase matched those of the actual test cases, however the air temperature was elevated to above the freezing point. Finally, a series of freezing rivulet runback test cases was run under the conditions outlined below. For each test case there were three rivulet sizes run, and the initial rivulet temperatures, in parentheses, are for rivulets A, B and C respectively.

- Test Case #1:
  - $T_w = 272.7 \text{ K}$ ,  $T_{in} = (285.7 \text{ K}, 286.9 \text{ K}, 276.6 \text{ K})$ ,  $T_{inf} = 271.0 \text{ K}$ ,  $\beta = 38^\circ$ ,  
and  $U_{inf} = 44.7 \text{ m/s}$  (100 mph)
- Test Case #2:
  - $T_w = 271.7 \text{ K}$ ,  $T_{in} = (284.1 \text{ K}, 286.6 \text{ K}, 274.9 \text{ K})$ ,  $T_{inf} = 270.8 \text{ K}$ ,  $\beta = 38^\circ$ ,  
and  $U_{inf} = 44.9 \text{ m/s}$  (100.5 mph)

- Test Case #3:
  - $T_w = 270.4 \text{ K}$ ,  $T_{in} = (283.3 \text{ K}, 282.3 \text{ K}, 273.2 \text{ K})$ ,  $T_{inf} = 269.7 \text{ K}$ ,  $\beta = 38^\circ$ ,  
and  $U_{inf} = 45.2 \text{ m/s}$  (101.0 mph)
- Test Case #4:
  - $T_w = 270.9 \text{ K}$ ,  $T_{in} = (284.6 \text{ K}, 283.4 \text{ K}, 273.2 \text{ K})$ ,  $T_{inf} = 270.8 \text{ K}$ ,  $\beta = 38^\circ$ ,  
and  $U_{inf} = 67.2 \text{ m/s}$  (150.4 mph)
- Test Case #6: (Note, contact angle change.)
  - $T_w = 271.5 \text{ K}$ ,  $T_{in} = (287.4 \text{ K}, 287.6 \text{ K}, 277.8 \text{ K})$ ,  $T_{inf} = 270.8 \text{ K}$ ,  $\beta = 60^\circ$ ,  
and  $U_{inf} = 44.8 \text{ m/s}$  (100.2 mph)
- Test Case #7:
  - $T_w = 270.6 \text{ K}$ ,  $T_{in} = (280.4 \text{ K}, 285.6 \text{ K}, 276.2 \text{ K})$ ,  $T_{inf} = 269.8 \text{ K}$ ,  $\beta = 60^\circ$ ,  
and  $U_{inf} = 44.7 \text{ m/s}$  (100.0 mph)
- Test Case #8:
  - $T_w = 271.1 \text{ K}$ ,  $T_{in} = (283.7 \text{ K}, 283.2 \text{ K}, 275.7 \text{ K})$ ,  $T_{inf} = 270.8 \text{ K}$ ,  $\beta = 60^\circ$ ,  
and  $U_{inf} = 67.1 \text{ m/s}$  (150.1 mph)
- Test Case #9:
  - $T_w = 270.1 \text{ K}$ ,  $T_{in} = (280.6 \text{ K}, 283.1 \text{ K}, 277.1 \text{ K})$ ,  $T_{inf} = 270.8 \text{ K}$ ,  $\beta = 60^\circ$ ,  
and  $U_{inf} = 67.0 \text{ m/s}$  (149.9 mph)

After the air speed and ambient temperature were set, sufficient time was allowed for the flat plate to thermally equilibrate. Once again, supercooled droplet impingement,

or cloud, conditions were not required since rivulet formation is considered to initiate downstream of the particle impingement zone.

Rivulets A, B and C of Test Cases 1-4 were each run sequentially on the polished anodized surface ( $\beta = 38^\circ$ ) by opening and closing the respective solenoid valves. Sufficient upstream water was allowed to run after the initial rivulet front had halted to gain insight into subsequent flow behavior and accretion surface growth. After each rivulet run, its associated supply line was air purged to remove all water and mitigate line-freeze. The IRT facility steam supply was used to quickly remove the accreted ice from the test article between test cases.

Roughing-up, or dulling, the surface of the rivulet lanes on the flat plate using a small piece of steel wool increased the rivulet contact angle ( $\beta = 60^\circ$ ) for Test Cases 6-9. Test Cases 6-9 were run in similar sequential fashion to Test Cases 1-4.

#### Rivulet Contact Angle Determination

Prior to the conduct of the experimental simulations, representative contact angles were measured in a laboratory at the University of Tennessee Space Institute. The Wilhelmy Slide Technique [25] was employed to measure the contact angles on a black anodized aluminum coupon for both smooth and rough conditions. The formulation that relates the meniscus height to the wetting (contact) angle is given by

$$\sin(\beta) = 1 - \frac{\rho g h^2}{2\sigma_{l,v}}, \quad (3.1)$$

where  $h$  is the meniscus height and  $\sigma_{l,v}$  is the liquid-air surface tension. The values recorded in the laboratory, and subsequently used in the post-test evaluations and numerical simulations, were  $\beta = 38^\circ$  and  $60^\circ$  for the smooth and rough surfaces, respectively.

## **Experimental Results**

Validation of key physics-based models in the numerical simulation of freezing shear driven rivulet runback was the primary objective of the subject experimental simulation. The prediction of the “bulk rivulet” halt distance, or the distance at which a deposition of ice from the rivulet front onto the wall begins, is a major element of the numerical simulation. The “bulk rivulet” halt distance is explained in detail in Chapter V, wherein the numerical simulation of freezing rivulet runback is examined in detail. Accordingly, the experimental determination of the rivulet front halt distance is crucial to the validation effort. Figures 12-16 provide “snapshot” images of the Case 1-C, 3-C, 4-C, 7-A and 7-C rivulets at their respective bulk rivulet front halt distances. Although many experimental test cases were run, these five cases form a representative subset of well-formed runback rivulets, and for which the data extraction was considered most accurate. Shown in Figure 17, is a capture of the bulk rivulet halting phenomena from a NACA 0012 airfoil rivulet runback test conducted in the NASA Glenn IRT by other investigators studying rivulet runback phenomena [26]. The NACA 0012 rivulet test case is used hereafter as a baseline case in the numerical simulation effort.

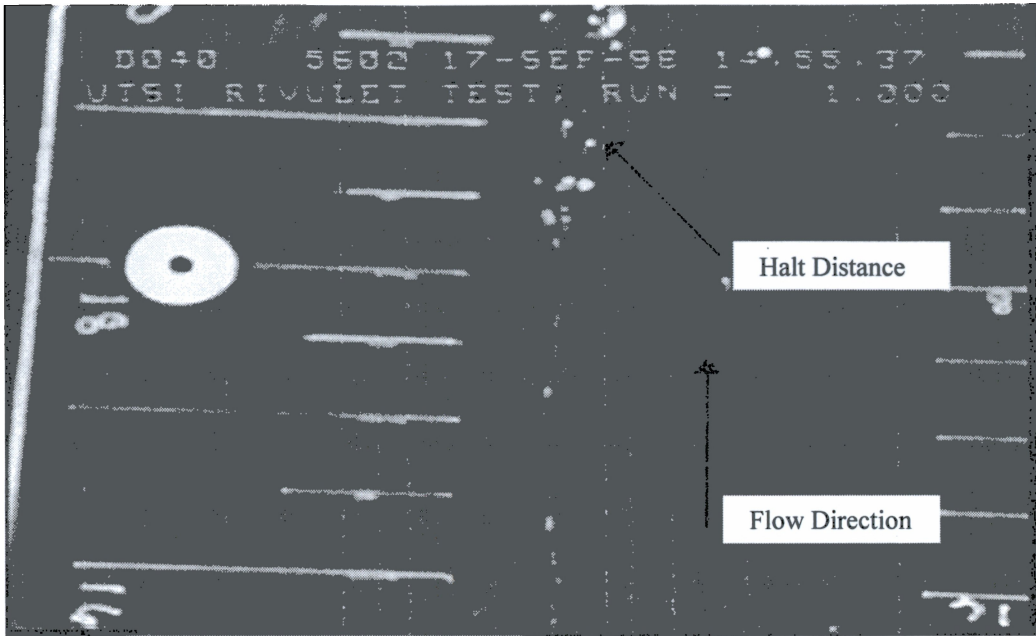


**Figure 12.** Rivulet 1-C at Rivulet Front Halt Distance

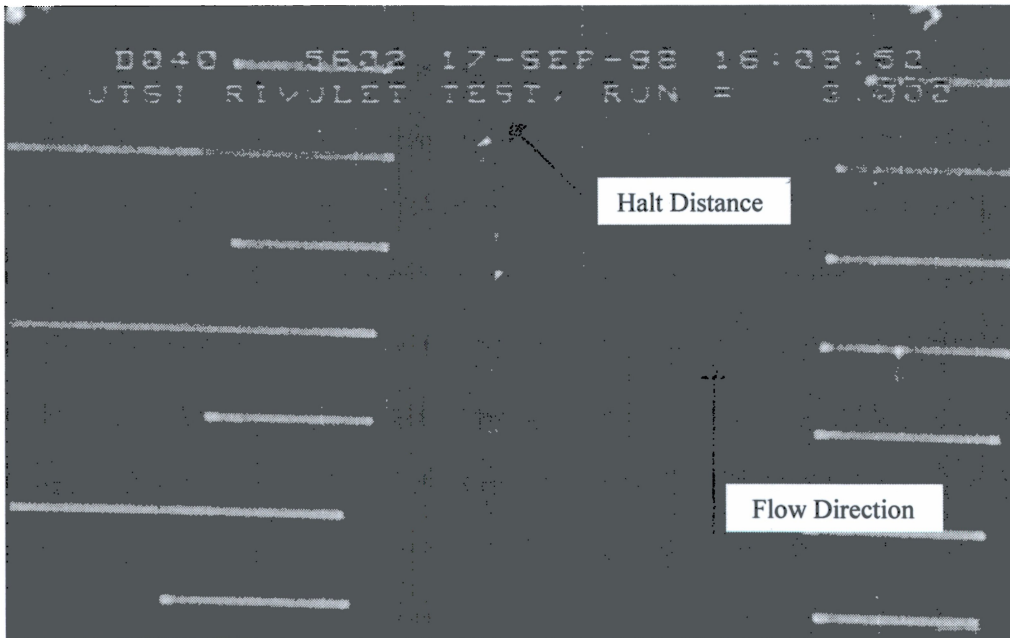


**Figure 13.** Rivulet 3-C at Rivulet Front Halt Distance

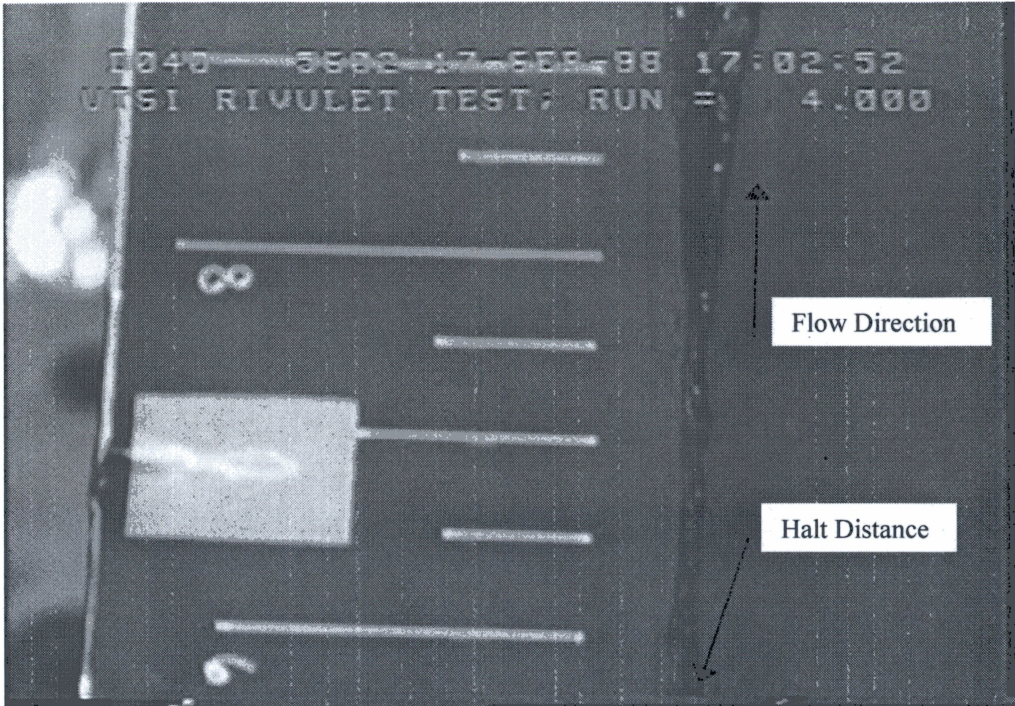


**Figure 14.** Rivulet 4-C at Rivulet Front Halt Distance

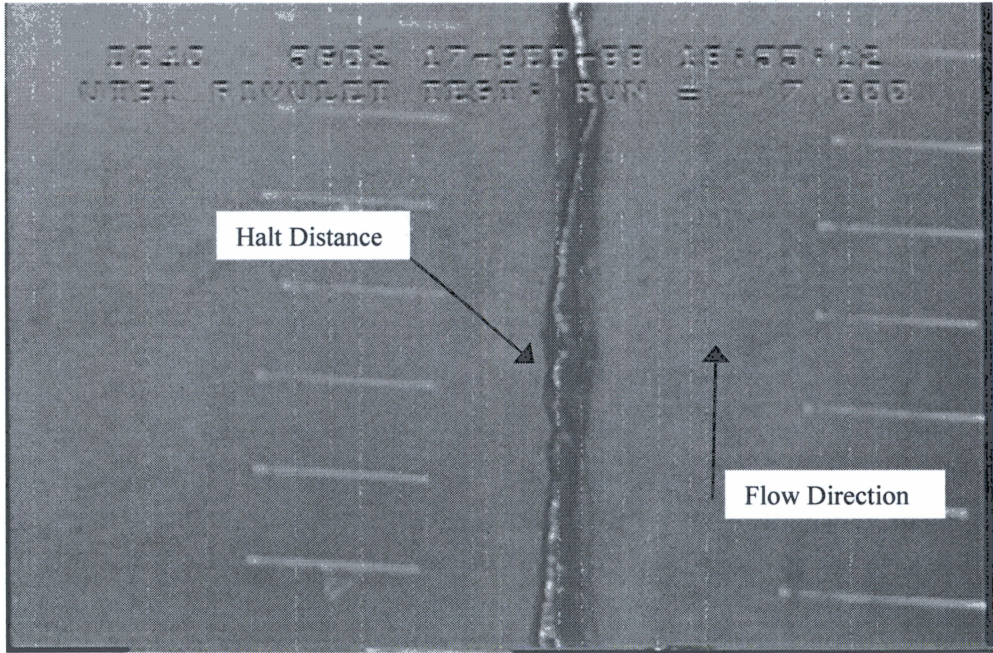


**Figure 15.** Rivulet 7-A at Rivulet Front Halt Distance



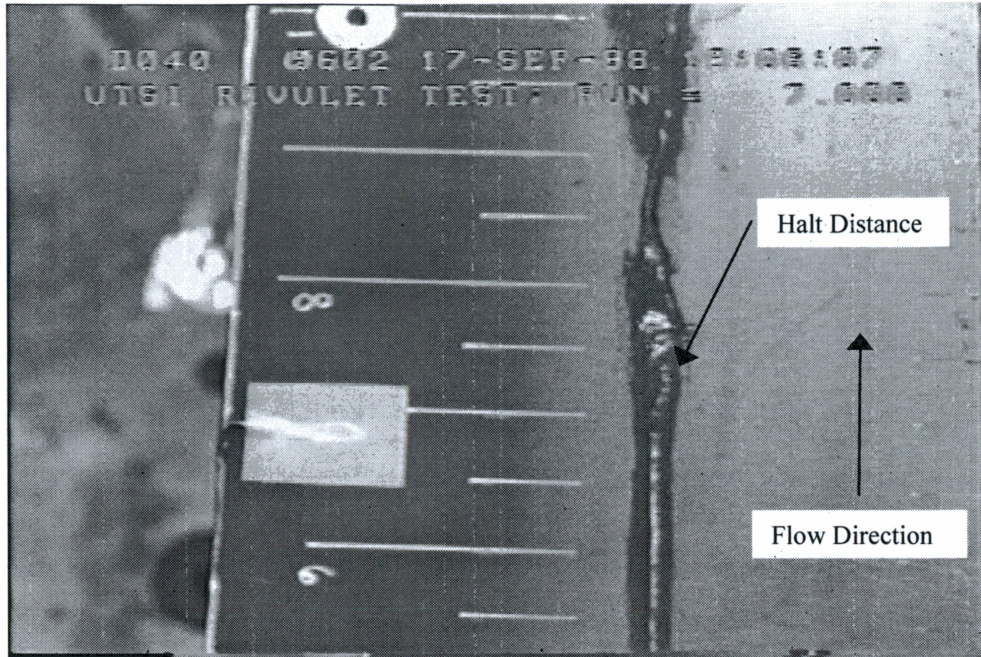


**Figure 16.** Rivulet 7-C at Rivulet Front Halt Distance

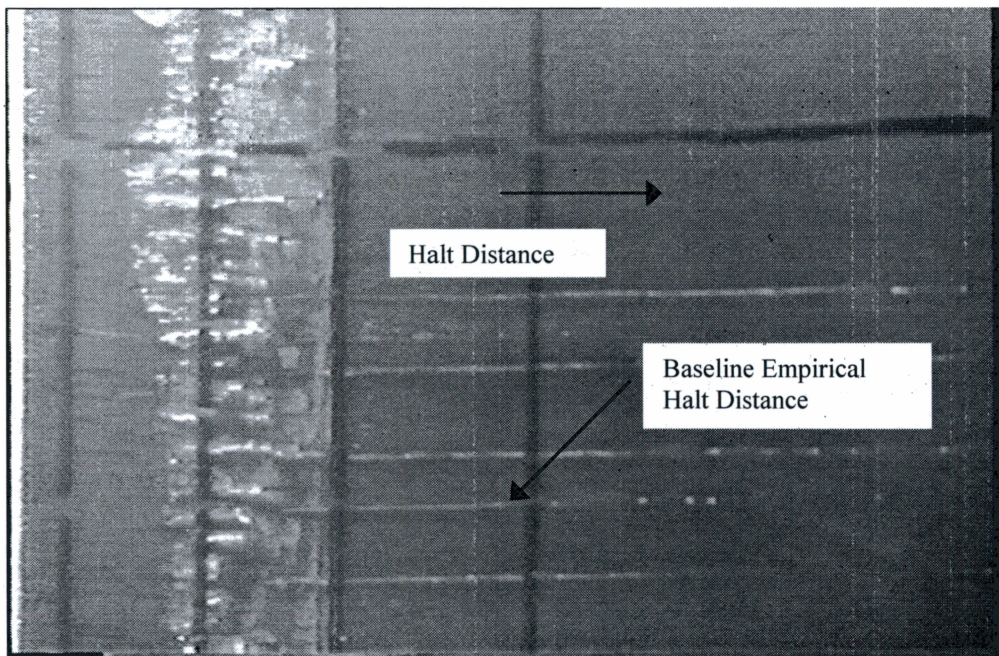


**Figure 17.** NACA 0012 Rivulets Running Back – Halt and Extension Phenomena

## **Conclusions and Remarks**

The results of Table 1 show the experimental, or measured, “bulk rivulet” halt length,  $L_H$ . The “bulk rivulet” halt distance is a parameter that quantifies a condition observed in previous experimental work [15,26], and is modeled as one of the freezing rivulet runback modes in the rivulet runback simulation that follows. One of the primary objectives of this experimental effort was to quantify the “bulk rivulet” halt distance parameter under varying initial and environmental conditions. The “bulk rivulet” halt distance is described in detail in Chapter V (see Figure 46a), however, summarily the halt distance refers to that distance traveled by the freezing rivulet before the frozen portion halts and the remaining liquid continues on downstream. Thus, the rivulet does not lose mass due to solid deposition during runback, but remains intact until an empirically determined halt distance is reached. In another light, the “bulk rivulet” halt distance corresponds to the length of the continuous rivulet structure as seen in Figures 3 and 17 for the BI-B inlet and NACA 0012 airfoil, respectively.

The experimental results were extracted via observation from video recordings of the freezing rivulet runback process. Thus, inherent in these results is a qualitative subjectivism not found in, otherwise, precise measurements. In Figures 12-13 and 15-16, one readily notes that there is frozen rivulet upstream of the indicated “bulk rivulet” halt distance. The author was using a panning camera, and by the time the rivulet front halt region was located, deposition of the frozen fraction of the rivulet front had begun and subsequent freezing in the upstream direction was already underway. The “bulk rivulet”

**Table 1.** Experimental Bulk Rivulet Halt Distances

	<b>Rivulet Parameters</b>	<b>Measured <math>L_H</math></b>
<b>Case 1-C</b>	$\beta = 38^\circ$ , $T_{in} = 276.6$ K, $T_{inf} = 271.9$ K, $T_w = 272.7$ K, $Ste = 0.00158$	489 mm (19.3 in)
<b>Case 3-C</b>	$\beta = 38^\circ$ , $T_{in} = 273.2$ K, $T_{inf} = 269.7$ K, $T_w = 270.4$ K, $Ste = 0.0155$	127 mm (5.0 in)
<b>Case 4-C</b>	$\beta = 38^\circ$ , $T_{in} = 273.2$ K $T_{inf} = 270.8$ K, $T_w = 270.9$ K, $Ste = 0.0125$	140 mm (5.5 in)
<b>Case 7-A</b>	$\beta = 60^\circ$ , $T_{in} = 280.4$ K, $T_{inf} = 269.8$ K, $T_w = 270.6$ K, $Ste = 0.0125$	127 mm (5.0 in)
<b>Case 7-C</b>	$\beta = 60^\circ$ , $T_{in} = 276.2$ K, $T_{inf} = 269.8$ K, $T_w = 270.6$ K, $Ste = 0.0147$	185 mm (7.3 in)

halt distances were ascertained by locating that point farthest downstream where the flow began to stagnate against the stationary ice. This stagnation zone was manifest through a subsequent widening of the rivulet in the region. After the “bulk rivulet” halt distance was reached, the rivulet continued to freeze in the upstream direction toward the point where freezing was first initiated.

The experimental tabular data were obtained from the distance values recorded using the flat plate length markings adjacent to each rivulet path. These data, as well as, other phenomena were captured on copious video footage. Considerable effort was made to capture the physics of the most fundamental of these observed phenomena in the subsequent numerical models. The nature of the experimental measurements precludes

an error analysis to be obtained for the experimental data. More research of this kind is needed to assemble an adequate statistical database.

Observations suggested that rivulet runback does travel downstream to a point where the frozen portion of the rivulet front halts, or ice deposition begins. The rivulet front at this juncture appeared to be partially frozen, with the liquid portion continuing to flow downstream. This physical phenomenon is a fundamental element in the numerical simulation of freezing rivulet runback. From observation, one could not ascertain the distance in the travel that coincided with the onset of phase-change. However, numerical simulation predicts initialization of phase-change at a distance well before where ice deposits were observed experimentally. Although this micro-scale phenomenon could not be observed, there was experimental evidence pointing to the fact that ice is not immediately deposited (halts) at the initiation of phase-change, but travels a distance downstream before coming to rest. In several of the rivulet cases, once the bulk rivulet front was observed to come to a halt, the rivulet would continue to freeze forward, or upstream. The upstream propagation of the phase-change front reveals that phase-change was initiated before ice was deposited from the original bulk rivulet and a subsequent stagnation point formed. This same upstream propagation was observed to continue until the freeze, or phase-change initiation point was reached. At this point, further upstream freezing of the rivulet has stopped due to equilibrium in the thermal energy transport, wherein the condition is said to be “freeze choked”. Water continues to enter the freezing rivulet domain at this station, and is only limited by the capacity of the upstream source.

When the solenoid valves were opened to initiate rivulet flow, the immediate result was not always a uniform continuous stream. Trapped air in the supply tubes mixed with water, at times, caused a short burst of spray. Thus, a few seconds were required to allow the rivulet flow to become established and stabilize. Care was taken to distinguish between frozen residue from this initial spray and the subsequent freezing phenomena of the rivulet runback.

Finally, the subject experimental simulation provided qualitative insights that substantiated several physics-based elements of the numerical simulation. Comparative data were obtained for the halt distances of the bulk rivulet runback. Upstream phase-change propagation from the first ice deposit (front halt) was observed to continue until a freeze choke condition was reached. In addition, the frozen rivulet was observed to provide a preferred path for subsequent upstream flow to follow while traveling downstream.

## CHAPTER IV

### STATIONARY FREEZING RIVULET NUMERICAL SIMULATION

The **stationary** freezing rivulet simulation provides valuable insight into the freezing process of rivulet geometry with specified boundary conditions. Many key physical features of the **stationary** model are integral to the freezing rivulet runback model detailed in Chapter V. The effectiveness and robustness of the enthalpy method for solution of the Stefan problem are validated through this model. As the name implies, the subject rivulet remains stationary relative to the adjacent substrate while submerged in a convective flow field. Although the rivulet would, in reality, be driven under the influence of shear at the free surface, the convective boundary is included in an effort to understand the impact of such a condition on the freezing process. Thus, the **stationary** model is simplified by eliminating the rivulet velocity field, but retains its utility by capturing many key physical features insightful to the subsequent, more complex, runback model.

#### Computational Formulation

The details of casting the problem within an appropriate computational framework are the substance of the present section. Such a framework consists of an appropriate computational domain, governing equations and boundary conditions.

## **Computational Domain**

Establishing an effective computational domain is fundamental to reducing numerical complexities. Although, semi-circular in nature, the rivulet geometry shown in Figure 4 reveals that a polar coordinate system would be fraught with difficulty given that the domain does not originate from the center of curvature. The physical domain of the rivulet in the non-dimensional coordinates defined by

$$X = \frac{x}{\delta} \quad \text{and} \quad Y = \frac{y}{\delta}, \quad (4.1)$$

and where  $\delta$  is the rivulet height, is shown in Figure 18. If the contact angle ( $\beta$ ) were  $90^\circ$ , the physical and computational domains would naturally be the same, i.e. a polar domain. As clearly seen in Figure 4, there exists a natural symmetry in the rivulet geometry. Thus, the computational domain is derived from a physical domain bounded by a plane of symmetry. The computational formulation and associated discretization of the rivulet domain is simplified through the transformation of the physical domain to a rectilinear computational domain. Such a domain transformation is consistent with the work of Al-Khalil [16] for rivulets running wet. In an effort to maintain consistency for possible comparison, the author employs the same transformation variables used by Al-Khalil [16]. The grid density (10 x 20) applied by Al-Khalil was used as the baseline grid resolution for the subject numerical simulation. This grid resolution was found to provide sufficient accuracy, especially when used with a method wherein the phase-change front is captured, as is the case with the enthalpy method. Furthermore, the

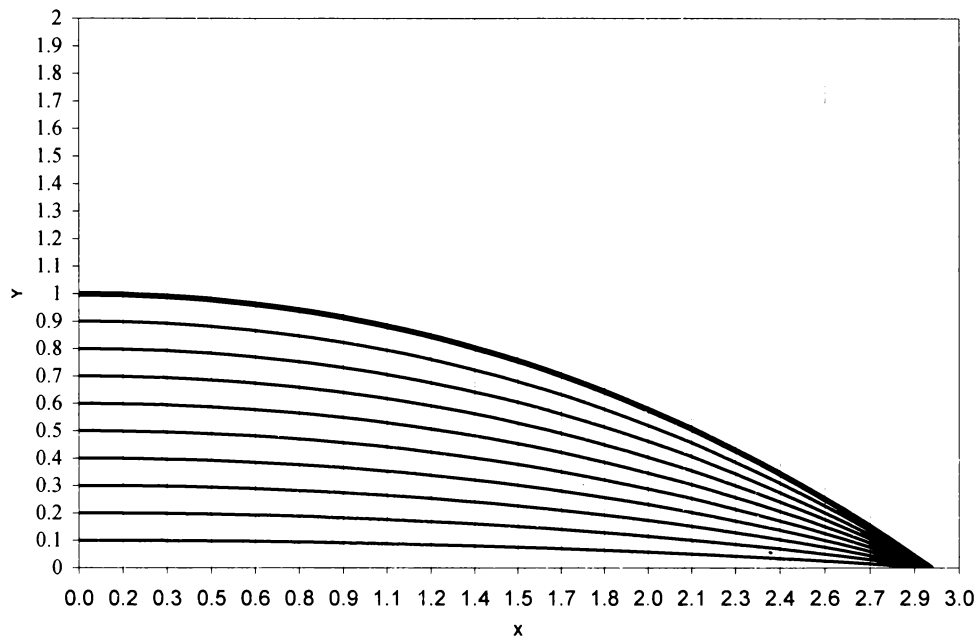


**Figure 18.** Rivulet - Physical Domain (Contact Angle,  $\beta = 38^\circ$ )



location of the phase-change front can be further resolved by applying the slushy cell liquid mass fraction, another output obtained from the subject numerical simulation. The results of doubling the grid density to 20 x 40 had negligible impact on the solution, and therefore the author retained the 10 x 20 grid density. The transformation variables employed are

$$X = \frac{x}{\delta}, \quad \Gamma = \frac{\xi(x)}{\delta} \quad \text{and the normalizing variable; } \eta = \frac{y}{\xi(x)}. \quad (4.2)$$

The resultant computational domain, shown in Figure 19, is a rectangular domain defined by the Cartesian coordinate pair  $(X, \eta)$ . At the contact line, where the rivulet, substrate and ambient fluid converge, one notices a singularity in the normalized coordinate,  $\eta$ . This concern arises because at  $x = R \sin(\beta)$  both the numerator and denominator of  $\eta$  vanish. However, l'Hopital's rule shows that as  $x \rightarrow R \sin(\beta)$ ,  $\eta \rightarrow 1$ . Therefore, a limit is defined at  $x = R \sin(\beta)$ , which validates the existence of the coordinate transformation at the contact line.

### **Primary Model Assumptions**

Recognizing that a model can only be as good, at best, as the underlying assumptions upon which it rests, the list of assumptions below is intended to provide a clear picture of which physical phenomena are included in the simulation and which are not.

- Thermal energy is transferred via isotropic heat conduction and convection. The effects of thermal radiation are considered negligible.

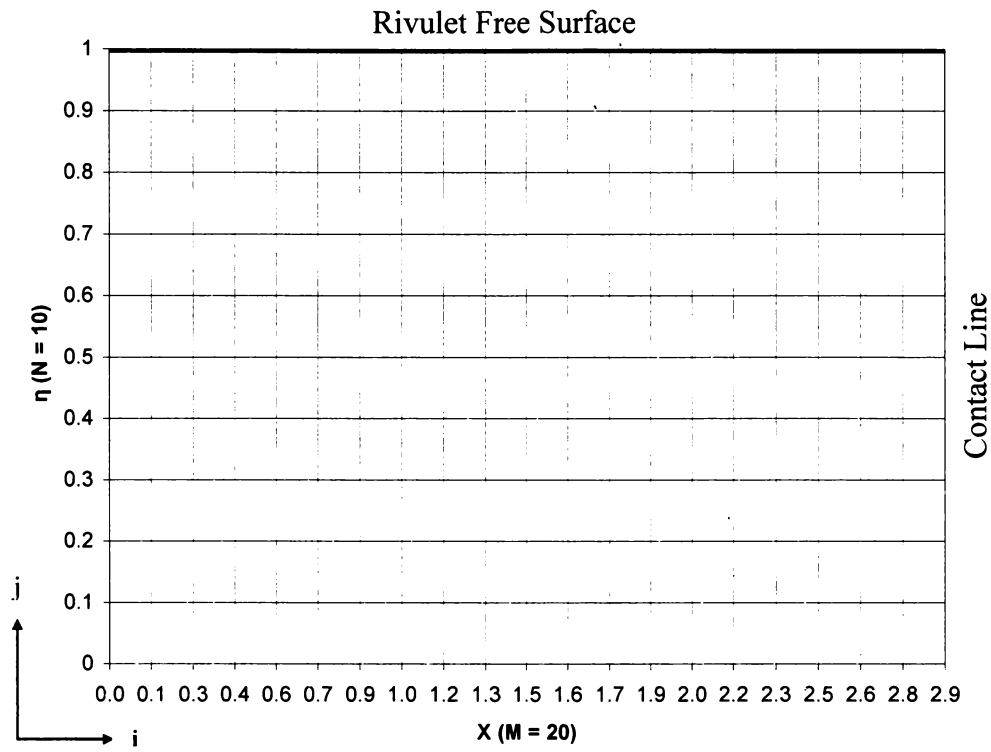


**Figure 19.** Rivulet - Computational Domain

- Mass is transferred to the environment via evaporation and sublimation at the free surface. Condensation, resulting in mass addition to the computational domain is also allowed.
- Gravitational effects were previously shown to be insignificant. Also, chemical and electromagnetic phenomena are deemed negligible.
- The latent heat of fusion,  $h_{ls}$ , for water is considered constant, and its release during the freezing process takes place at a constant phase-change temperature. The latent heats of vaporization and sublimation, employed in the mass transfer calculations at the free surface, are also constant.
- Nucleation and supercooling effects are considered unnecessary complexities in relation to the objectives of the subject research.
- As stated previously in the discussion of the “enthalpy method formulation”, the phase change takes place over a cell width rather than at a sharp surface. However, a natural result output from the “enthalpy method” is the liquid mass fraction within the “slushy” cell.
- Although, surface tension is a primary parameter of the rivulet geometry, its effects are only considered at the free surface interface between the liquid rivulet and the surrounding air. Thus, surface tension effects are not considered at the phase-change interface.

- All thermophysical properties are considered constant within their respective phases, while recognizing the important feature associated with the jump in properties across the phase-change cell, i.e.  $c_l \neq c_s$  and  $k_l \neq k_s$ .
- The density of the liquid phase is constant and equal to the density of the solid phase. The constancy of the phase densities is a very reasonable assumption given the relatively small temperature range over which the freezing rivulet process takes place. The equality of phase densities is a more gross assumption in that it does not allow for the movement of one phase relative to the other. This volume change, or in words, the ability of the ice to grow relative to the liquid upon freezing, adds a complexity to the model that is unnecessary for the scope of this study.
- Heat transfer in the “z” direction, or the streamwise direction, is negligible. In the case of the stationary rivulet, this assumption suggests that the temperature field is the same from one location to the next in the z-direction. Thus, each rivulet cross-sectional slice has an identical temperature distribution. Therefore, the solution need only be found for one rivulet slice, wherein heat is transferred in two dimensions, namely, the x-y plane. For the traveling rivulet, the same assumption is made based upon the Peclet number ( $Pe = RePr$ ). Given that for water  $Pe$  is large, heat conduction in the streamwise direction becomes negligible when compared to the other transport terms in the governing equations.

- The freestream atmosphere is considered to be at some specified relative humidity, up to 100% relative humidity.
- In the absence of an applicable value, a thermal contact resistance is not applied at the rivulet/wall interface, and perfect thermal contact is assumed. Although, the effects of contact resistance on the solution can be studied parametrically.

## **Governing Equations**

### **Physical Domain**

The governing energy transport equation for the stationary rivulet Stefan problem, when formulated using enthalpy as a dependent variable, becomes

$$\rho \frac{\partial h}{\partial t} = k \left[ \frac{\partial^2 T}{\partial x^2} + \frac{\partial^2 T}{\partial y^2} \right], \quad (4.3)$$

where  $k = k_s$  or  $k = k_l$  depending upon the associated phase.

The associated boundary conditions are as follows:

At  $x = 0$ , the plane of symmetry;

$$\left. \frac{\partial T}{\partial x} \right|_{x=0} = 0. \quad (4.4)$$

At the free surface, liquid/gas interface, the boundary condition is defined by equation (4.5), and the associated mass flux rate from the rivulet free surface is expressed by equations (4.9) and (4.10).

$$-k \frac{\partial T}{\partial \bar{n}} = \bar{h}_\infty (T_i - T_{rec}) + \dot{m}_{fs}'' h_{fs}, \quad \text{where}$$

$\bar{n}$  is the component normal to the free surface

$\bar{h}_\infty$  is the average convective heat transfer coefficient (4.5)

$T_i$  is the liquid/gas interface temperature

$T_{rec}$  is the recovery temperature

$\dot{m}_{fs}''$  is the mass flux at the free surface (evaporation or sublimation)

$h_{fs}$  is the latent heat (vaporization or sublimation) at the free surface.

At the contact line,  $x = R \sin(\beta)$ , and at the rivulet/substrate interface,  $y = 0$ ;

$$T = T_w, \quad \text{where } T_w \text{ is the constant substrate temperature.} \quad (4.6)$$

At the free surface, the convective heat transfer coefficient is based upon flat plate boundary layer theory, and is defined as [27],

$$\bar{h}_\infty = \frac{\bar{Nu} * k_g}{L}, \quad \text{where } \bar{Nu} = 0.664 Re_l^{1/2} Pr^{1/3} \quad (\text{Laminar Flow}) \quad (4.7)$$

$$\bar{Nu} = 0.037 Re_l^{4/5} Pr^{1/3} \quad (\text{Turbulent Flow})$$

The recovery temperature is defined as [28],

$$T_{rec} = T_\infty \left( 1 + \zeta \frac{\gamma - 1}{2} Ma_\infty^2 \right), \quad \text{where } \zeta = Pr^{1/2} \quad (\text{Laminar Flow}) \quad (4.8)$$

$$\zeta = Pr^{1/3} \quad (\text{Turbulent Flow})$$

The mass flux at the free surface is given, fundamentally, by

$$\dot{m}_{fs}'' = \bar{h}_m [\rho_{v,sat}(T_i) - \rho_{v,e}] \quad , \quad (4.9)$$

where  $\bar{h}_m$  is the average mass transfer coefficient,  $\rho_{v,sat}$  is the saturated vapor density at the rivulet free surface interface and  $\rho_{v,e}$  is the water vapor density at the edge of the gaseous medium boundary layer. Employing the ideal gas equation of state and the applicable Chilton-Colburn analogy [29], the relationship for the mass transfer rate at the free surface becomes

$$\dot{m}_{fs}'' = \frac{\bar{h}_m Mw}{\rho_{g,e} \bar{R} (c_{p,g} Le^{2/3})} \left( \frac{P_{sat,i}}{T_i} - \frac{P_{v,e}}{T_e} \right), \text{ where} \quad (4.10)$$

$P_{sat,i}$  is the saturation vapor pressure of water (or ice) at  $T_i$ , the local temperature at the free surface, and  $P_{v,e}$  is the water vapor pressure at the edge of the boundary layer of the adjacent gas stream.

The saturation vapor pressure of pure liquid water within the representative range of temperature is given by Al-Khalil [16] as

$$P_{sat,i} \text{ (Pa)} = 2337. \exp \left\{ 6789. \left( \frac{1.}{293.15} - \frac{1.}{T_i} \right) - 5.031 \ln \left( \frac{T_i}{293.15} \right) \right\} \quad (\text{liquid}). \quad (4.11)$$

The saturation vapor pressure for ice, presented by Willbanks and Schulz [30], is employed in this study. This relationship was converted to S.I. units for consistency and is given by

$$P_{sat,i} \text{ (Pa)} = 2.7845 \exp \left\{ 2.3 \left[ \begin{array}{l} \left( \frac{-2.4455646 \times 10^3}{T_e} + 0.4343 * 8.2312 \ln(T_e) \right) \\ - 1.677006 \times 10^{-2} T_e + 1.20514 \times 10^{-5} T_e^2 \\ - 6.757169 \end{array} \right] \right\} * 47.88 \text{ (ice).} \quad (4.12)$$

The fluid stream (or cloud) adjacent to the rivulet is populated with supercooled water droplets. The saturated vapor pressure of supercooled water,  $P_{sat,\infty}$ ; a relationship also found in the work of Willbanks and Schulz [30], is detailed below following unit conversion. Thus, the relationship for  $P_{sat,\infty}$  is:

$$P_{sat,\infty} \text{ (Pa)} = 2117. * \exp \left\{ 2.3 \left[ \begin{array}{l} \left[ 5.4266514 - \frac{2.0051 \times 10^3}{T_e} + \right. \\ \left. \left( 1.3869 \times 10^{-4} * \left( \frac{T_e^2 - 2.937 \times 10^5}{T_e} \right) \right) * A \right] \\ - 4.4 \times 10^{-3} * B \end{array} \right] \right\}, \text{ where}$$

$$A = 10^{\left[ 1.1965 \times 10^{-11} * (T_e^2 - 2.937 \times 10^5)^2 \right]} - 1.0 \quad (4.13)$$

$$B = 10^{\left[ -5.7148 \times 10^{-3} * (374.11 - T_e)^{125} \right]}$$

Finally, the water vapor pressure at the boundary layer edge is related to the saturation vapor pressure of the freestream by:

$$P_{v,e} = P_{sat,\infty} rh, \quad (4.14)$$



where  $rh$  is the relative humidity of the freestream air.

### Computational Domain

The transformation of the above governing equation and associated boundary conditions to the computational domain is presented. The independent spatial variables,  $x$  and  $y$ , were previously mapped to the non-dimensional coordinates,  $X$  and  $\eta$ , as part of the domain transformation. Frequently, however, in transient thermal analyses the temporal variable (or time) is non-dimensionalized using the Fourier number. The Fourier number defined as

$$F_o = \frac{t k}{\rho c_p \delta^2} \quad , \quad (4.15)$$

is not practical for use in the subject Stefan problem since the thermal conductivity and specific heat can vary from one side of a cell to the other. Therefore, the dependent variables and the independent spatial variables are non-dimensionalized, but the temporal variable remains dimensional. The non-dimensional dependent variables are:

$$\psi = \left( \frac{h - h_{mp,s}}{h_{ls}} \right), \text{ non - dimensional enthalpy} \quad , \quad (4.16)$$

$$\phi = \left( \frac{c_{p,s} (T - T_{mp})}{St_s h_{ls}} \right), \text{ non - dimensional temperature}$$

where  $h_{mp,s}$  ,  $h_{ls}$  and  $St_s$  are the enthalpy of the solid (ice) at the phase-change temperature, the latent heat of fusion and Stefan number respectively.

Upon transformation from the physical domain to the computational domain, the governing equation (4.3), becomes:

$$\frac{\partial \psi}{\partial t} = \frac{k}{\delta^2} C_w \left\{ \frac{\partial^2 \phi}{\partial X^2} + \frac{1}{\Gamma^2} \left( 1 + \left( \frac{d\xi}{dx} \right)^2 \eta^2 \right) \frac{\partial^2 \phi}{\partial \eta^2} + \frac{1}{\Gamma^2} \left( \frac{d\xi}{dx} \right)^2 \eta \frac{\partial \phi}{\partial \eta} \right\}, \text{ where} \quad (4.17)$$

$$C_w = \frac{\Delta T_{ref}}{\rho h_{ls}} \text{ and subsequently, } \Delta T_{ref} = \frac{St_s h_{ls}}{c_{p,s}} = (T_{mp} - T_w).$$

The constants  $C_w$ ,  $\Delta T_{ref}$  and  $\Gamma$  (see equation 4.2) were defined by the author to consolidate several of the coefficients that resulted as part of the transformation of the governing equations, thus simplifying the expressions. At the symmetry boundary, the boundary condition becomes:

$$\frac{\partial \phi}{\partial X} = 0, \text{ at } X = 0. \quad (4.18)$$

At the free surface (rivulet/gas interface), the boundary condition becomes:

$$\Gamma X \frac{\partial \phi}{\partial X} + \frac{\partial \phi}{\partial \eta} \eta \left( \Gamma - X \frac{d\xi}{dx} \right) = \frac{\Gamma}{\Delta T_{ref}} \left\{ -Bi_R (T_i - T_{rec}) - \frac{\dot{m}_{fs}^n h_{ph} R}{k} \right\}, \text{ at } \eta = 1.0,$$

$$\text{where } Bi_R = \frac{h_c R}{k} \text{ and } h_{ph} = h_{lv} \text{ if surface is liquid, or } h_{ph} = h_{sv} \text{ if surface is ice.} \quad (4.19)$$

In the two dimensional space, the ‘‘contact point’’ of the physical domain becomes a ‘‘contact line’’ in the computational domain. Accordingly, the contact line forms a boundary at  $X = X_{max}$  of the computational domain. The boundary condition at the

contact line is simply the wall (substrate) temperature. Therefore, the boundary condition at the contact line is equivalent to the boundary condition at the substrate surface, and is shown to be:

$$\phi = \frac{(T_w - T_{mp})}{\Delta T_{ref}} = -1.0 \text{ , at } X = X_{max} \text{ and } \eta = 0 . \quad (4.20)$$

With the governing equations properly defined in the coordinates of the computational domain, the problem now is to obtain a solution. The details of equation discretization and the numerical method applied are presented next.

### **Discretization and Numerical Solution Technique**

The inherent non-linearity and discontinuities at the phase-change interface of the freezing rivulet Stefan problem provide the impetus for employing the enthalpy method in the solution phase. Therefore, the governing equation, and associated boundary conditions have been formulated with enthalpy as a dependent variable. The solution set-up, including the discretization of the governing equation and boundary conditions is now discussed in detail. The reader is referred to Figure 20 wherein the computational domain is presented in discretized cell index notation. The solution is found over a computational domain with a dimension of MxN cells. The governing equation is solved at each cell node, which resides in the center of the cell. Cells that are adjacent to one or more boundaries are termed “boundary cells” and contain a central node, as well as, a boundary node(s). Boundary nodes lie strictly on the boundary itself, i.e. along  $i = 0$ ,  $i = 21$ ,  $j = 0$  and  $j = 11$ .

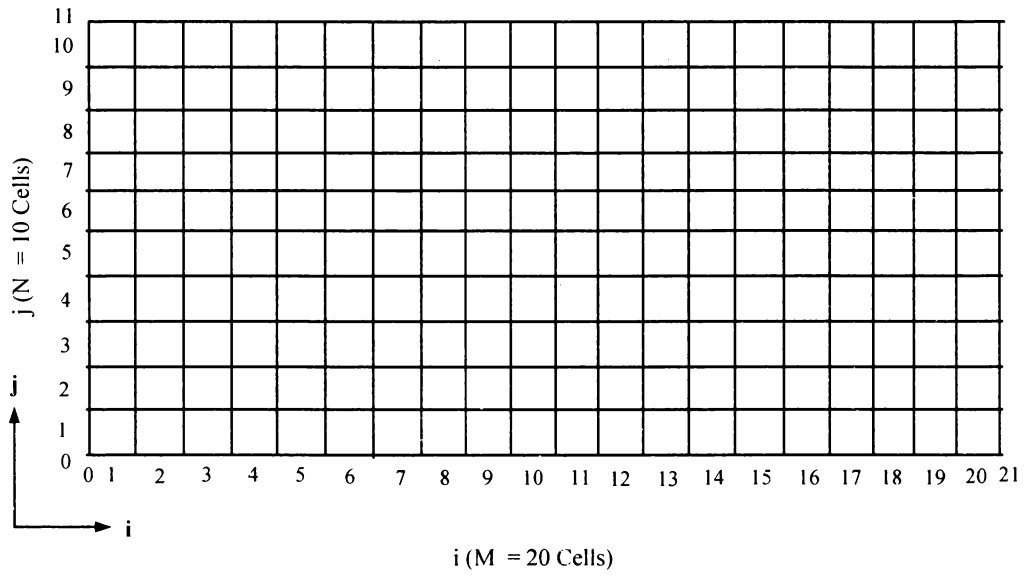


**Figure 20.** Computational Domain with Discretized Cell Index Notation

## Discretization

The discretization below represents a fully implicit form resulting in the necessity to solve a resultant system of equations. The desire for robustness and stability in the numerical solution is the motivation behind selecting a fully implicit numerical formulation. A convenient and physically consistent approach is to combine appropriate terms to form thermal resistances that manifest themselves in the denominator of the discretized equations. Utilizing the previously defined non-dimensional temperature,  $\phi$ , and applying an approach similar to the “Kirchoff transformation” [20], the functional relationship for the “Kirchoff temperature”,  $\phi_k$ , becomes

$$\phi_k = \left\{ \begin{array}{ll} \frac{k_s c_{p,s} (T - T_{mp})}{St_s h_{ls}}, & \text{if } T < T_{mp} \\ 0, & \text{if } T = T_{mp} \\ \frac{k_l c_{p,s} (T - T_{mp})}{St_s h_{ls}}, & \text{if } T > T_{mp} \end{array} \right\}. \quad (4.21)$$

The utility of the “Kirchoff temperature” is that it allows the thermal flux between neighboring cells to be nicely split, and each cell to have its own thermal resistance value. This concept is illustrated below for heat conduction between two neighboring cells. The heat flux across the interface of two cells is given by Fourier’s Law as

$$q_{i-1/2} = \frac{(\phi_{k,i-1} - \phi_{k,i})}{\Delta x} = \frac{\phi_{i-1}}{R_{i-1}} - \frac{\phi_i}{R_i}, \text{ where}$$

$$R_i = \frac{\Delta x}{k_i} \quad (4.22)$$

$\phi_{k,i} = k \phi_i$  is the Kirchoff temperature, and  
 $\phi$  is the non - dimensional temperature

Herein, each cell has its own thermal resistance, which is conveniently determined from the following relationship that employs the liquid mass fraction, mf:

$$R_i = \Delta x \left\{ \frac{mf_i}{k_l} + \frac{(1-mf_i)}{k_s} \right\}. \quad (4.23)$$

Clearly, if an adjacent cell is slushy, then accordingly,  $T_i = T_{mp}$  and the slushy cell does not contribute to the conduction. However, thermal energy is still transferred from the slushy cell to its neighbors via conduction, where the temperature potential and thermal resistance are defined in the heat flux equation of the neighboring cells. This is a natural artifice of the “Kirchoff temperature”, which is inherently referenced to the phase-change temperature  $T_{mp}$ . Additionally, this fact is consistent with the enthalpy method formulation, which considers a slushy cell to be isothermal at the phase-change temperature, but still exchanges thermal energy with its surroundings.

The fully implicit discretization of the governing equation for all cells within the computational domain except the symmetry boundary cells ( $i=1$ ) becomes

$$\begin{aligned}
\psi_{i,j}^{n+1} + \frac{\Delta t C_w}{(\delta^n)^2} \left\{ \frac{2}{\Delta X \bar{R}_{i,j}^{n+1}} + \frac{2 \left( 1 + \left( \frac{d\xi}{dx} \right)^2 \eta^2 \right)}{\Delta \eta \Gamma^2 \hat{R}_{i,j}^{n+1}} \right\} \phi_{i,j}^{n+1} = \psi_{i,j}^n + \\
\frac{\Delta t C_w}{(\delta^n)^2} \left\{ \frac{1}{\Delta X} \left[ \frac{\phi_{i-1,j}^{n+1}}{\bar{R}_{i-1,j}^{n+1}} + \frac{\phi_{i+1,j}^{n+1}}{\bar{R}_{i+1,j}^{n+1}} \right] + \frac{\left( \frac{d\xi}{dx} \right)^2 \eta}{2\Gamma^2} \left[ \frac{\phi_{i,j+1}^{n+1}}{\hat{R}_{i,j+1}^{n+1}} - \frac{\phi_{i,j-1}^{n+1}}{\hat{R}_{i,j-1}^{n+1}} \right] + \right. \\
\left. \frac{\left( 1 + \left( \frac{d\xi}{dx} \right)^2 \eta^2 \right)}{\Delta \eta \Gamma^2} \left[ \frac{\phi_{i,j-1}^{n+1}}{\hat{R}_{i,j-1}^{n+1}} + \frac{\phi_{i,j+1}^{n+1}}{\hat{R}_{i,j+1}^{n+1}} \right] \right\}, \tag{4.24}
\end{aligned}$$

for  $2 \leq i \leq M$  and  $1 \leq j \leq N$ , and where  $\bar{R}_{i,j}$  is the thermal resistance in the X direction and  $\hat{R}_{i,j}$  is the thermal resistance in the  $\eta$  direction. The discretization employs a “five” cell stencil.

For the symmetry boundary cells ( $i=1$ ), the backward difference is zero due to the zero gradient at the symmetry boundary ( $i=0$ ) nodes. Thus, for the symmetry boundary cells, equation (4.24) becomes

$$\begin{aligned}
& \psi_{i,j}^{n+1} + \frac{\Delta t C_w}{(\delta^n)^2} \left\{ \frac{1}{\Delta X \bar{R}_{i,j}^{n+1}} + \frac{2 \left( 1 + \left( \frac{d\xi}{dx} \right)^2 \eta^2 \right)}{\Delta \eta \Gamma^2 \hat{R}_{i,j}^{n+1}} \right\} \phi_{i,j}^{n+1} = \psi_{i,j}^n + \\
& \frac{\Delta t C_w}{(\delta^n)^2} \left\{ \frac{1}{\Delta X} \left[ \frac{\phi_{i+1,j}^{n+1}}{\bar{R}_{i+1,j}^{n+1}} \right] + \frac{\left( \frac{d\xi}{dx} \right)^2 \eta}{2\Gamma^2} \left[ \frac{\phi_{i,j+1}^{n+1}}{\hat{R}_{i,j+1}^{n+1}} - \frac{\phi_{i,j-1}^{n+1}}{\hat{R}_{i,j-1}^{n+1}} \right] + \right. \\
& \left. \frac{\left( 1 + \left( \frac{d\xi}{dx} \right)^2 \eta^2 \right)}{\Delta \eta \Gamma^2} \left[ \frac{\phi_{i,j-1}^{n+1}}{\hat{R}_{i,j-1}^{n+1}} + \frac{\phi_{i,j+1}^{n+1}}{\hat{R}_{i,j+1}^{n+1}} \right] \right\}, \quad (4.25)
\end{aligned}$$

for  $i=1$  and  $1 \leq j \leq N$ .

A “middle” three-point formula [31] was used in the representation of the single derivative terms. Therefore, in the evaluation of the single derivatives, the function  $\phi$  need only be evaluated at the nodes on either side and adjacent to the node of interest.

In accordance with equation (4.23), the directional thermal resistances at each node are of the form

$$\begin{aligned}
\bar{R}_{i,j}^{n+1} &= \Delta X \left\{ \frac{mf_{i,j}^{n+1}}{k_l} + \frac{(1 - mf_{i,j}^{n+1})}{k_s} \right\}, \quad 1 \leq i \leq M \text{ and } 1 \leq j \leq N. \quad (4.26) \\
\hat{R}_{i,j}^{n+1} &= \Delta \eta \left\{ \frac{mf_{i,j}^{n+1}}{k_l} + \frac{(1 - mf_{i,j}^{n+1})}{k_s} \right\}
\end{aligned}$$

When the a solution is being computed at the nodes residing within the boundary cells at  $i=1$ ,  $i=M$ ,  $j=1$  and  $j=N$ , the functional relationship for the node resistances become



$$\begin{aligned}
\bar{R}_{1,j}^{n+1} &= \Delta X \left\{ \frac{mf_{1,j}^{n+1}}{k_l} + \frac{(1-mf_{1,j}^{n+1})}{k_s} \right\}, \quad i=1 \text{ and } 1 \leq j \leq N \\
\hat{R}_{1,j}^{n+1} &= \Delta \eta \left\{ \frac{mf_{1,j}^{n+1}}{k_l} + \frac{(1-mf_{1,j}^{n+1})}{k_s} \right\}, \quad i=1 \text{ and } 1 < j < N \\
\hat{R}_{M,j}^{n+1} &= \Delta \eta \left\{ \frac{mf_{M,j}^{n+1}}{k_l} + \frac{(1-mf_{M,j}^{n+1})}{k_s} \right\}, \quad i=M \text{ and } 1 < j < N \\
\bar{R}_{i,1}^{n+1} &= \Delta X \left\{ \frac{mf_{i,1}^{n+1}}{k_l} + \frac{(1-mf_{i,1}^{n+1})}{k_s} \right\}, \quad 1 < i < M \text{ and } j=1 \\
\bar{R}_{i,N}^{n+1} &= \Delta X \left\{ \frac{mf_{i,N}^{n+1}}{k_l} + \frac{(1-mf_{i,N}^{n+1})}{k_s} \right\}, \quad 1 < i < M \text{ and } j=N \\
\bar{R}_{M,j}^{n+1} &= \frac{2\Delta X}{3} \left\{ \frac{mf_{M,j}^{n+1}}{k_l} + \frac{(1-mf_{M,j}^{n+1})}{k_s} \right\}, \quad i=M \text{ and } 1 \leq j \leq N \\
\hat{R}_{i,1}^{n+1} &= \frac{2\Delta \eta}{3} \left\{ \frac{mf_{i,1}^{n+1}}{k_l} + \frac{(1-mf_{i,1}^{n+1})}{k_s} \right\}, \quad 1 \leq i \leq M \text{ and } j=1, \quad (4.27) \\
\hat{R}_{i,N}^{n+1} &= \frac{2\Delta \eta}{3} \left\{ \frac{mf_{i,N}^{n+1}}{k_l} + \frac{(1-mf_{i,N}^{n+1})}{k_s} \right\}, \quad 1 \leq i \leq M \text{ and } j=N
\end{aligned}$$

otherwise, they are defined according to equation (4.26). The nodal thermal resistances associated with the boundaries at  $i=M+1, j=0$  and  $j=N+1$ , likewise are uniquely defined by

$$\begin{aligned}
\bar{R}_{M+1,j}^{n+1} &= \frac{\Delta X}{2} \left\{ \frac{mf_{M,j}^{n+1}}{k_l} + \frac{(1-mf_{M,j}^{n+1})}{k_s} \right\}, \quad i=M+1 \text{ and } 1 \leq j \leq N \\
\hat{R}_{i,0}^{n+1} &= \frac{\Delta \eta}{2} \left\{ \frac{mf_{i,1}^{n+1}}{k_l} + \frac{(1-mf_{i,1}^{n+1})}{k_s} \right\}, \quad 1 \leq i \leq M \text{ and } j=0 \quad (4.28) \\
\hat{R}_{i,N+1}^{n+1} &= \frac{\Delta \eta}{2} \left\{ \frac{mf_{i,N}^{n+1}}{k_l} + \frac{(1-mf_{i,N}^{n+1})}{k_s} \right\}, \quad 1 \leq i \leq M \text{ and } j=N+1
\end{aligned}$$

A unique thermal resistance definition for the symmetry boundary is not necessary since physical nodes along this boundary are not required in the solution, wherein the condition is invoked mathematically.

The discretized boundary condition equations, beginning with the symmetry boundary, are

$$\begin{aligned} \phi_{0,j}^{n+1} &= \phi_{1,j}^{n+1}, \\ i &= 0 \text{ and } 1 \leq j \leq N \text{ (Symmetry Boundary)} \\ \Gamma X \left[ \frac{\phi_{i+1,N+1}^{n+1} - \phi_{i,N+1}^{n+1}}{\Delta X} \right] + \eta \left( \Gamma - X \frac{d\xi}{dx} \right) \left[ \frac{\phi_{i,N+1}^{n+1} - \phi_{i,N}^{n+1}}{0.5 \Delta \eta} \right] &= \\ - \frac{\Gamma Bi_R}{\Delta T_{ref}} \left[ (T_{i,N+1}^n - T_{rec}) + \frac{\dot{m}'' h_{ph}}{h_c} \right], \\ 1 \leq i \leq M \text{ and } j = N + 1 \text{ (Rivulet Free Surface)}. \end{aligned} \quad (4.29)$$

$$\begin{aligned} \phi_{M+1,j}^{n+1} &= 1.0, \\ i &= M + 1 \text{ and } 1 \leq j \leq N + 1 \text{ (Rivulet Contact Line)} \end{aligned}$$

$$\begin{aligned} \phi_{i,0}^{n+1} &= 1.0, \\ 1 \leq i \leq M \text{ and } j = 0 \text{ (Substrate Wall)} \end{aligned}$$

### Numerical Solution Technique

The solution to the freezing rivulet Stefan problem requires solving a system of equations at each computational time step. The Gauss-Seidel iterative method was chosen as the numerical method for solving the subject finite difference equations. This method solves the (i,j)-th equation for the (i,j)-th unknown dependent variable utilizing the latest values available for all other variables. In the equations to follow, the (i,j)-th

dependent variable is updated with the new value just obtained from the solution of the (i,j)-th equation, which results in a point-by-point successive substitution technique. As shown above in the discretized equation, “n+1” as the superscript denotes the computational time increment for which a solution is desired. Given that the Gauss-Seidel method employs an iterative process within each “n+1” computational time step, “p+1” is used as the variable superscript to denote the Gauss-Seidel iteration number. A given Gauss-Seidel iteration sequence proceeds until a user specified convergence tolerance is achieved. For illustrative purposes, the governing equation (4.24) is shown below cast in Gauss-Seidel iteration notation. Figure 21 shows the five-cell stencil configuration employed in the discretization of the governing equations. Gauss-Seidel iterative superscripts are also attached to the nodal temperatures.

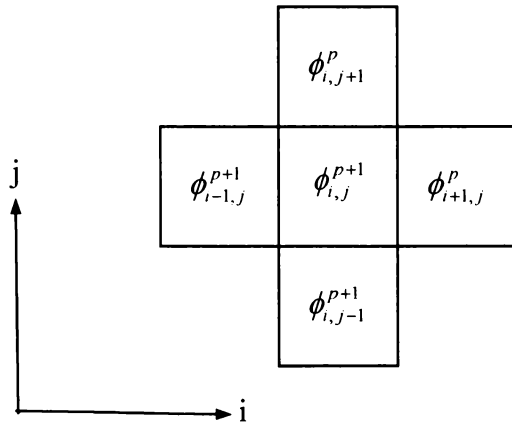


**Figure 21.** Five-Cell Computational Stencil With Gauss-Seidel Iterative Notation

Equation (4.24) becomes

$$\psi_{i,j}^{p+1} + \frac{\Delta t C_w}{(\delta^p)^2} \left\{ \frac{2}{\Delta X \bar{R}_{i,j}^p} + \frac{2 \left( 1 + \left( \frac{d\xi}{dx} \right)^2 \eta^2 \right)}{\Delta \eta \Gamma^2 \hat{R}_{i,j}^p} \right\} \phi_{i,j}^{p+1} = \psi_{i,j}^p + \frac{\Delta t C_w}{(\delta^p)^2} \left\{ \frac{1}{\Delta X} \left[ \frac{\phi_{i-1,j}^{p+1}}{\bar{R}_{i-1,j}^p} + \frac{\phi_{i+1,j}^p}{\bar{R}_{i+1,j}^p} \right] + \frac{\left( \frac{d\xi}{dx} \right)^2 \eta}{2\Gamma^2} \left[ \frac{\phi_{i,j+1}^p}{\hat{R}_{i,j+1}^p} - \frac{\phi_{i,j-1}^{p+1}}{\hat{R}_{i,j-1}^p} \right] + \frac{\left( 1 + \left( \frac{d\xi}{dx} \right)^2 \eta^2 \right)}{\Delta \eta \Gamma^2} \left[ \frac{\phi_{i,j-1}^{p+1}}{\hat{R}_{i,j-1}^p} + \frac{\phi_{i,j+1}^p}{\hat{R}_{i,j+1}^p} \right] \right\}, \quad (4.30)$$

for  $2 \leq i \leq M$  and  $1 \leq j \leq N$ .

Note that the variables  $\phi_{i-1,j}^{p+1}$  and  $\phi_{i,j-1}^{p+1}$  from the right hand side of equation (4.30) are known values because they were evaluated when the (i-1,j)-th and (i,j-1)-th equations were solved. Thus, the only unknowns are  $\psi_{i,j}^{p+1}$  and  $\phi_{i,j}^{p+1}$  on the left hand side of equation (4.30). However, the enthalpy,  $\psi_{i,j}^{p+1}$ , is a function of the temperature,  $\phi_{i,j}^{p+1}$ , wherein again the non-linearity of the system is exhibited.

Introducing the variables “Z” and “C”, and setting them equal to the right hand side of equation (4.30) and the coefficient of  $\phi_{i,j}^{p+1}$ , respectively, then equation (4.30) can be written as

$$\psi_{i,j}^{p+1} + C_{i,j}^p \phi_{i,j}^{p+1} = Z_{i,j}^p. \quad (4.31)$$

The power of the enthalpy method formulation is manifest by applying the equation of state that relates enthalpy and temperature and solving for the unknown nodal temperature. Thus, employing equation (4.31), the enthalpy equation of state and the criteria pertaining to the physical phases of liquid, slushy and solid, the phase of a given cell is determined by the parameter  $Z_{i,j}^p$ . The functional relationship for the nodal (cell) non-dimensional temperature now becomes

$$\phi_{i,j}^{p+1} = \begin{cases} \frac{Z_{i,j}^p}{St_s C_{i,j}^p}, & \text{if } Z_{i,j}^p \leq 0 \\ 0, & \text{if } 0 \leq Z_{i,j}^p < 1 \\ \frac{Z_{i,j}^p - 1}{\frac{c_{p,l}}{c_{p,s}} St_s + C_{i,j}^p}, & \text{if } Z_{i,j}^p \geq 1 \end{cases} \quad (4.32)$$

Once the convergence criterion is met, the newly obtained nodal temperatures are used to solve for the up-dated cell enthalpies according to

$$\psi_{i,j}^{n+1} = Z_{i,j} - C_{i,j}^p \phi_{i,j}^{n+1}. \quad (4.33)$$

In the actual mechanics of the computations, the author employed a mathematical functional representation of equation (4.32) that allows a single continuous function to be

solved for  $\phi_{i,j}^{p+1}$ . By accurately representing the three-component relationship for  $\phi_{i,j}^{p+1}$  with one continuous function, computational efficiency is enhanced. Thus, the need to query to determine a priori if  $Z_{i,j}^p \leq 0$ ,  $0 \leq Z_{i,j}^p < 1$ , or  $Z_{i,j}^p \geq 1$  is eliminated. The relationship between  $\phi_{i,j}^{p+1}$  and  $Z_{i,j}^p$  is now expressed by [32]

$$\phi_{i,j}^{p+1} = \frac{Z_{i,j}^p}{St_s + C_{i,j}^p} - \frac{Z_{i,j}^p}{St_s + C_{i,j}^p} \left[ \frac{1.}{(1. + e^{-D(Z_{i,j}^p - a)})} \right] + \frac{Z_{i,j}^p}{\frac{c_{p,l}}{c_{p,s}} St_s + C_{i,j}^p} \left[ \frac{1.}{(1. + e^{-D(Z_{i,j}^p - b)})} \right], \quad (4.34)$$

where  $a = 0.0$ ,  $b = 1.0$  and  $D = 5000$ . The constants “a” and “b” represent the bounds on  $Z_{i,j}$  when the cell is slushy, or  $\phi_{i,j}^{p+1}$  equals zero. The constant “D” is simply a weighting factor, the value of which was obtained by trial and error. A graphical representation of equation (4.34) is shown in Figure 22. Once the new enthalpy is obtained from equation (4.33), the new liquid mass fraction of the cell is obtained in a similar manner to equation (4.34) for  $\phi_{i,j}^{p+1}$ . The liquid mass fraction,  $mf_{i,j}^{p+1}$ , is found from

$$mf_{i,j}^{p+1} = \psi_{i,j}^{p+1} \left[ \frac{1.}{(1. + e^{-D(\psi_{i,j}^{p+1} - a)})} \right] - (\psi_{i,j}^{p+1} - 1.) \left[ \frac{1.}{(1. + e^{-D(\psi_{i,j}^{p+1} - b)})} \right], \quad (4.35)$$

where again  $a = 0.0$ ,  $b = 1.0$  and  $D = 5000$ .

A top-level flow chart illustrating the solution process is shown in Figure 23, with the shaded areas depicting the primary computational blocks. The convergence criterion

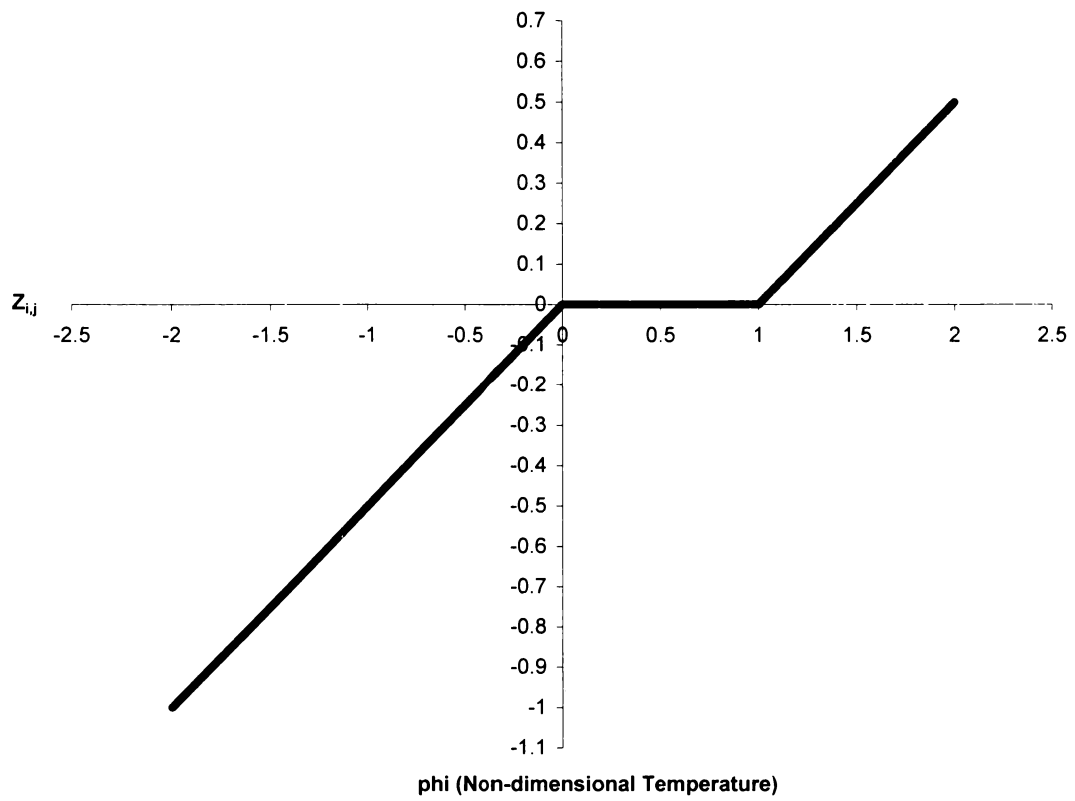


**Figure 22.** Graphical Representation of Equation (4.34)

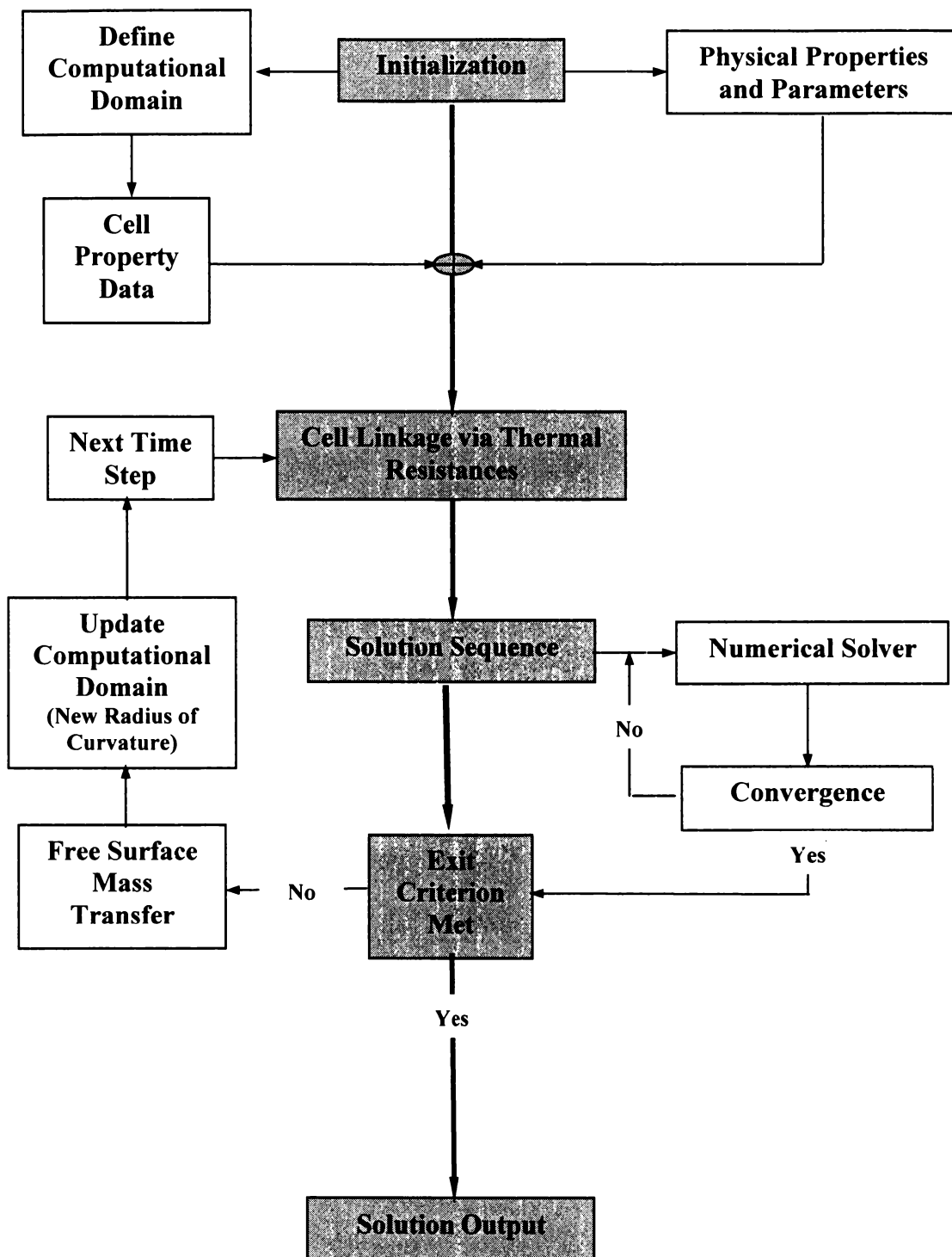


**Figure 23.** Freezing Stationary Rivulet Solution Flow Chart



is based upon a user specified error tolerance that defines the maximum tolerance over all  $\phi_{i,j}$ . The convergence criterion takes the form of

$$\text{Max.} \left| \phi_{i,j}^{p+1} - \phi_{i,j}^p \right| < \text{Error Tolerance, for all } \phi_{i,j}. \quad (4.36)$$

After each  $\phi_{i,j}^{p+1}$  has met the above criterion, the Gauss-Seidel iteration sequence is considered converged and the solution marches on to the next n+1 time step. The exit criterion requirement shown in Figure 23 is, at a minimum, the time corresponding to a completely frozen rivulet. The user may, however, desire to forego exiting the program until further cooling of the rivulet has taken place, or when a steady state condition is met.

#### Thermo-Physical Properties

The thermo-physical properties of the stationary rivulets were held constant with values corresponding to the phase-change temperature of 273.15 K [33]. Several of the key properties are listed below for reference purposes.

- Density (Liquid/Ice): 0.999 g/cm<sup>3</sup>
- Specific Heat (Liquid): 4.218 J/g-K
- Specific Heat (Ice): 2.028 J/g-K
- Thermal Conductivity (Liquid): 5.54 x 10<sup>-3</sup> W/cm-K
- Thermal Conductivity (Ice): 22.4 x 10<sup>-3</sup> W/cm-K
- Heat of Vaporization: 2.5 x 10<sup>3</sup> J/g
- Heat of Fusion: 3.336 x 10<sup>2</sup> J/g

- Heat of Sublimation:  $2.833 \times 10^3 \text{ J/g}$

Other pertinent thermo-physical property values will be highlighted, as necessary, in the next chapter that addresses the “running rivulet” model.

### **Freezing Stationary Rivulet Results**

Six experimental rivulet cases were showcased as part of the experimental investigation results of Chapter III, namely cases 1-C, 3-C, 4-C, 7-A, 7-C and NASAIR. Four of these six cases, specifically 1-C, 3-C, 4-C and 7-C were used here in the simulation of the freezing of stationary rivulets. Case 9-C was added to the stationary freezing rivulet simulation results to provide a second rivulet case with a  $60^\circ$  contact angle, but with different initial and environmental conditions. Additionally, two cases having the same initial and environmental conditions as Case 3-C, but with different boundary conditions were added. These two cases, namely 3-C\_a and 3-C\_b, highlight the effects of an adiabatic boundary condition at the wall, and a non-evaporative condition at the rivulet free surface, respectively.

### **Phase-Change Front Propagation**

The phase-change front propagation results for the seven cases are plotted in Figures 24-30. The results are shown in the physical domain, again, with symmetry invoked. The rivulet physical properties, initial temperature and environmental parameters are summarized in Table 2 below. In Table 2, the following definitions are applicable.

**Table 2.** Rivulet Conditions and Parameters for the Stationary Rivulet Cases

<b>Case</b>	<b><math>t_f</math></b>	<b><math>T_w</math></b>	<b><math>T_{in}</math></b>	<b><math>T_{inf}</math></b>	<b>Ste</b>	<b>rh</b>	<b><math>\beta</math></b>	<b><math>w_r</math></b>	<b><math>U_{inf}</math></b>
	(sec.)	(K)	(K)	(K)	-	%	(deg.)	(mm)	(m/s)
1-C	3.0	272.9	276.7	271.1	0.00158	80.8	38	1.0	44.7
3-C	0.74	270.6	273.4	268.9	0.0155	82.7	38	1.0	45.1
4-C	0.76	271.1	273.2	268.7	0.0125	87.2	38	1.0	67.2
7-C	4.07	270.7	276.3	269.0	0.0147	83.3	60	1.5	44.7
9-C	5.51	270.2	277.2	267.7	0.0179	86.1	60	2.0	67.0
3-C <sub>a</sub>	$\gg 1.0$	$T_{i,1}^*$	273.4	268.9	0.0155	82.7	38	1.0	45.1
3-C <sub>b</sub>	0.84	270.6	273.4	268.9	0.0155	82.7	38	1.0	45.1

\* Adiabatic wall boundary:  $T_w$  equal to the cell temperature one node off the wall,  $T_{i,1}$ .

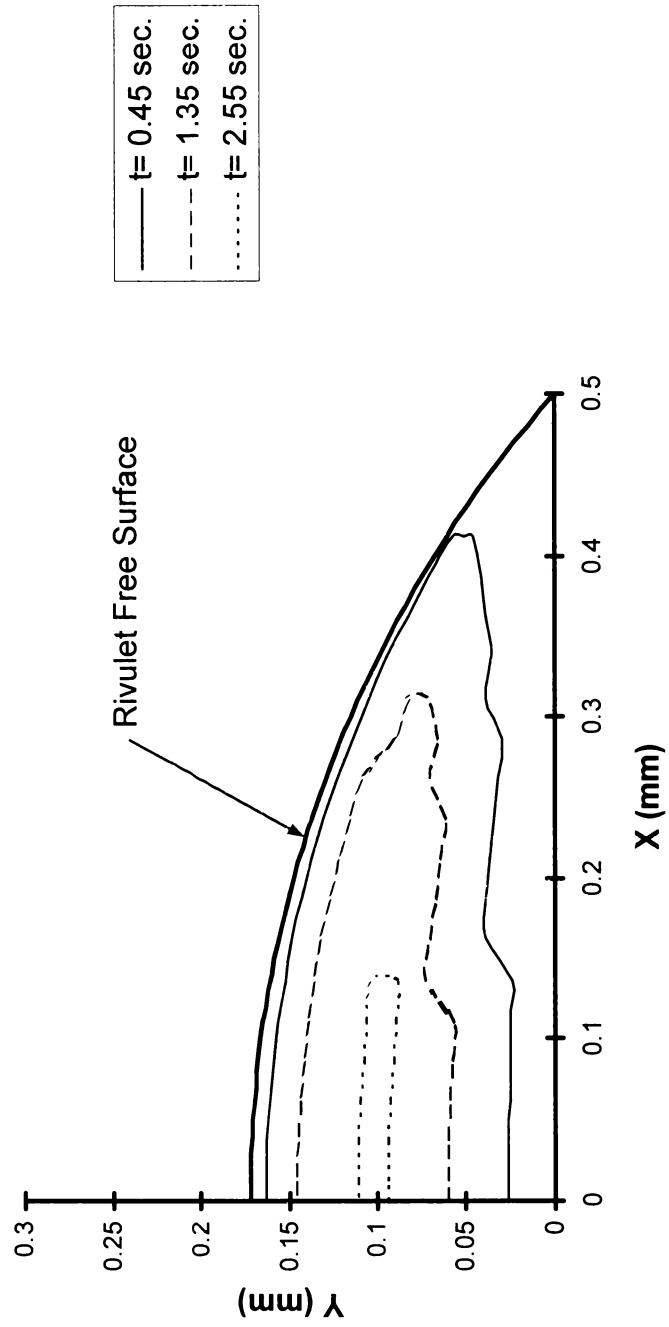


**Figure 24.** Case 1-C Stationary Freezing Rivulet

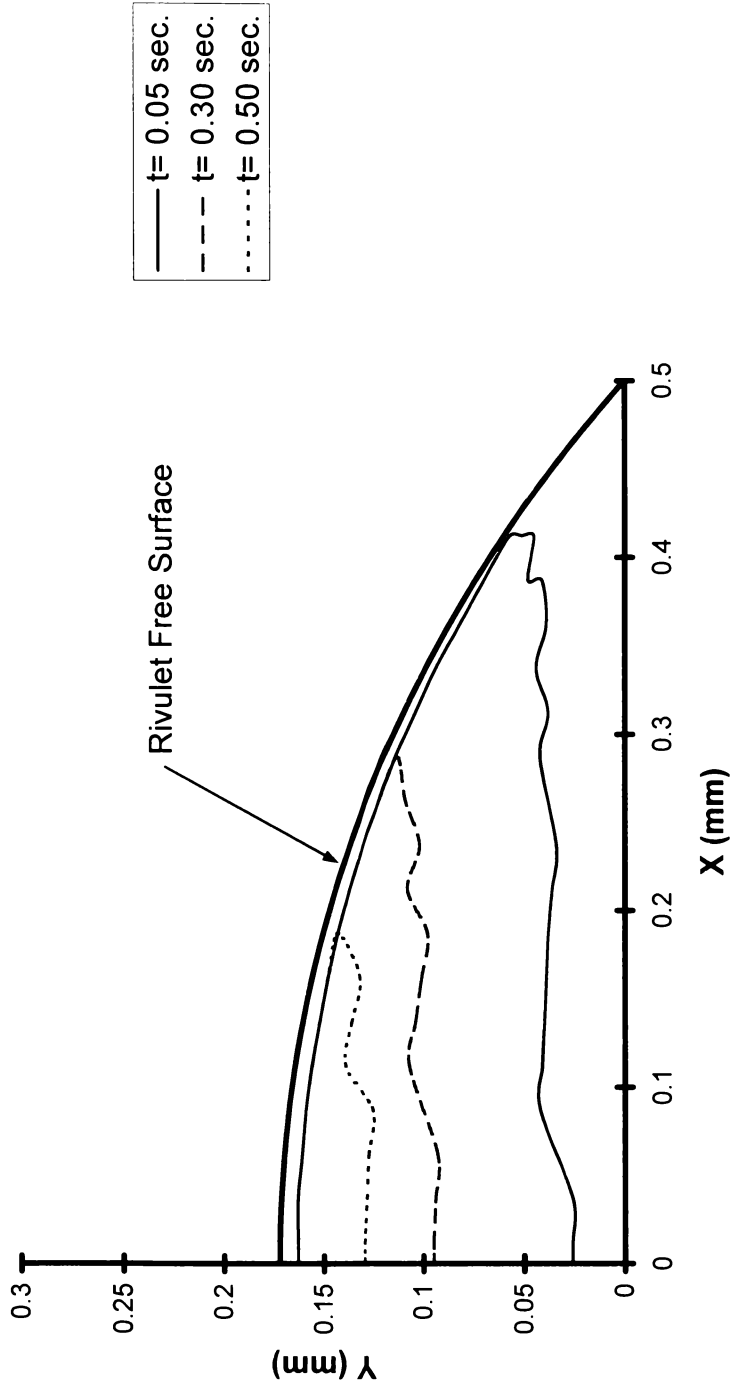


**Figure 25.** Case 3-C Stationary Freezing Rivulet

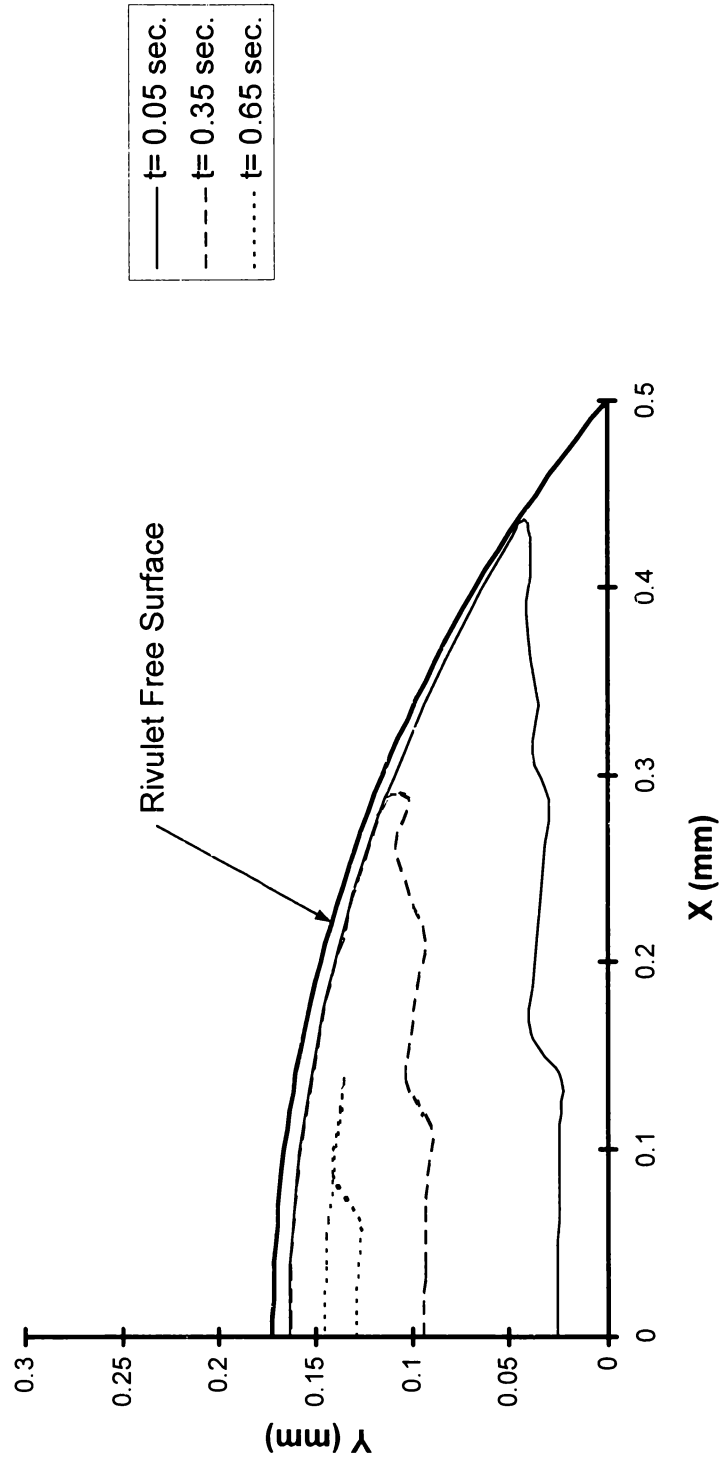


**Figure 26.** Case 4-C Stationary Freezing Rivulet

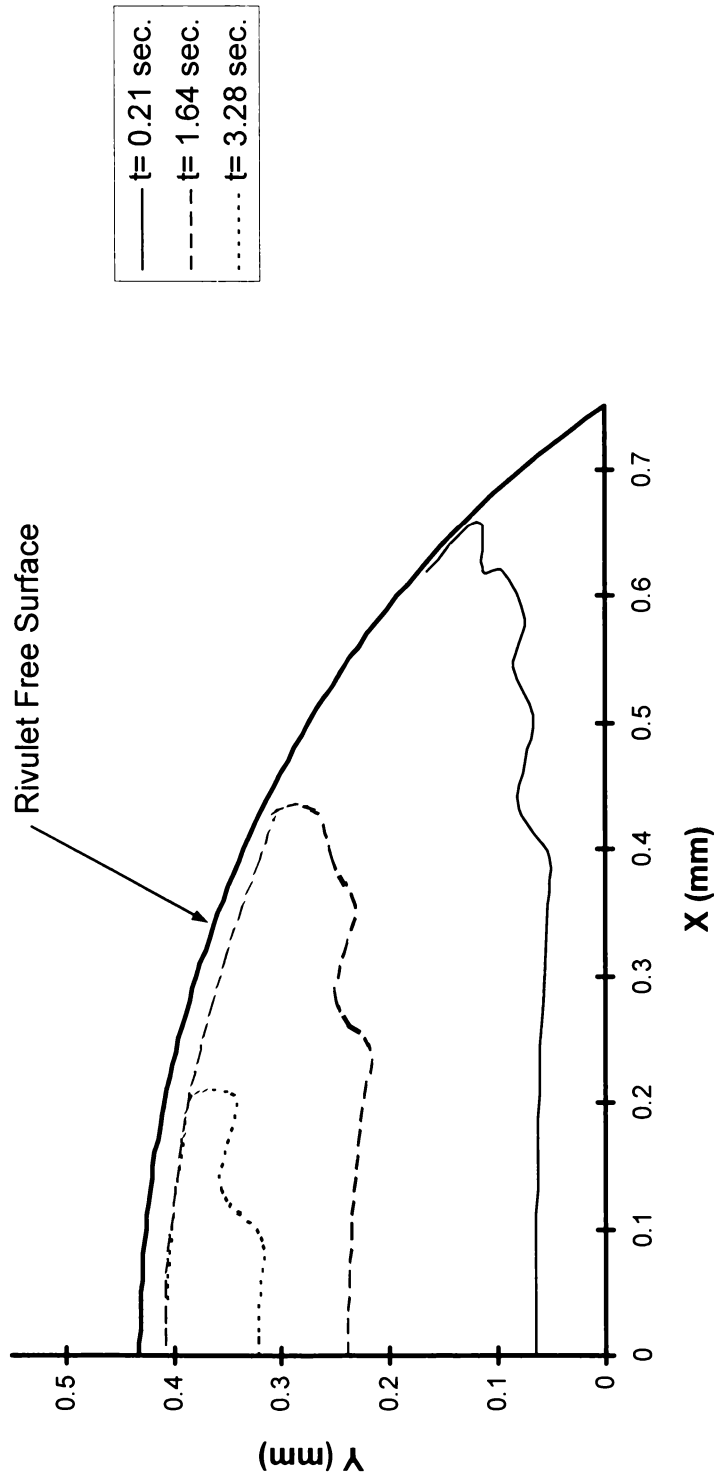


**Figure 27.** Case 7-C Stationary Freezing Rivulet

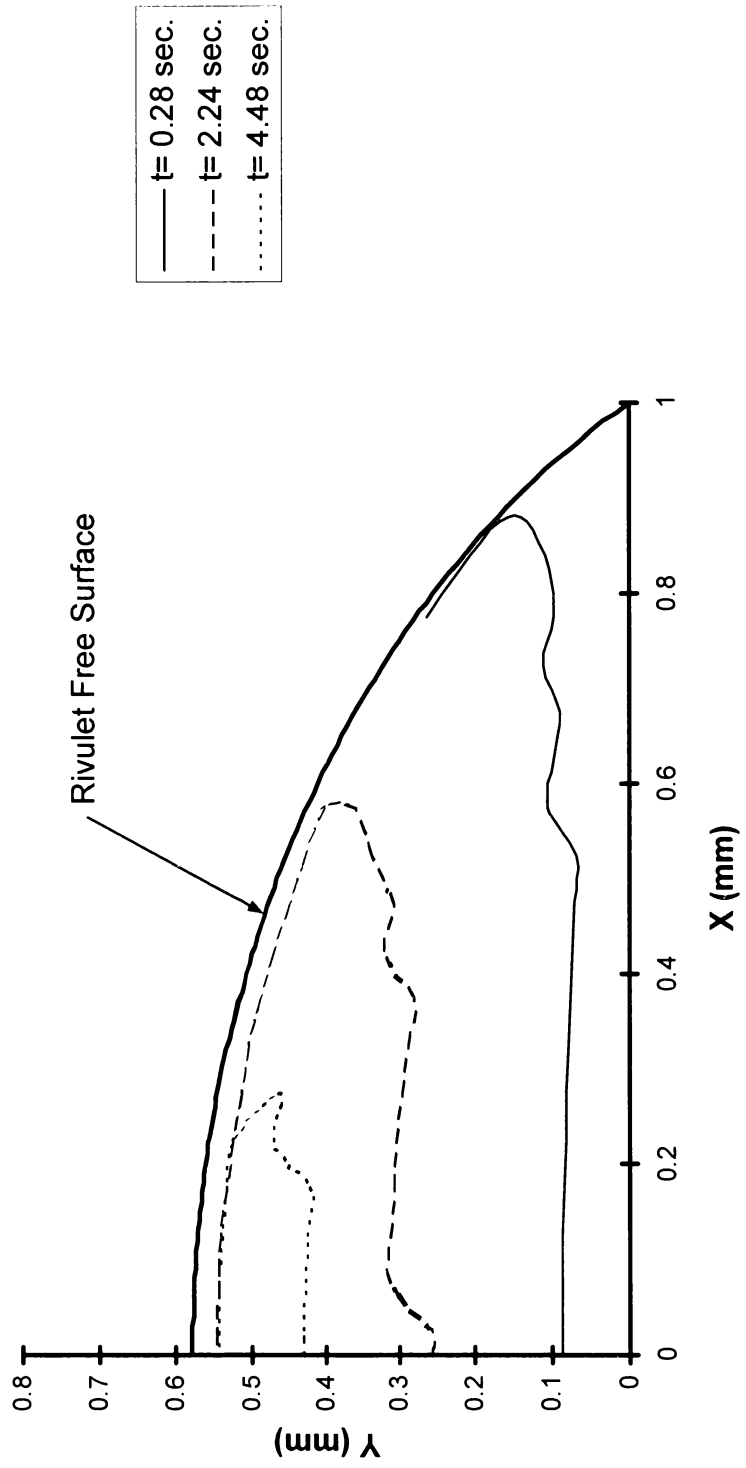


**Figure 28.** Case 9-C Stationary Freezing Rivulet



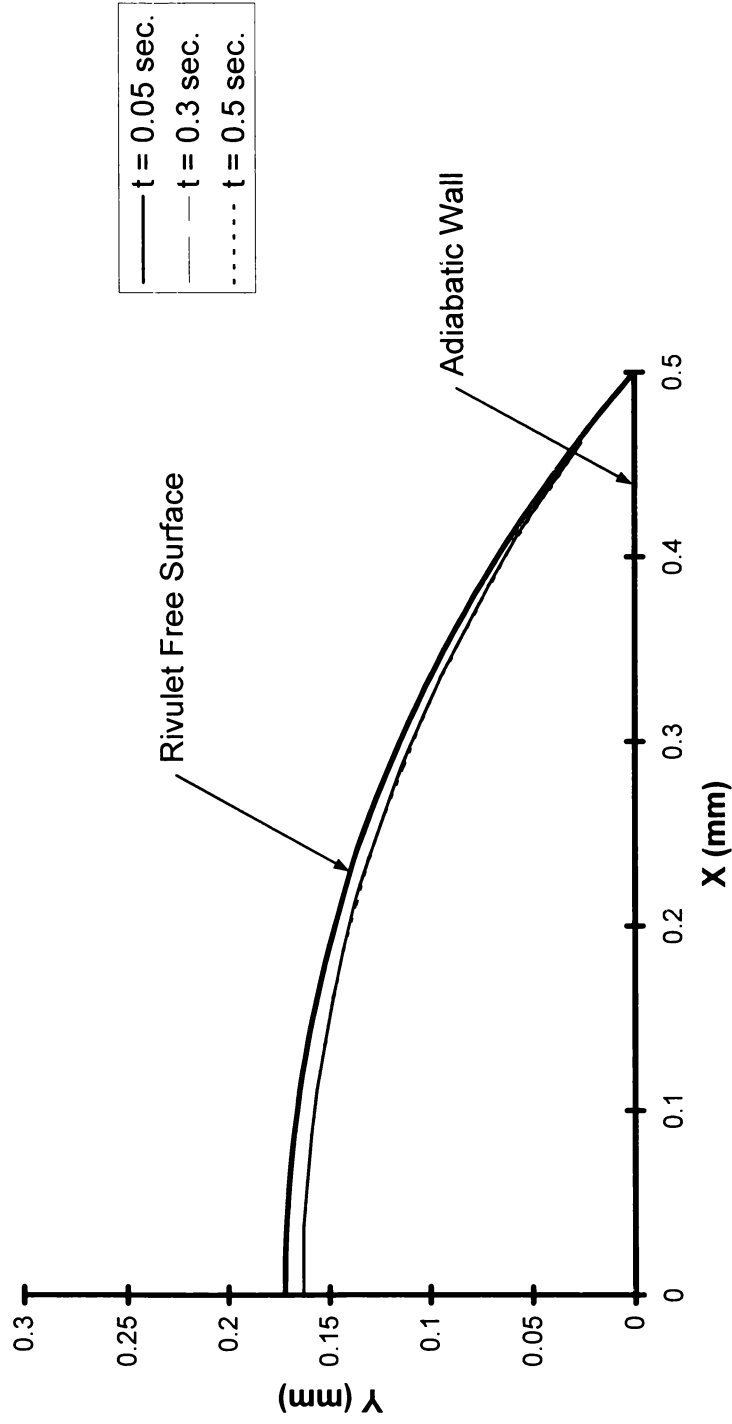


**Figure 29.** Case 3-C\_a: Case 3-C Rivulet With Adiabatic Wall Boundary Condition

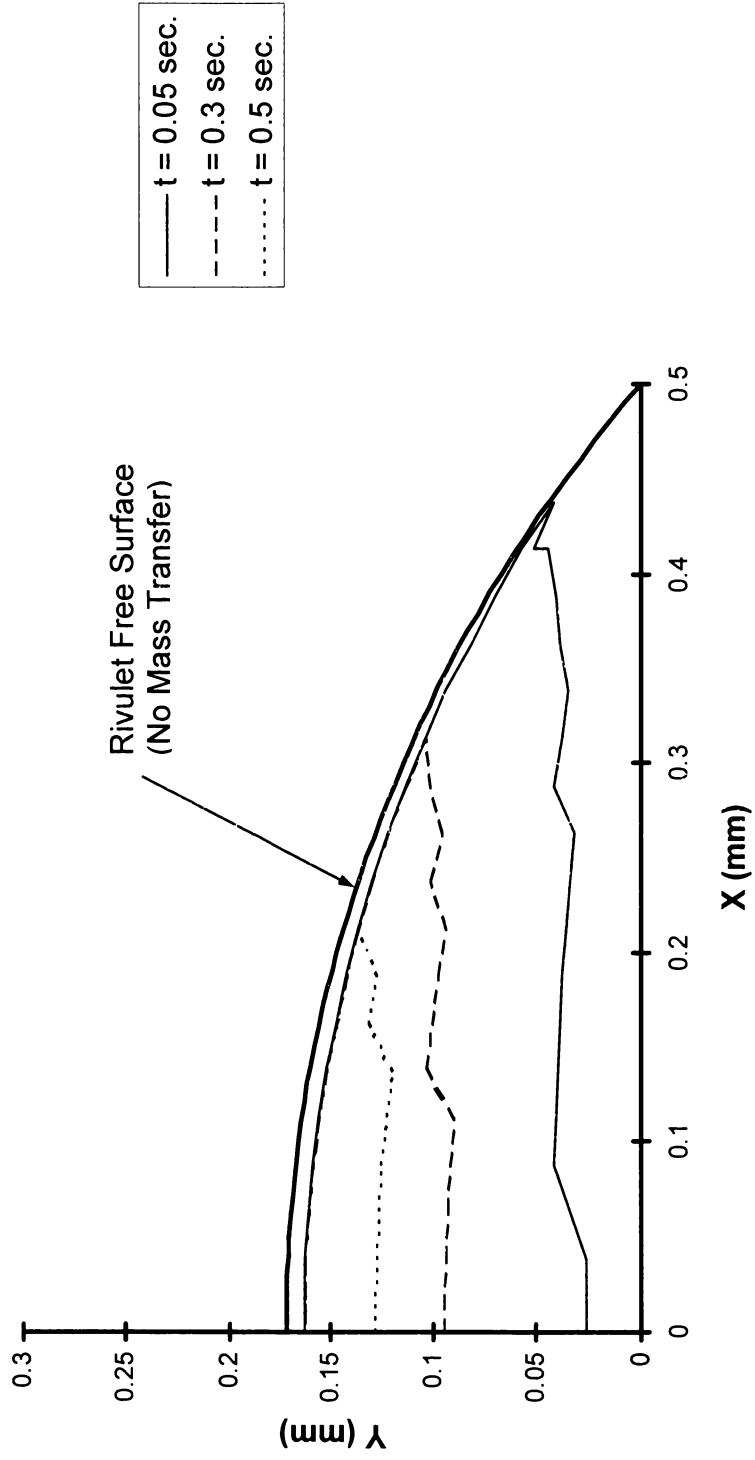


**Figure 30.** Case 3-C\_b: Case 3-C Rivulet With No Mass Transfer (Evaporation/Sublimation) At The Free Surface

- $t_f$ : The time for a complete freeze of the rivulet (seconds). A computational time step,  $\Delta t$ , ranging from 0.0001 seconds to 0.0002 seconds was used.
- $\beta$ : The rivulet/substrate contact angle (degrees).
- $St_e$ : The associated Stefan number (non-dimensional).
- $T_{in}$ : The uniform initial temperature of the rivulet (Kelvins).
- $T_{inf}$ : The freestream air temperature (Kelvins).
- $T_w$ : The constant wall or substrate temperature (Kelvins).
- $rh$ : The relative humidity of the gas medium (non-dimensional).
- $w_r$ : The rivulet full width (mm).
- $U_{inf}$ : The freestream velocity of the gaseous medium (m/s)

The stationary rivulet widths in Table 2 were obtained from the experimental simulation video footage by employing a scaling methodology. The phase-change front propagation results shown in Figures 24-30 are physically reasonable and show some interesting trends. There exists some jaggedness to the phase front line due to the volume tracking effect spoken of previously. The propagation line is obtained by connecting the nodes of each slushy cell to the next. Thus, the phase front is captured within a cell width. One should note that the contact angle for Cases 7-C and 9-C is  $60^\circ$ , and their measured widths are 1.5 mm and 2.0 mm, respectively. This results in an increased rivulet height,  $\delta$ , for these two cases. Cases 3-C, 7-C and 9-C reveal the effect of a cooler wall temperature relative to the phase change temperature,  $T_{mp} = 273.15$  K. In cases 3-C, 7-C and 9-C, the phase-change propagation is dominated by travel from the cold wall

inward and upward toward the free surface. However, the front propagation from the free surface advanced only slightly. Case 1-C shows considerable front propagation from the free surface inward due to a wall temperature closer to the phase change temperature. Case 4-C reveals some front propagation from the free surface; however, propagation from the wall still dominates due to a colder wall and an initial rivulet temperature slightly above the freezing temperature.

Finally, cases 3-C\_a and 3-C\_b reveal the resultant effect of thermal energy removal at either the rivulet free surface only or the wall only, when compared with their parent rivulet, namely 3-C. Case 3-C\_a shows the effect of an adiabatic wall boundary condition, wherein only one phase-change front exists and propagates inward from the free surface towards the wall. Case 3-C\_b shows the effect of eliminating mass transfer by evaporation, and its associated thermal energy. The result is a phase-change front propagation profile very similar to that shown in Figure 13 for case 3-C. These two cases serve to demonstrate that thermal energy removal at the wall boundary by conduction dominates the rivulet freezing process.

### **Surface Heat Transfer Rate Results**

Of interest in the stationary freezing rivulet problem are the rates of thermal energy removal via convective transfer at the rivulet/air interface (free surface) and via conduction at the wall boundary. Therefore, the heat transfer rates at these boundaries are plotted in Figures 31-40. The values were obtained by evaluating the line integrals along the respective surfaces given by

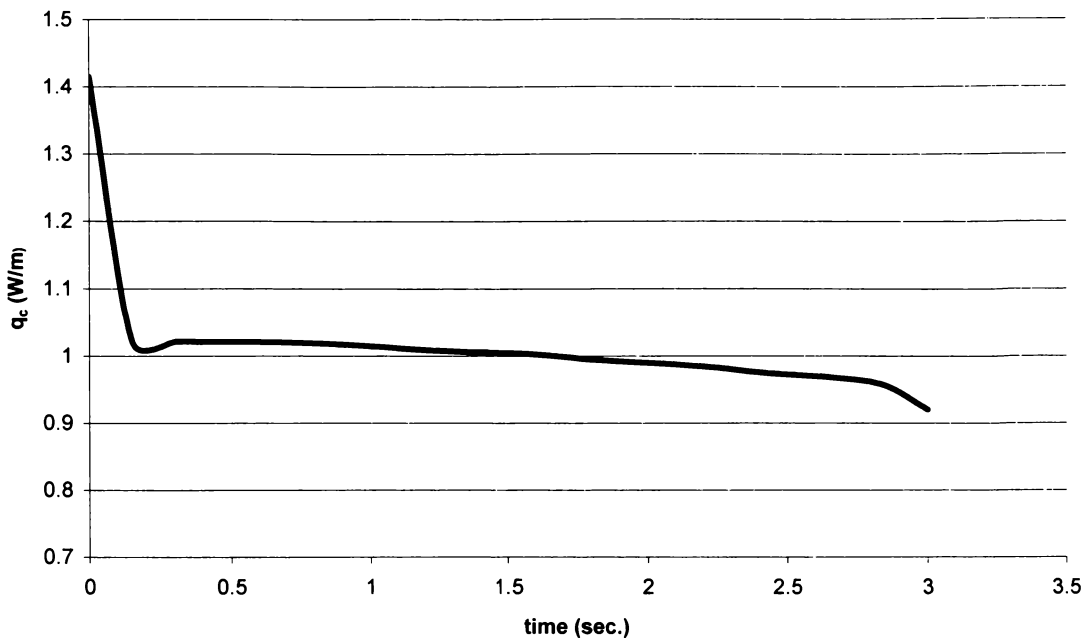


**Figure 31.** Case 1-C Free Surface Heat Flux

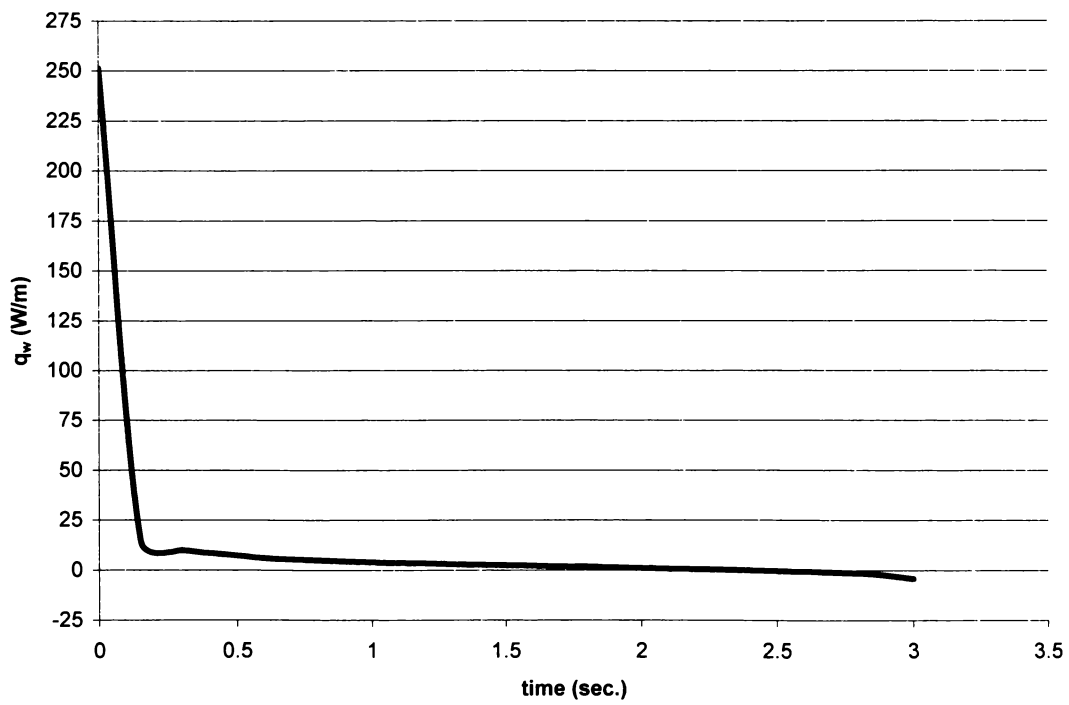


**Figure 32.** Case 1-C Wall Heat Flux

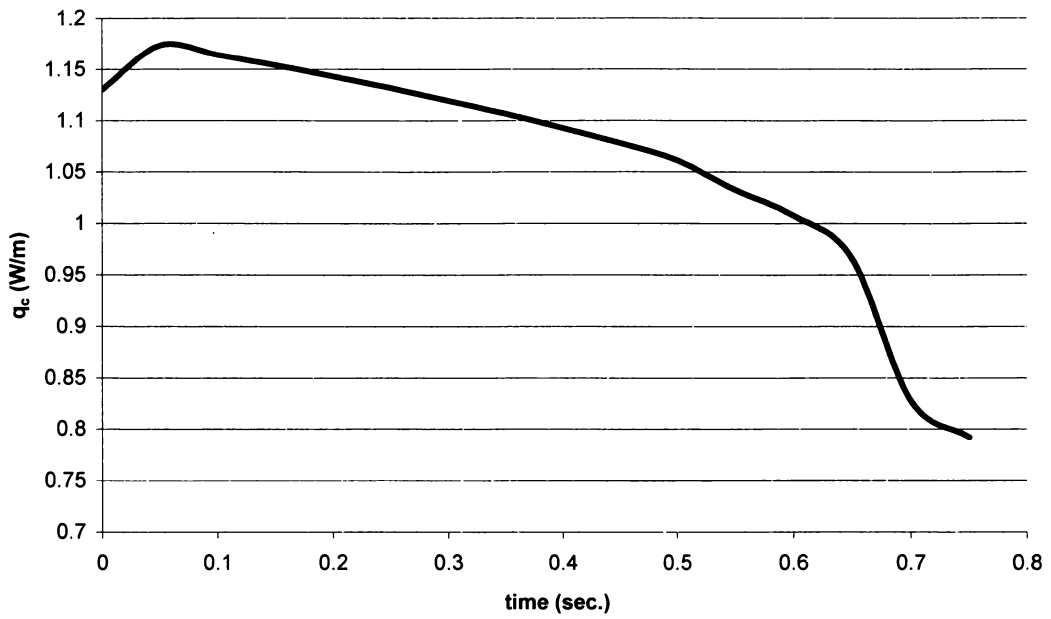


**Figure 33.** Case 3-C Free Surface Heat Flux

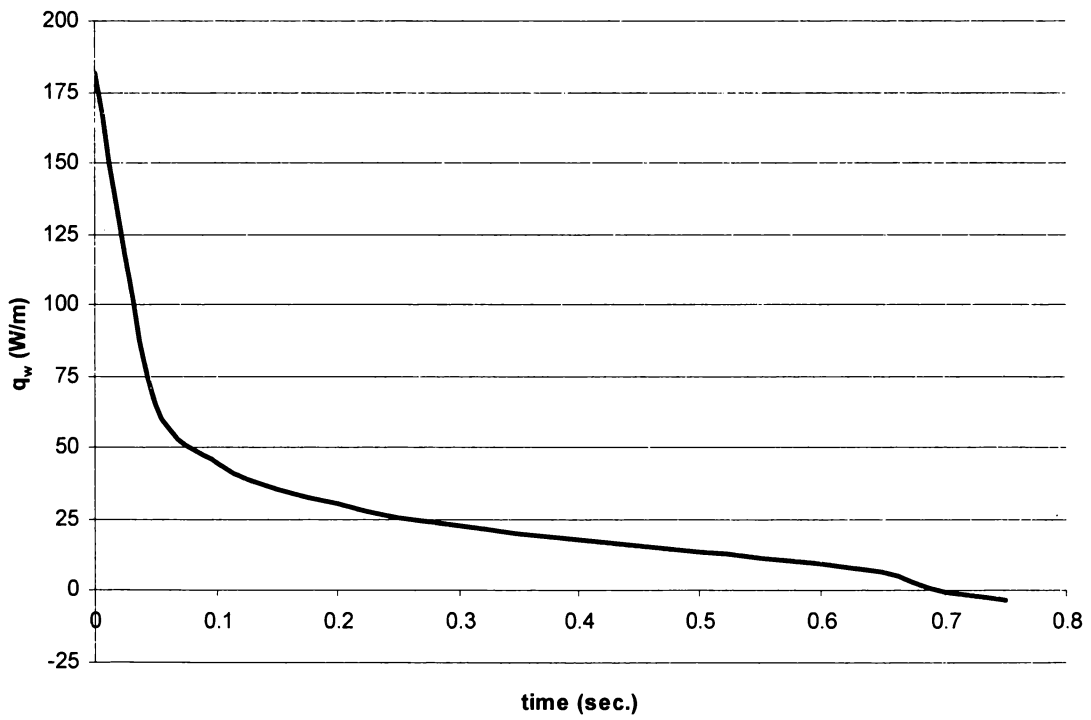


**Figure 34.** Case 3-C Wall Heat Flux

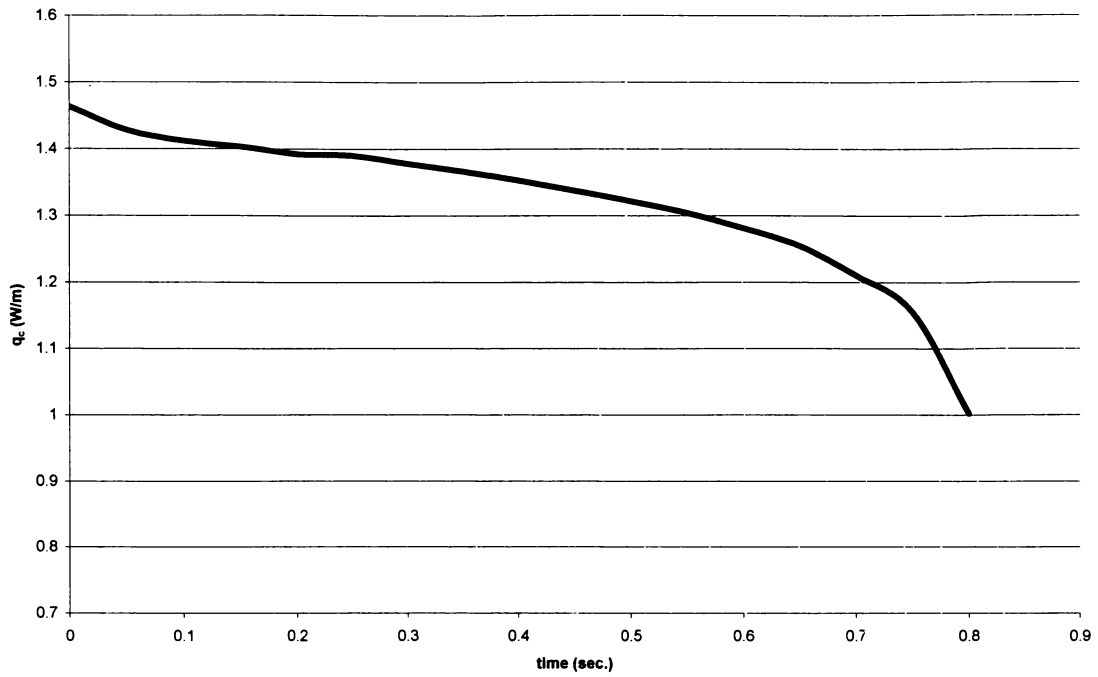


**Figure 35.** Case 4-C Free Surface Heat Flux

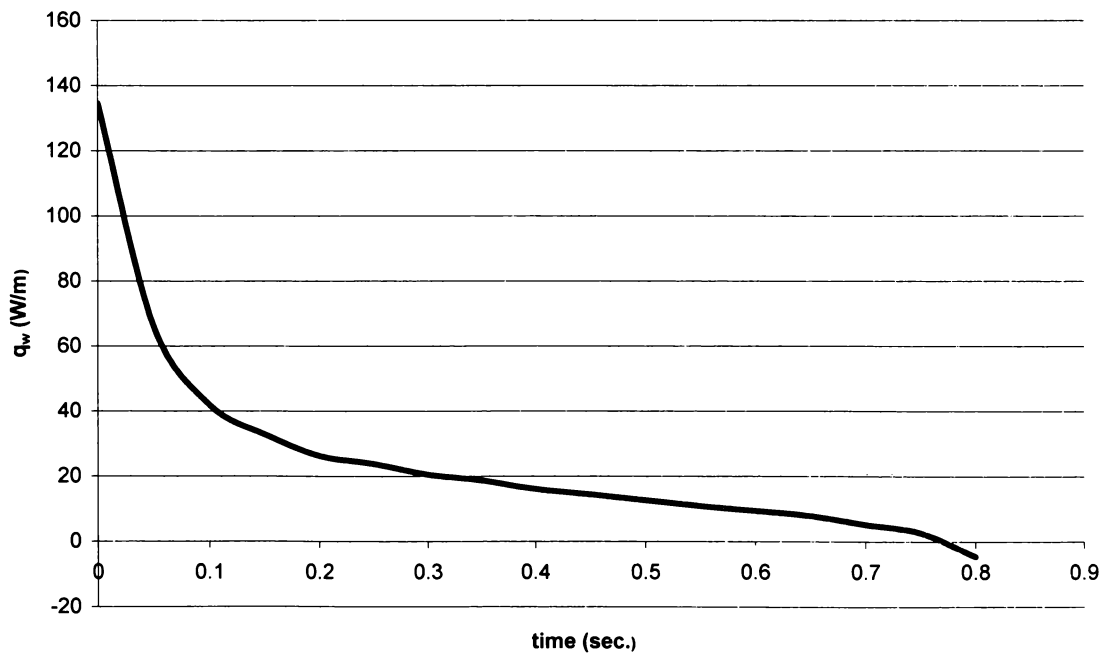


**Figure 36.** Case 4-C Wall Heat Flux

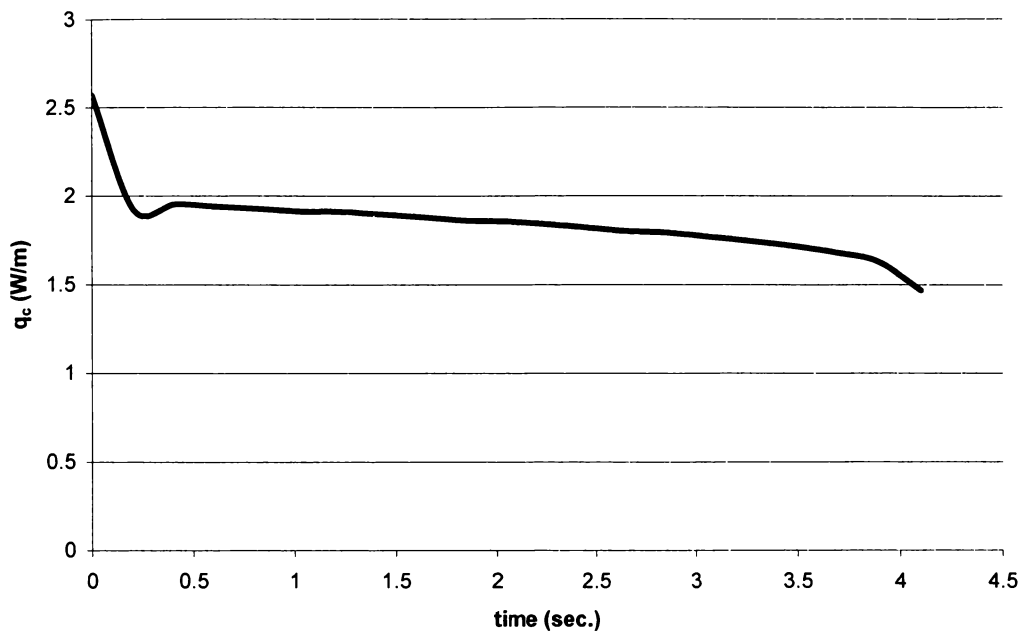


**Figure 37.** Case 7-C Free Surface Heat Flux

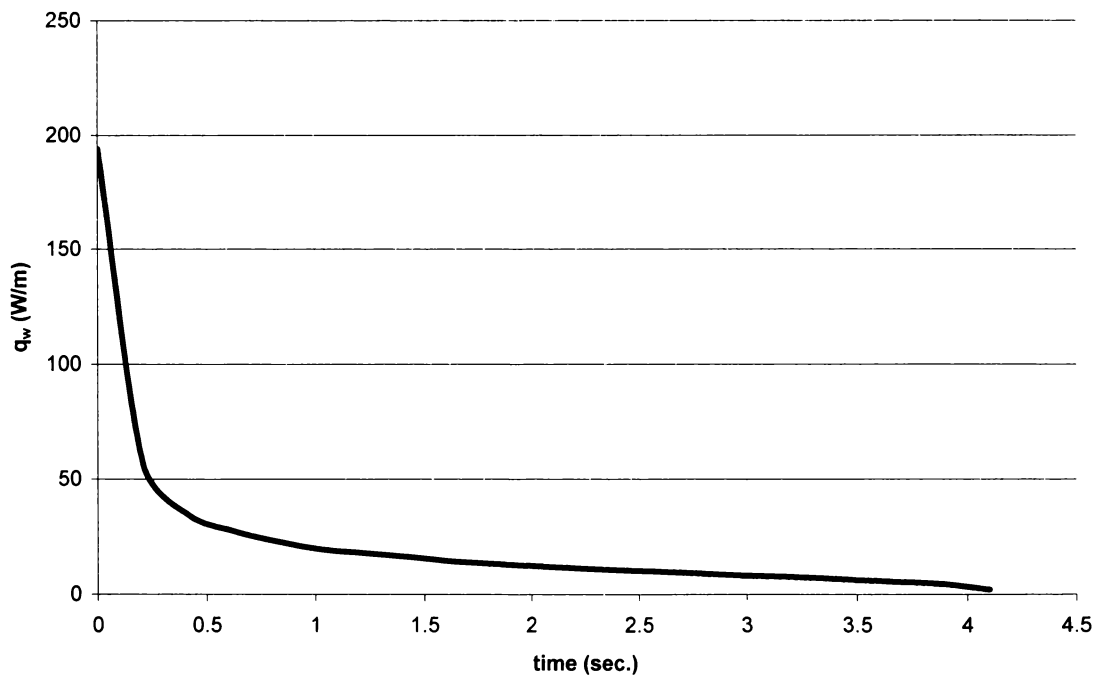


**Figure 38.** Case 7-C Wall Heat Flux



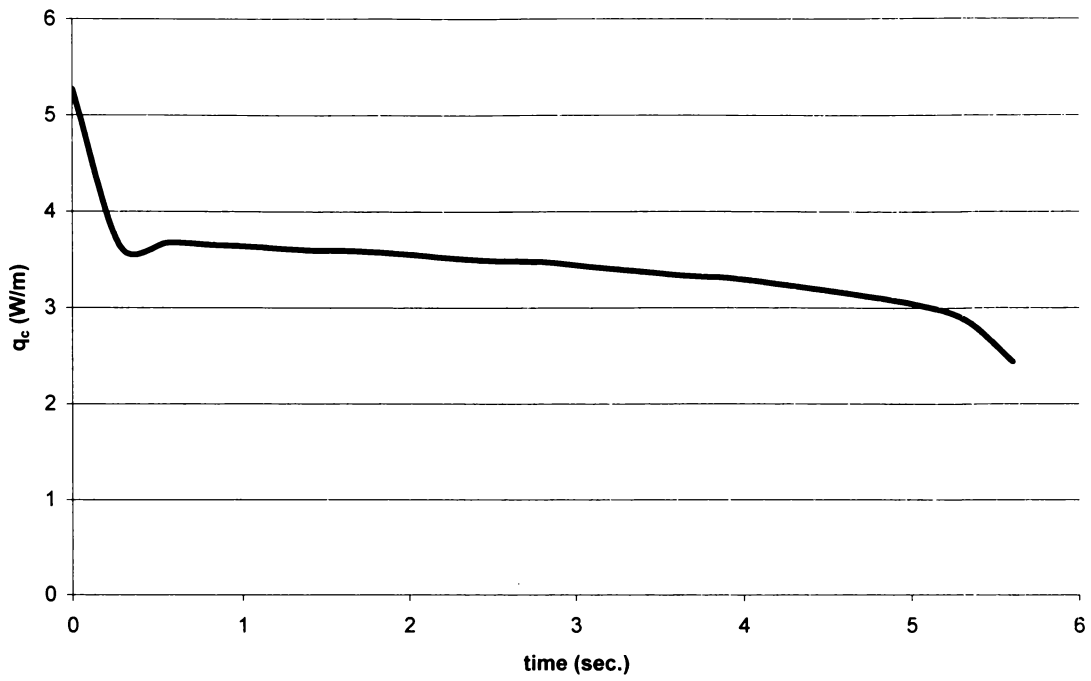


**Figure 39.** Case 9-C Free Surface Heat Flux

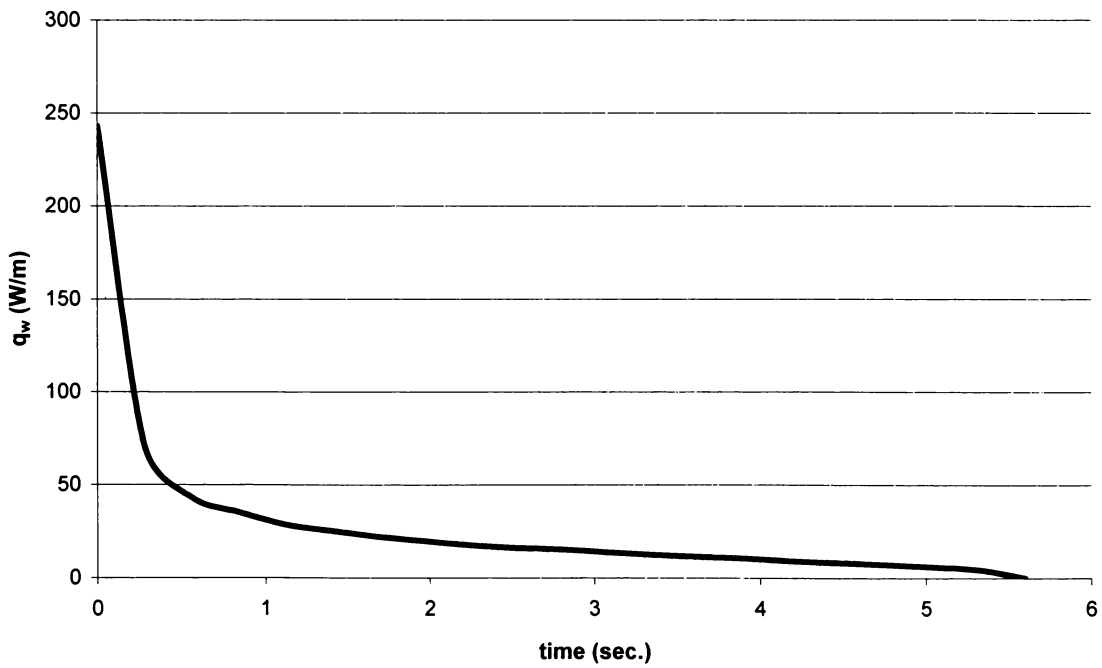


**Figure 40.** Case 9-C Wall Heat Flux

$$\dot{q}' (W / m) = h_c \int_{\theta_a}^{\theta_b} (T_{fs} - T_{rec}) R d\theta, \quad \text{Free Surface Heat Flux}$$

and

$$\dot{q}'_w (W / m) = \int_0^{R \sin(\beta)} \frac{(T_{i,1} - T_w)}{\hat{R}_{i,j}^{n+1}} dx \quad \text{Wall Heat Flux}$$

(4.37)

In equation (4.37),  $T_{fs}$  is the temperature at the free surface, and  $T_{i,1}$  is the temperature one node off the wall in the “y” direction. The Simpson rule was employed for the numerical integration. Note, that because the rivulet properties are uniform in the axial (z) direction, the heat transfer results are in terms of the rate of heat transfer per unit axial length (W/m).

The slight up-turn in the heat transfer rate at the free surface in Figures 31, 33, 37 and 39 and at the wall boundary in Figure 32, at  $t \approx 0.25$  seconds, is likely the artifact of numerical overshoot. However, a contributor to the more pronounced up-turn at the rivulet free surface could be the result of the boundary cell becoming totally frozen and contributing to the thermal energy transfer via sublimation rather than evaporation. Immediately following this slight up-turn, the heat transfer rate plateaus briefly while the latent heat of fusion is removed from the boundary cell followed by sensible heat removal and an associated temperature drop. This phenomenon is evident in each case except 4-C (Figure 35), wherein the temperature of the rivulet is initially at the phase-change temperature.

An additional, and interesting, heat transfer rate comparison is obtained through comparing the free surface heat transfer to the wall heat transfer after each has been

normalized using the their respective transfer rates at time  $t=0.0$ . These comparisons are found in Figures 41-45. The rate of heat conduction at the wall is shown to drop rapidly due to the temperature of the node just inward from the wall boundary quickly approaching the wall temperature. Thus, this effect is an artifice of the sudden application of the constant cold wall temperature, and then normalizing the heat transfer rates that follow by the initial heat transfer rate.

### **Remarks**

The results presented above for the **stationary** freezing rivulet simulation speak clearly of the utility of the enthalpy method formulation for the subject Stefan problem. Based upon this strong evidence and the effectiveness of the associated Gauss-Seidel numerical solution technique, the enthalpy method was applied to the freezing rivulet **runback** problem. The details of the freezing rivulet runback simulation are discussed in Chapter V.

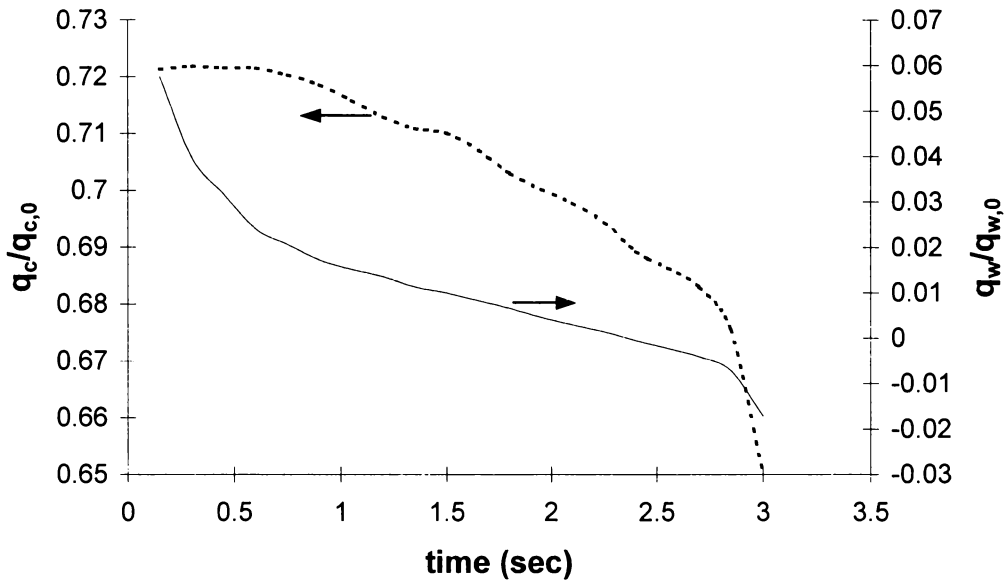


**Figure 41.** Case 1-C Normalized Heat Flux Comparison

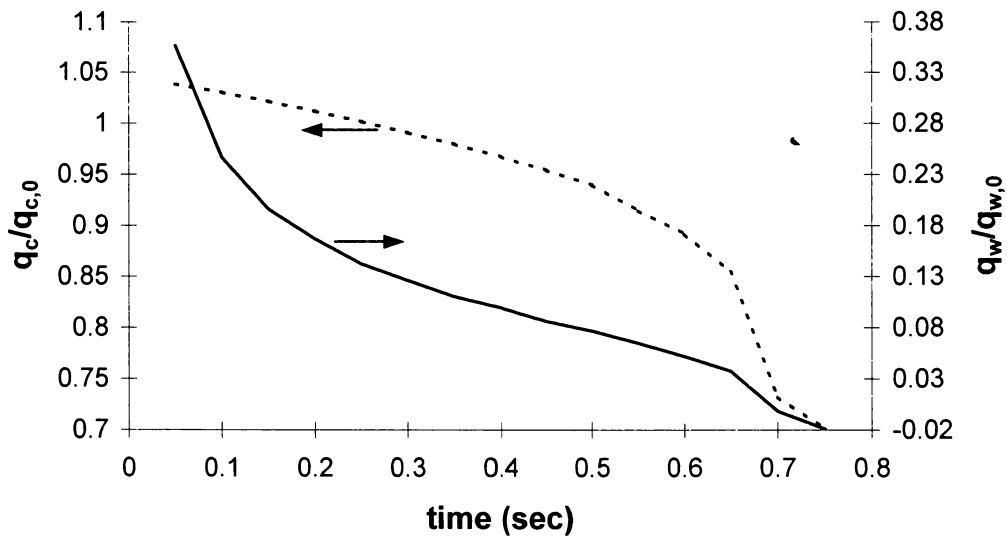


**Figure 42.** Case 3-C Normalized Heat Flux Comparison

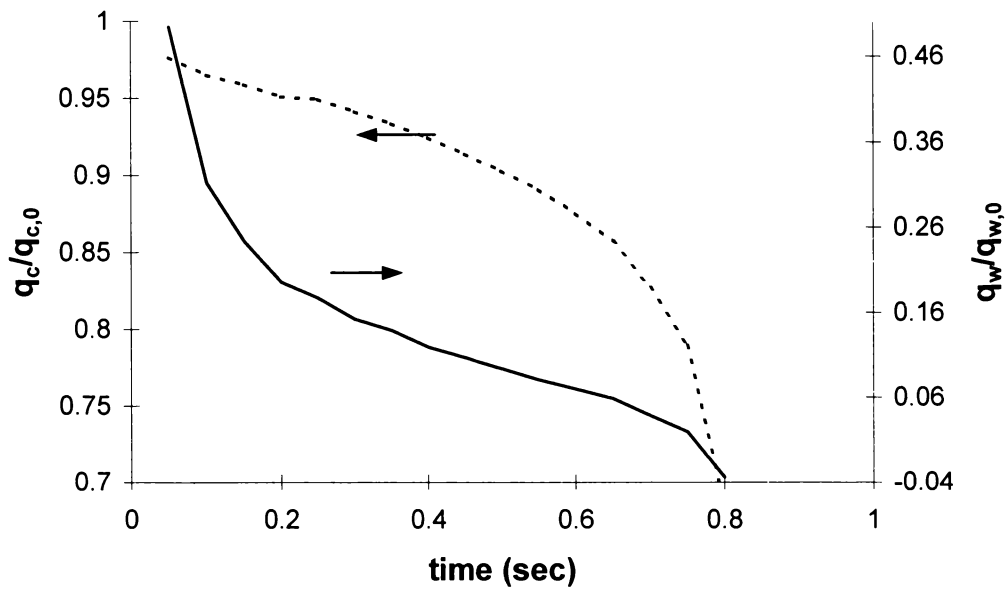


**Figure 43.** Case 4-C Normalized Heat Flux Comparison

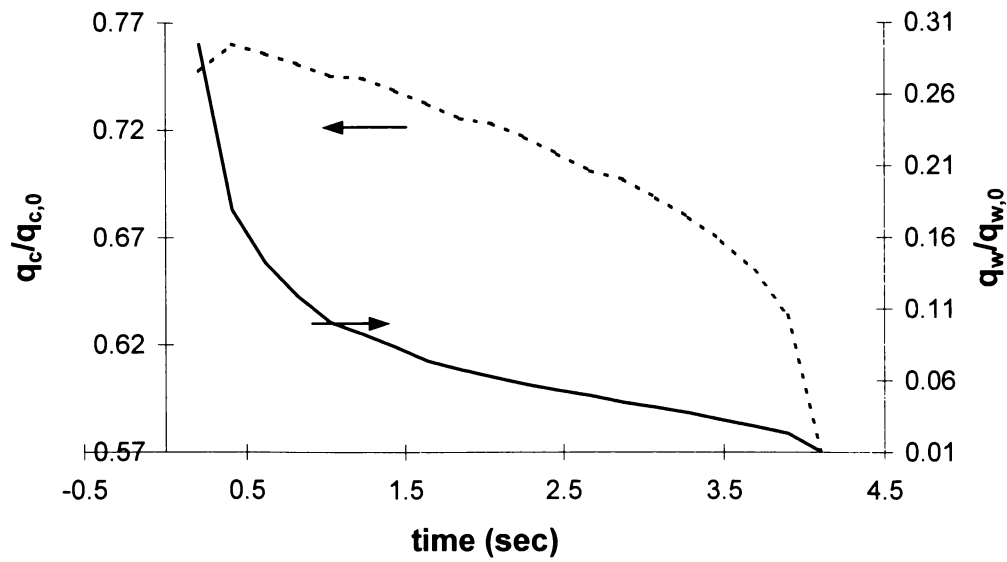


**Figure 44.** Case 7-C Normalized Heat Flux Comparison

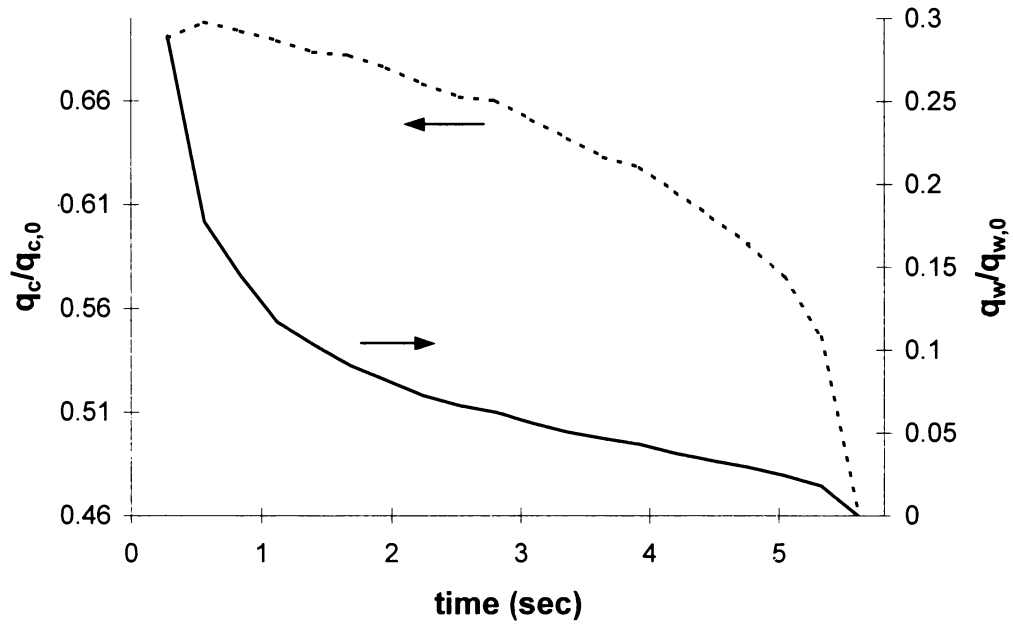


**Figure 45.** Case 9-C Normalized Heat Flux Comparison

## CHAPTER V

### FREEZING RIVULET RUNBACK NUMERICAL SIMULATION

The stationary rivulet model detailed in Chapter IV provides the physical and numerical foundation upon which the more complicated **runback** simulation is built. The desired result of the subject simulation of freezing shear driven rivulets is the prediction of the extent of rivulet travel and associated freezing profile during the process. The details of the freezing runback model are discussed below, including appropriate simplifying assumptions. A copy of the computer code containing the numerical simulation of the freezing of shear driven rivulet runback can be obtained from the author upon request.

#### Freezing Rivulet Runback Modes

The freezing rivulet runback model is comprised of three distinct modes. In the aggregate, these modes constitute the runback model, but are distinct in the physical phenomena that each attempts to capture. The basis for such a demarcation by modes comes from the physical observation of freezing shear driven rivulet runback on a NACA0012 airfoil [26]. These data obtained from freezing rivulet runback on the NACA0012 airfoil served as a baseline for the runback model development. The freezing of shear driven rivulets is a complicated interaction between the driving flowfield, fluid and solid interfacial phenomena and the microphysical dynamics of phase-change. The formulation of the problem into distinct modes allows the observed

physical phenomena to be simulated in a simplified manner. The established runback modes are discussed below.

**Mode #1 – Freezing Rivulet Runback without Frozen Deposition**

The initial stage of the freezing runback process is characterized by a fully developed shear driven rivulet that suddenly comes in contact with a cold surface, where  $T_s < T_{mp}$ . A portion of the rivulet freezes as it runs back, however this frozen fraction does not adhere to the surface but is carried along downstream with the traveling rivulet. Thus, the rivulet does not lose mass due to solid deposition during runback, but remains intact until an empirically specified halt distance is reached. The Mode #1 condition is illustrated in Figure 46(a) below. The distance the rivulet front travels before coming to a halt is established by an empirical non-dimensional parameter,  $Wi$ , which characterizes the rivulet front (leading edge) at halt. This parameter is defined by

$$Wi = \frac{\tau_i \bar{m}_f}{F_r}, \tag{5.1}$$

where  $\tau_i$  is the shear stress at the free surface,  $\bar{m}_f$  is the average rivulet liquid mass fraction and  $F_r$  is the ice/substrate interface sliding friction force per area of interface. Employing the observed bulk rivulet halt length from [26] as the solution constraint, the runback model presented herein was used to evaluate the resultant conditions of the rivulet front at halt. Based upon this result, the traveling rivulet front is said to halt when  $Wi \geq 2.25$ . This empiricism consists of a weighted ratio between the free surface driving shear force and the resistive sliding friction force at the solid wall. The weighting factor, as depicted above, is the liquid mass fraction at the rivulet front.



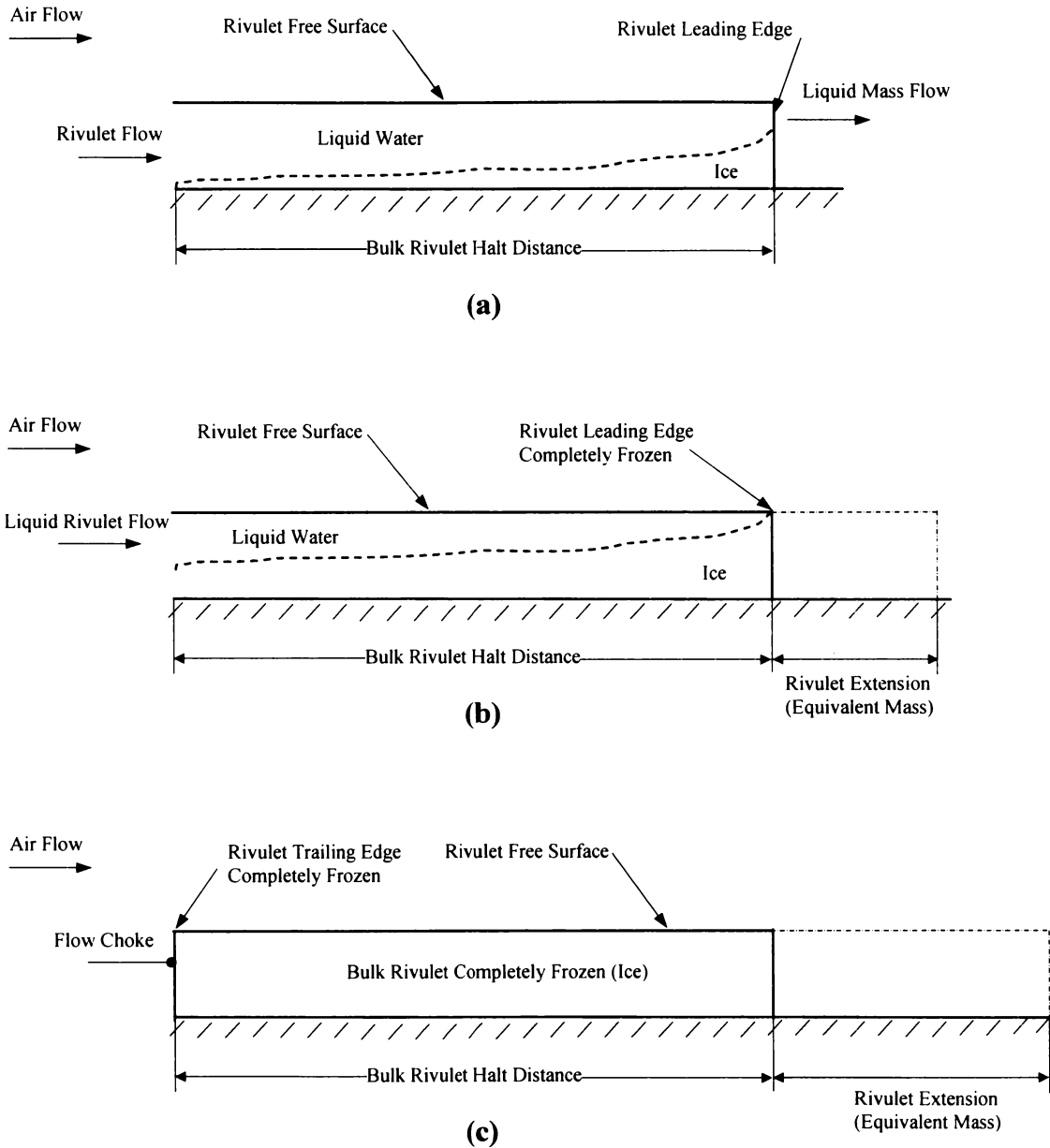


**Figure 46.** Rivulet Freezing Modes: (a) Mode #1, (b) Mode #2 and (c) Mode #3

The liquid rivulet is driven downstream by the shear loading at the free surface generated in the high-speed gas flow environment. Accordingly, a velocity field is developed within the rivulet, resulting in an associated shear stress manifest at the rivulet/wall interface. However, as the rivulet begins to freeze at the wall boundary, a portion of the liquid/solid interfacial shear now acts upon the resultant ice layer at the phase-change interface. The resistance to motion beneath the ice layer is now one of sliding friction between the ice and wall. Soon after freezing is initiated at the wall boundary, an ice layer is formed between the wall and the remaining liquid portion of the rivulet. The author proposes that at the phase-change interface the liquid shear force is sufficient to overcome the opposing sliding friction force at the ice/wall interface until the halt criterion,  $Wi \geq 2.25$  is met.

The friction force at the wall boundary essentially remains constant, while the phase-change interface shear force decreases due to a reduction in interface area as the rivulet freezes. The said reduction in phase-change interface area, as the rivulet freezes from the wall outward, is a natural by-product of the circular rivulet shape. As the rivulet runs back, the bulk structure remains intact, albeit partially frozen, until the halt distance is reached and the frozen portion stays fixed spatially. The varying liquid mass fraction in equation (5.1) represents the effect of the varying interfacial area. The temperature of the wall remains constant as in the **stationary** rivulet model discussed in Chapter IV, however, the thermal resistance at the wall boundary employs a convective heat transfer coefficient based on laminar flat plate theory. Summarily, the halt distance refers to that distance traveled by the freezing rivulet before the frozen portion halts and the remaining

liquid continues on downstream. The freezing rivulet between the upstream (trailing edge) starting point and the downstream (leading edge) halt point is hereafter referred to as the “bulk rivulet”. The downstream travel of the remaining liquid after halt is the substance of Mode #2.

## **Mode #2 – Extension of Liquid Mass Beyond Halted Frozen Mass until Rivulet**

### **Leading Edge Completely Freezes**

Once the frozen portion of the rivulet has come to a halt, Mode #2 attempts to capture the extension of the rivulet as liquid mass is ejected downstream beyond the halted frozen portion of the rivulet. Liquid is ejected until the rivulet front, or leading edge, at the halt distance has completely frozen,  $\bar{m}_f = 0$ . The quantity of liquid mass that flows downstream of the halt distance is based upon a mass balance. The density of the liquid, average liquid rivulet velocity and the liquid cross-sectional area at the halt distance combine to establish the rate of liquid mass ejection downstream. Once the cross-sectional area is reduced to zero due to a completely frozen front, the ejection of liquid mass downstream in this mode stops. The condition at the conclusion of Mode #2 is illustrated in Figure 46(b). The complexities and uncertainties associated with the interaction of the ejected liquid mass with the surrounding flowfield make the application of simplifying assumptions prudent. Therefore, the magnitude of the rivulet extension downstream is quantified by assuming the total ejected mass maintains a continuum and has the same cross-sectional area as the original rivulet. Knowing the density of the liquid, the mass ejected and the proposed cross-sectional area, the axial length of the extended rivulet is easily determined. Clearly, these assumptions do not account for the

dynamics of the freezing liquid and its associated travel as in Mode #1. Thus, the model simply attempts to capture the amount of liquid mass that flows beyond the halted frozen mass of the bulk rivulet and then subsequently freezes. The spatial parameter attached to this downstream flow is a rivulet extension length of equivalent mass.

An additional complexity inherent to Mode #2 is formulating an appropriate convective heat transfer coefficient at the phase-change interface of the bulk rivulet, wherein now there exists a convective boundary. The complexity is manifest by the fact that the boundary is moving and has an associated impact on the boundary layer at the interface. The thermal resistance of a “slushy” cell, wherein this phenomenon is addressed, is discussed hereafter. The thermal resistance at the wall, however, now consists of a simple conduction boundary since the bulk rivulet is halted.

**Mode #3: Liquid Mass Extension Beyond Halted Frozen Mass until Choke Condition is Achieved**

Since at the conclusion of Mode #2 the bulk rivulet trailing edge (upstream starting point) is still not completely frozen, there continues to be further liquid flow downstream. Mode #3 is very similar to Mode #2 from a modeling standpoint, however the computations now take place at the rivulet inlet plane, or trailing edge, rather than at the rivulet halt plane, or leading edge. However, the author chose to distinguish this mode because it represents the liquid runback during the time between when the leading edge completely freezes and when the trailing edge completely freezes and chokes off further flow. The condition at the conclusion of Mode #3 is illustrated in Figure 46(c). A main distinction associated with Mode #3 is that the runback is likely in the form of

liquid beads that “ride” atop the frozen downstream portion of the rivulet and subsequently flow off the end of the rivulet. This phenomenon is clearly shown in Figure 3 of Chapter I for the B1-B engine inlet, wherein beaded deposits are shown on the surface downstream of the continuous, or bulk rivulet. In Mode #3, again a mass balance is employed to determine the quantity of mass that runs back. A reasonable constraint levied in this mode is that the cross-sectional area of the bulk rivulet does not grow. Therefore, all the liquid mass that runs back during Mode #3 is deposited downstream of the bulk rivulet front face. Also, this implies that the amount of liquid mass entering the bulk rivulet at the upstream face is the same amount that must be ejected downstream to satisfy continuity. During this process the bulk rivulet continues to completely freeze; complete freeze being the result manifest by a liquid mass fraction equal to zero at the upstream face. At this point, the Mode #3 runback condition is deemed choked and no additional liquid runback along the established rivulet path is considered. The additional rivulet extension length resulting from the Mode #3 process is determined in the same way as for Mode #2. In reality, the Mode #3 rivulet extension would most likely be in the form of frozen beads separated by dry patches. However, herein the rivulet is extended in a continuum consisting of the amount of mass equivalent to that which runs back beyond the rivulet halt distance.

A worthy note is that as the upstream face freezes, the mass flow rate of liquid entering the domain of the bulk rivulet is reduced according to the available liquid cross-sectional area. Thus, any liquid running back that impinges on the solid part of the upstream face of the bulk rivulet is diverted and follows a path separate from that

provided by the bulk rivulet. The freezing run back simulation, therefore, models the freezing of only that flow associated with the bulk rivulet path.

The final rivulet extension length is determined from the sum of the Mode #2 and Mode #3 length extensions. The extension length forms a rivulet continuum with the same cross-sectional area as the original bulk rivulet. The simulation of the behavior of the bulk rivulet is the focus of the runback rivulet model. The behavior of the bulk rivulet during the freezing runback process determines the bulk rivulet halt length and the subsequent downstream extension.

Finally, a clarification of terms associated with Mode #3 is in order. In Mode #3, when the trailing edge (upstream station where the rivulet begins to freeze) is completely frozen the rivulet flow is considered “flow” choked and no further flow is found within the bulk rivulet domain, as shown in Figure 46(c). Additional upstream flow could potentially use the frozen rivulet as a path to a downstream destination; however, this type of “piggy back” flow is not simulated herein. Another type of choking mechanism is associated with the freezing itself. Cases are shown hereafter where, under certain conditions, the rivulet trailing edge cross-section does not completely freeze, but an equilibrium condition is attained in the energy balance at the phase-change interface. That is, a point is reached where the rate at which energy is convected into the control volume, via the liquid flow, equals the rate at which latent heat is removed from the liquid. Thus, the freezing process is defined as choked under the circumstances described. Therefore a “freeze” choke exists at the upstream station. Under such a

condition, the rivulet will continue to extend downstream until the upstream water supply is depleted.

### **Governing Equations**

A formulation of the thermal energy transport equation that includes the spatial rate of enthalpy change coupled with the convective velocity of the rivulet flow is appropriate for freezing rivulet runback. That is, as the bulk rivulet runs back the heat transfer is steady state as the system enthalpy changes with respect to the streamline spatial coordinate. Equation (4.1) now becomes

$$w \frac{\partial h}{\partial z} = \frac{k}{\rho} \left[ \frac{\partial^2 T}{\partial x^2} + \frac{\partial^2 T}{\partial y^2} \right], \quad (5.2)$$

where,  $w$  is the velocity in the z-direction, or streamline direction of the rivulet flow. As expressed previously, the Peclet number is large enough to suggest that heat conduction in the streamwise direction is negligible. From an Eulerian viewpoint, equation (5.2) represents a steady state formulation. For Mode #1, however, one desires to monitor the thermal energy transport of the rivulet front (leading edge) while traveling downstream. Thus, when one hops on board and rides the rivulet front, the problem becomes Lagrangian in nature and equation (5.2) still holds. As the rivulet runs back, the enthalpy of the computational cells that make up the rivulet front are updated at each spatial step,  $\Delta z$ . This local spatial step is defined by  $\Delta z = w_{i,j} \Delta t$ , where  $w_{i,j}$  is the local cell velocity and  $\Delta t$  is the constant user defined time step.

The governing equation (5.2) is also applied to the constant volume liquid cells of Modes #2 and #3 following the halt of the frozen portion of the bulk rivulet. All computational cells within the rivulet model maintain a constant volume and mass, except for the free surface boundary cells where mass is ejected via evaporation or sublimation. An energy balance on the liquid cells of Modes #2 and #3 results in equation (5.2), where  $\Delta z$  is now the fixed computational cell length in the streamwise direction (Eulerian) rather than the incremental distance traveled (Lagrangian) in Mode #1 as the rivulet front is tracked. The halted bulk rivulet volume, and accordingly the mass, is fixed, except for volume reduction due to mass loss at the free surface. Thus, the same amount of liquid entering the halted rivulet domain upstream must be ejected downstream. As the rivulet continues to freeze during Modes #2 and #3, the bulk rivulet frozen fraction continues to increase until flow into the rivulet domain is choked. The enthalpy of each liquid cell after rivulet halt is updated with the new enthalpy value at the local time,  $t^n + \frac{\Delta z}{w_{i,j}}$ , which corresponds to the enthalpy value at the downstream face of the cell. Equation (4.1) is employed in cells that are solid or contain the phase-change interface. The thermal resistance of the phase-change (or slushy) cells is a modified formulation of those applied to the stationary rivulet since there is now an internal convective boundary at the liquid/solid interface. The thermal resistance of the cells containing the phase-change front is treated in detail hereafter.



Before the discretization of the above governing equation and associated boundary equations is presented, the spatial coordinate,  $z$ , and the local cell velocity,  $w$ , are non-dimensionalized according to

$$\bar{z} = \frac{z}{\delta} \quad \text{and} \quad \bar{w} = \frac{w}{\bar{W}_r} \quad (5.3)$$

respectively, where  $\bar{W}_r$  is the average streamwise velocity over the rivulet cross-section. The derivation for both the local cell velocities and the associated average rivulet velocity is shown hereafter. Also, equation (5.2) is brought into the computational domain via a transformation similar to equation (4.17). In the computational domain, equation (5.2) becomes

$$\frac{\partial \psi}{\partial \bar{z}} = \frac{k}{w_{i,j}} C_w \delta \left\{ \frac{\partial^2 \phi}{\partial X^2} + \frac{1}{\Gamma^2} \left( 1 + \left( \frac{d\xi}{dx} \right)^2 \eta^2 \right) \frac{\partial^2 \phi}{\partial \eta^2} + \frac{1}{\Gamma^2} \left( \frac{d\xi}{dx} \right)^2 \eta \frac{\partial \phi}{\partial \eta} \right\}, \quad (5.4)$$

where  $w_{i,j}$  is the local cell velocity in the rivulet streamwise direction. Equation (5.4) differs from equation (4.17) only in the leading coefficient on the right hand side, which now contains the local streamwise velocity and the rivulet height,  $\delta$ .

### **Discretization of Governing Equations**

Similarly to equation (4.24), the discretized form of equation (5.4), for  $2 \leq i \leq M$  and  $2 \leq j \leq N$ , is

$$\begin{aligned}
\psi_{i,j}^{n+1} + \frac{\Delta \bar{z} C_w}{w_{i,j}^n \delta^n} & \left\{ \frac{2.}{\Delta X \bar{R}_{i,j}^{n+1}} + \frac{2. \left( 1. + \left( \frac{d\xi}{dx} \right)^2 \eta^2 \right)}{\Delta \eta \Gamma^2 \hat{R}_{i,j}^{n+1}} \right\} \phi_{i,j}^{n+1} = \psi_{i,j}^n + \\
& \left. \frac{\Delta \bar{z} C_w}{w_{i,j}^n \delta^n} \left\{ \frac{1.}{\Delta X} \left[ \frac{\phi_{i-1,j}^{n+1}}{\bar{R}_{i-1,j}^{n+1}} + \frac{\phi_{i+1,j}^{n+1}}{\bar{R}_{i+1,j}^{n+1}} \right] + \frac{\left( \frac{d\xi}{dx} \right)^2 \eta}{2. \Gamma^2} \left[ \frac{\phi_{i,j+1}^{n+1}}{\hat{R}_{i,j+1}^{n+1}} - \frac{\phi_{i,j-1}^{n+1}}{\hat{R}_{i,j-1}^{n+1}} \right] + \right. \right. \\
& \left. \left. \frac{\left( 1. + \left( \frac{d\xi}{dx} \right)^2 \eta^2 \right)}{\Delta \eta \Gamma^2} \left[ \frac{\phi_{i,j-1}^{n+1}}{\hat{R}_{i,j-1}^{n+1}} + \frac{\phi_{i,j+1}^{n+1}}{\hat{R}_{i,j+1}^{n+1}} \right] \right\} \right. \quad (5.5)
\end{aligned}$$

Equation (5.5) applies to each cell within the rivulet computational domain except for the symmetry boundary cells and the rivulet/wall interface boundary cells. The discretized symmetry boundary equation is the same as in equation (4.29) for the stationary freezing rivulet. That is

$$\phi_{0,j}^{n+1} = \phi_{1,j}^{n+1} . \quad (5.6)$$

Now, however, the rivulet/wall interface boundary cell contains a convective thermal resistance rather than a conduction resistance, and upon discretization, the governing equation for the boundary cells at  $j=1$  and  $2 \leq i \leq M$  becomes

$$\begin{aligned}
& \psi_{i,j}^{n+1} + \Delta t C_w \left\{ \frac{2.}{\delta^2 \Delta X \bar{R}_{i,j}^{n+1}} + \left( \frac{d\xi}{dx} \right)^2 \left[ \frac{1.}{\hat{R}_{i,j+1}^{n+1}} \left( \frac{-\eta}{2. \Delta \eta} + \eta \right) \right] + \frac{1.}{\Delta \eta \xi^2(x) \hat{R}_{i,j+1}^{n+1}} \right\} \phi_{i,j}^{n+1} \\
& = \psi_{i,j}^n + \Delta t C_w \left\{ \frac{1.}{\delta^2 \Delta X} \left[ \frac{\phi_{i-1,j}^{n+1}}{\bar{R}_{i-1,j}^{n+1}} + \frac{\phi_{i+1,j}^{n+1}}{\bar{R}_{i+1,j}^{n+1}} \right] + \left( \frac{d\xi}{dx} \right)^2 \left[ \frac{\eta^2}{2 \Delta \eta} \left( \frac{-2 \phi_{i,j+1}^{n+1}}{\hat{R}_{i,j+1}^{n+1}} + \frac{\phi_{i,j+2}^{n+1}}{\hat{R}_{i,j+2}^{n+1}} \right) + \frac{\eta \phi_{i,j+1}^{n+1}}{\bar{R}_{i,j+1}^{n+1}} \right] + \right. \\
& \quad \left. + \frac{1}{\Delta \eta \xi^2} \left[ \frac{\phi_{i,j+1}^{n+1}}{\hat{R}_{i,j+1}^{n+1}} \right] \right\} \quad (5.7) \\
& + \frac{\bar{h}_w \Delta t}{\xi(x) \rho h_{i,s}} (T_w - \bar{T}_r),
\end{aligned}$$

where  $\Delta t = \frac{\Delta z}{\bar{W}_r}$ ,  $\bar{h}_w$  is the average heat transfer coefficient at the wall boundary, and  $\bar{T}_r$  is the average temperature over the rivulet local cross-section. The average heat transfer coefficient at the wall,  $\bar{h}_w$ , is based on the average Nusselt number for rivulet flow over a wall held at a constant temperature. This Nusselt number is defined by Al-Khalil [16] as

$$\bar{N}u = 2.63 + 0.000143 \text{Re} \quad , \quad \text{where } \text{Re} = \frac{\rho \bar{W}_r \delta}{\mu} \quad (5.8)$$

For the corner cell adjacent to both the wall and the symmetry boundary, where  $i = 1$  and  $j = 1$ , the coupling in the  $\eta$  direction is negligible. That is, the coupling coefficient in

equation (5.7),  $\left( \frac{d\xi}{dx} \right)^2$ , is negligibly small. Therefore, the governing equation for this

cell, after removing the coupling terms and invoking symmetry, becomes the simplified expression;

$$\begin{aligned} \psi_{i,j}^{n+1} + \Delta t C_w \left\{ \frac{1}{\delta^2 \Delta X \bar{R}_{i,j}} + \frac{1}{\Delta \eta \xi^2(x) \hat{R}_{i,j+1}} \right\} \phi_{i,j}^{n+1} = \psi_{i,j}^n + \\ \Delta t C_w \left\{ \frac{\phi_{i+1,j}^{n+1}}{\bar{R}_{i+1,j} \delta^2 \Delta X} + \frac{\phi_{i,j+1}^{n+1}}{\hat{R}_{i,j+1} \Delta \eta \xi^2(x)} \right\} + \frac{\bar{h}_w \Delta t}{\Delta \eta \xi(x) \rho h_{i,s}} (T_w - \bar{T}_r). \end{aligned} \quad (5.9)$$

### **Rivulet Velocity Profile**

A closed form solution for the velocity profile of a traveling rivulet as a function of contact angle,  $\beta$ , was developed by Al-Khalil [16] employing a power series representation. The associated coefficients were determined using a least squares regression analysis on the data resulting from the analytical solution of the equation governing velocity. The relationship developed by Al-Khalil for the mass flow rate of a developed rivulet using this closed form velocity solution is

$$m_r = \frac{\rho \tau_i \dot{R}^3}{\mu} F_1(\beta), \quad (5.10)$$

where  $\tau_i$  and  $\mu$  are the rivulet free surface shear stress and dynamic viscosity of the liquid, respectively. The free surface driving shear stress is derived by employing flat plate correlations, thus

$$\tau_i = \frac{c_f}{2} \rho_a V_\infty^2, \quad (5.11)$$

where  $c_f = \frac{0.664}{\sqrt{\text{Re}}}$ , laminar flow,

or

$$c_f = \frac{0.455}{(\ln(0.06 \text{Re}))^2}, \text{ turbulent flow.}$$

Also,  $F_1(\beta)$  is a functional of the form

$$F_1(\beta) = b_1 f_{20}(\beta) + b_2 f_{22}(\beta) + \frac{2}{3} b_3 f_{30}(\beta) + \frac{2}{3} b_4 f_{32}(\beta), \quad (5.12)$$

where  $f_{20}(\beta)$ ,  $f_{22}(\beta)$ ,  $f_{30}(\beta)$  and  $f_{32}(\beta)$  are integral functions of the form

$$f_{ij} = \int_0^\beta (\cos\theta - \cos\beta)^i (\sin\theta)^j \cos\theta d\theta. \quad (5.13)$$

Using equation (4.9), the author developed the following expression for the average

velocity of a rivulet whose cross-sectional area is  $R^2 \left( \beta - \frac{1}{2} \sin 2\beta \right)$ ;

$$\bar{W}_r = \frac{\tau_i R}{\mu \left( \beta - \frac{1}{2} \sin 2\beta \right)} \left\{ b b_1 f_{20}(\beta) + b b_2 f_{22}(\beta) + \frac{2}{3} b b_3 f_{30}(\beta) + \frac{2}{3} b b_4 f_{32}(\beta) \right\}, \quad (5.14)$$

where the expressions for the coefficients  $b b_i$  and integral functions  $f_{ij}$  are found in Appendix A. The author also developed expressions for the rivulet mass flow rate and average velocity based on Bankoff's [34] work in formulating the minimum thickness criteria of draining liquid films. These expressions are not discussed herein since they

were not employed in the subject simulation. However, Bankoff's work is cited as a valuable study of the criteria associated with the breakdown of liquid films into rivulets.

The local rivulet cell velocity was derived from Al-Khalil's power series expansion relationship for the local velocity. In terms of the non-dimensional coordinates defined in Chapter III, the dimensional local cell velocity becomes

$$w_{i,j} = \frac{\tau_i \delta}{\mu} \{ b_1 Y + b_2 X^2 Y + b_3 Y^2 + b_4 X^2 Y^2 \}, \quad (5.15)$$

where the  $b_i$  coefficients are found in Appendix A.

### **Phase-Change Cell Thermal Resistances**

At the initialization of Mode #2, after the frozen fraction of the bulk rivulet has halted, a boundary is established with relative motion between the stationary solid and the moving liquid at the phase-change interface. Consistent with the enthalpy method formulation employed herein, the application of the non-linear Stefan condition at this boundary is avoided. Remember, the phase-change front is tracked to within a cell volume. Previously, for the stationary rivulet, a cell containing the phase front communicated with its neighbors via thermal conduction. Accordingly, in the runback problem, the effect of the convective interface on the neighboring cells must be included in the connecting thermal resistances. The fact that the convective interface boundary is moving as the phase front propagates, introduces an additional complexity.

The classical convective mechanism associated with the relative motion between a solid stationary surface and a flowing fluid is altered in the case of phase-change. This

alteration is due to the presence of a finite interfacial velocity present at the phase-change interface [35]. From the study of boundary layer control and mass transport, the effect of this interfacial velocity on the thermal transport rate is known to be significant [29,36]. A modified Nusselt number that accounts for the effect of the interfacial boundary velocity associated with phase-change is defined by Pozvonkov et al. [37] as

$$\frac{Nu_p}{Nu_n} \cong \left[ \frac{a_k}{2} \cdot \frac{1}{\left(1 + \frac{1}{k_t}\right)} \right]^{\frac{1}{2}}, \text{ where} \quad (5.16)$$

$$a_k = 3 \cdot \left[ \sqrt{\left(k_t^2 + \frac{4}{3}k_t\right)} - k_t \right]$$

$$k_t = \frac{h_{is}}{c_{p,l}(T_{mp} - T_w)} \text{ (Kutateladze Number)}$$

Also,  $Nu_p$  is the phase-change Nusselt number and  $Nu_n$  is the non-freezing Nusselt number. The non-freezing Nusselt number at the liquid/solid interface is defined using a couette flow approximation and introducing the Brinkman number,  $Br$  [38]. That is

$$Nu_n = 1 + \frac{Br}{2}, \text{ where } Br = Pr \frac{\overline{W}_r^2}{c_{p,l}(T_{mp} - T_w)}. \quad (5.17)$$

From equation (5.16), the new phase-change Nusselt number,  $Nu_p$  is used to define a characteristic thermal conductance for a cell containing the phase-change front. Thus, for those cells that contain the phase-change front during Modes #2 and #3, the thermal resistances are still defined by equations (4.26) and (4.27). However, the author proposes

that the liquid thermal conductivity,  $k_l$ , be replaced by a characteristic thermal energy transport coefficient that embodies the convective mechanism at the phase-change boundary. Therefore, the author proposes scaling the liquid thermal conductivity by the phase-change Nusselt number, wherein the characteristic transport coefficient for a slushy cell becomes

$$k_{ls} \cong f(Nu_p) = Nu_p k_l. \quad (5.18)$$

### **Freezing Rivulet Runback Results**

The results of the freezing shear driven rivulet runback simulation are presented hereafter. Results from the afore mentioned NACA 0012 airfoil test provided an experimental halt distance, which was used to develop the empirical freezing rivulet halting parameter,  $Wi$ . This parameter was then employed in the subsequent numerical simulations. The results of the baseline NACA 0012 airfoil case (hereafter referred to as the NASAIR case) are included in, and compared to, the simulation results. The five experimental simulation cases presented in Chapter III were selected as numerical simulation cases for the runback analysis. They are: cases 1-C, 3-C, 4-C, 7-A and 7-C. Each case has differing initial and environmental conditions. The results of a parametric study of the parameters affecting the halt distance and subsequent downstream runback are also discussed.



### **Phase-Change Front Profiles at Halt**

The phase-change front profile of the leading edge at the bulk rivulet halt distance is shown for each rivulet case in Figures 47-52 below. The frozen fraction of the rivulet front at halt is indicated for each case. The initial and environmental conditions unique to each case are shown in Table 3 below.

Unlike the stationary rivulet simulation cases, the rivulet widths used in the runback rivulet simulation cases correspond to rivulet widths derived from the rivulet mass flow rates used in the experimental study. Scaling rivulet widths of such small dimension (1 mm-2 mm) from video footage, where the resolution was moderate at best, lacked consistency. Therefore, the desire for a more uniform approach led to the calculation of the experimental rivulet widths from the measured mass flow rates. The rivulet mass flow rate is a dependent function of the rivulet radius of curvature,  $R$ , as expressed in equation (5.10). This correlation requires the evaluation of the analytical function,  $F_1(\beta)$ . Thus, the collaboration between the analytical and experimental was

**Table 3.** Rivulet Conditions and Parameters for the Runback Rivulet Cases

<b>Case</b>	<b><math>T_w</math></b>	<b><math>T_{in}</math></b>	<b><math>T_{inf}</math></b>	<b>Ste</b>	<b>rh</b>	<b><math>\beta</math></b>	<b><math>w_r</math></b>	<b><math>U_{inf}</math></b>
	(K)	(K)	(K)	-	%	(deg.)	(mm)	(m/s)
NASAIR	266.5	273.2	266.0	0.0405	100	40	1.7	44.7
1-C	272.9	276.7	271.1	0.00158	80.8	38	1.4	44.7
3-C	270.6	273.4	268.9	0.0155	82.7	38	1.4	45.1
4-C	271.1	273.2	268.7	0.0125	87.2	38	1.0	67.2
7-A	270.7	280.6	269.0	0.0147	83.3	60	1.3	44.7
7-C	270.7	276.3	269.0	0.0147	83.3	60	1.3	44.7

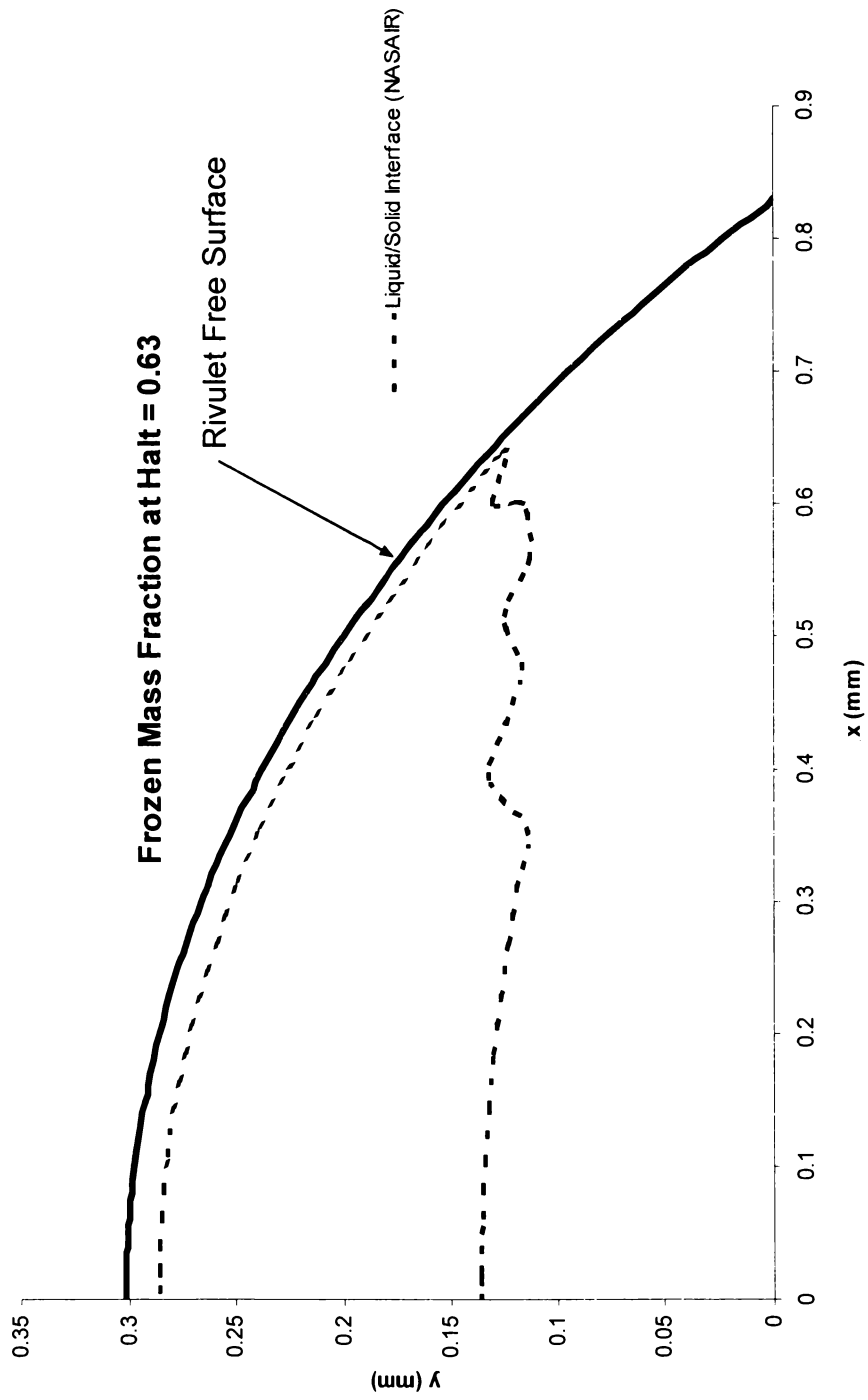


**Figure 47.** Case NASAIR: Predicted Phase-Change Front Profile at Halt

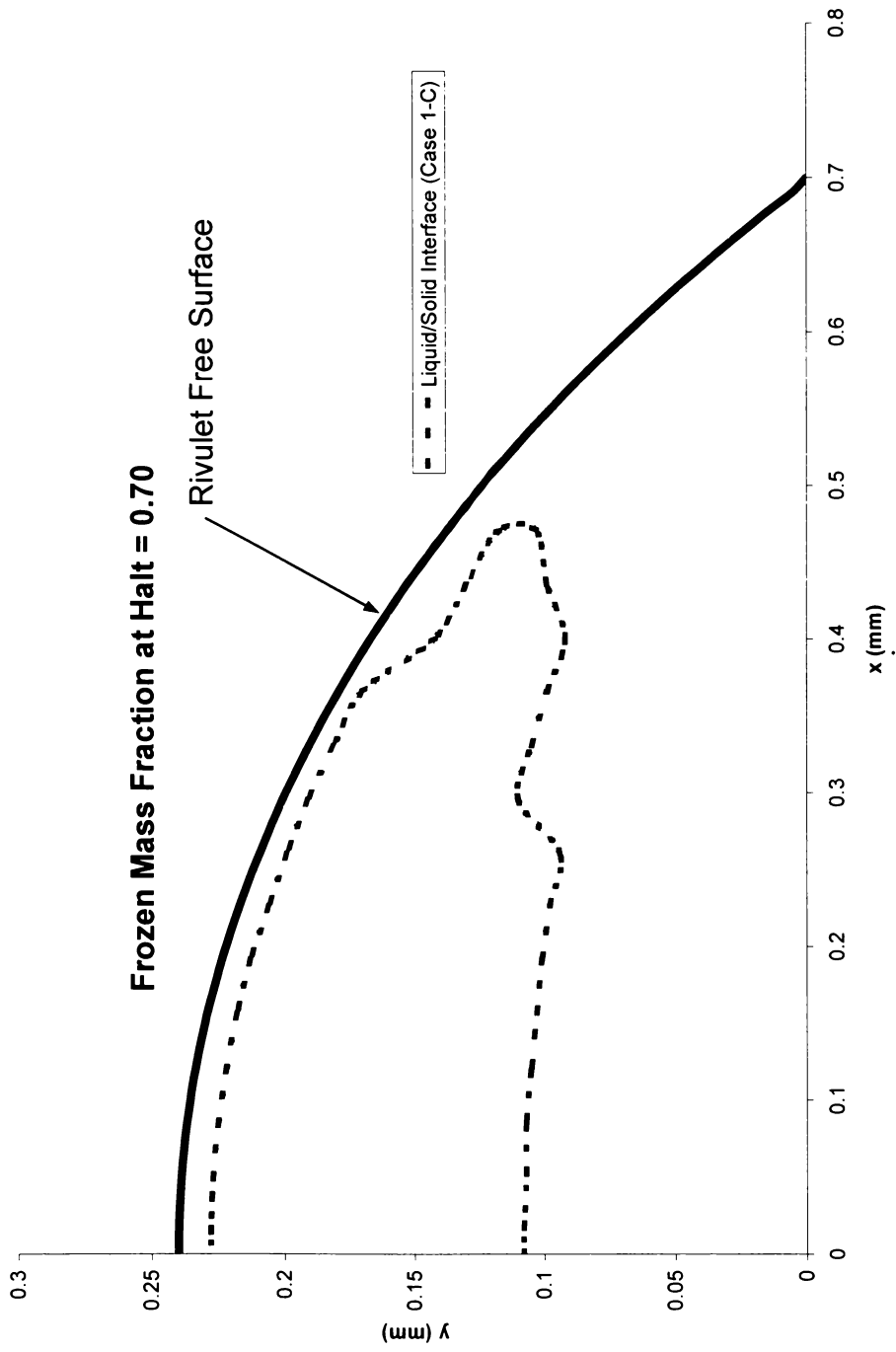


**Figure 48.** Case 1-C: Predicted Phase-Change Front Profile at Halt

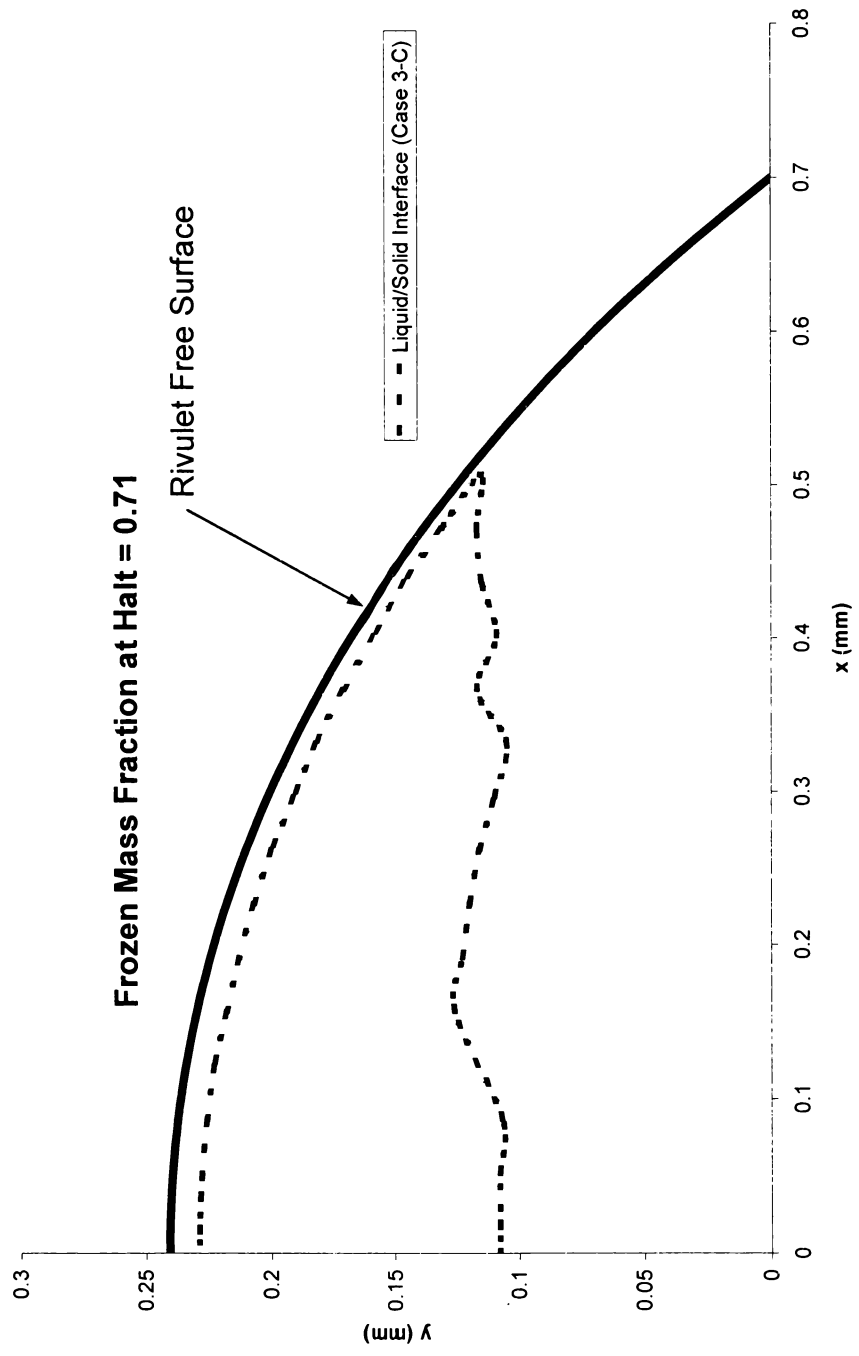


**Figure 49.** Case 3-C: Predicted Phase-Change Front Profile at Halt

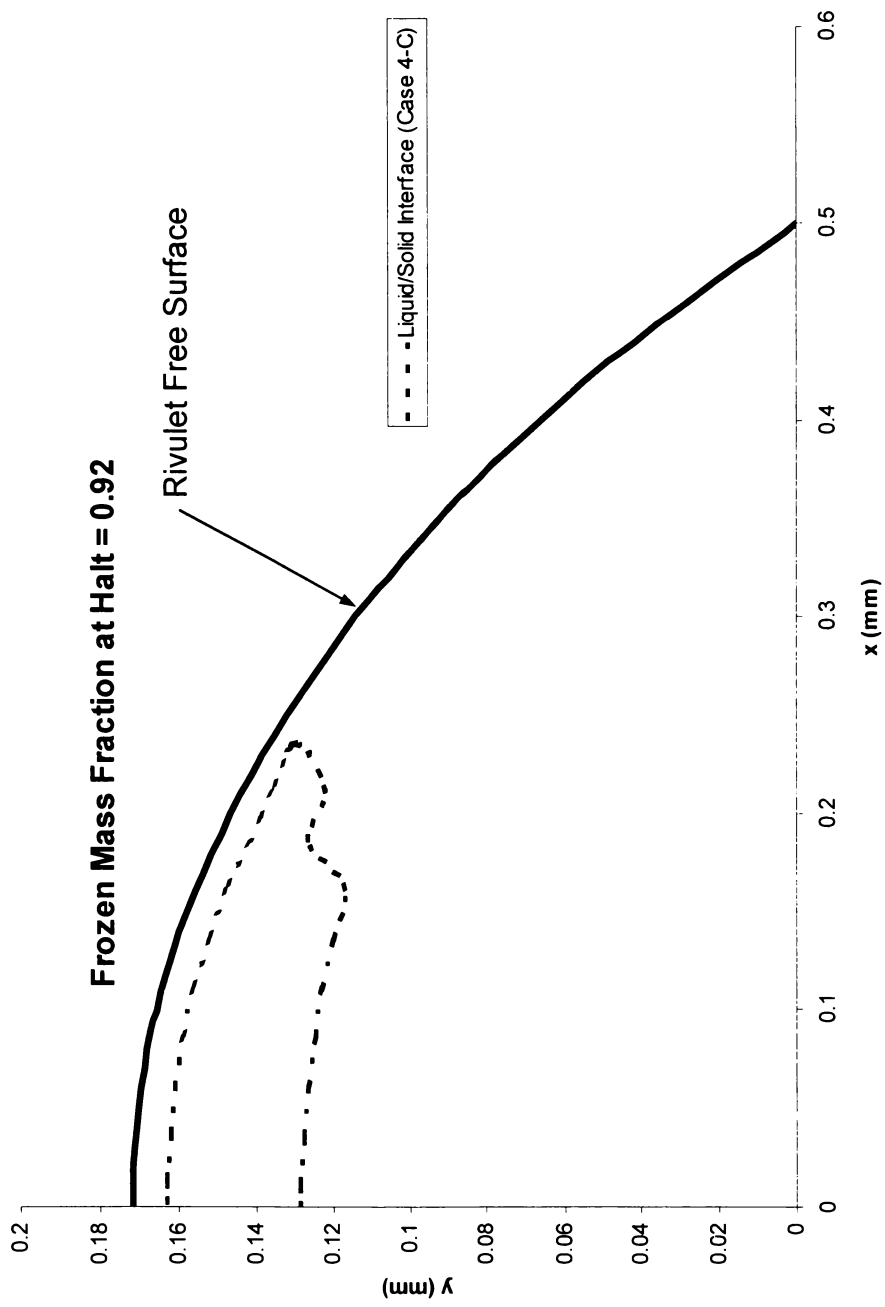


**Figure 50.** Case 4-C: Predicted Phase-Change Front Profile at Halt

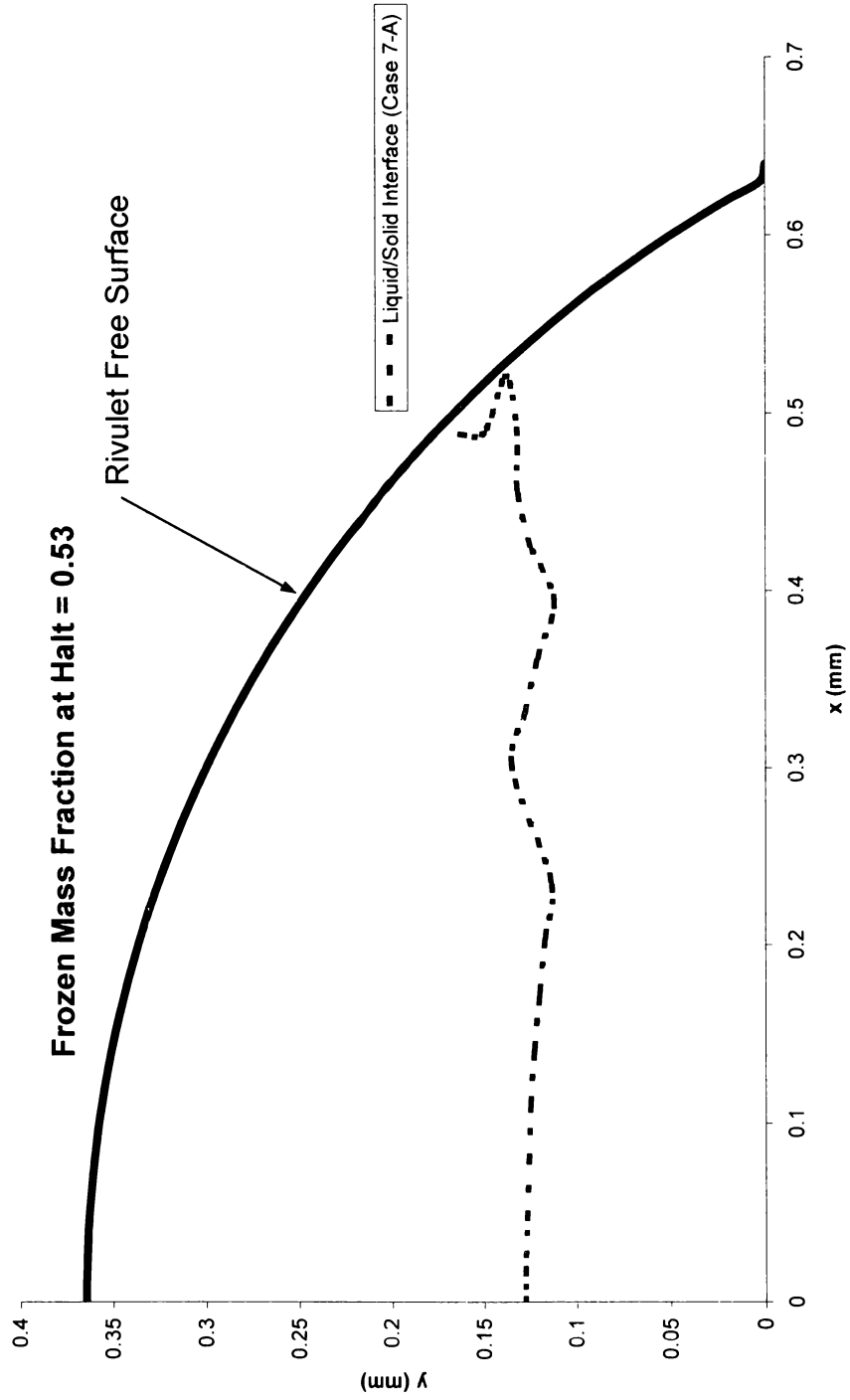


**Figure 51.** Case 7-A: Predicted Phase-Change Front Profile at Halt

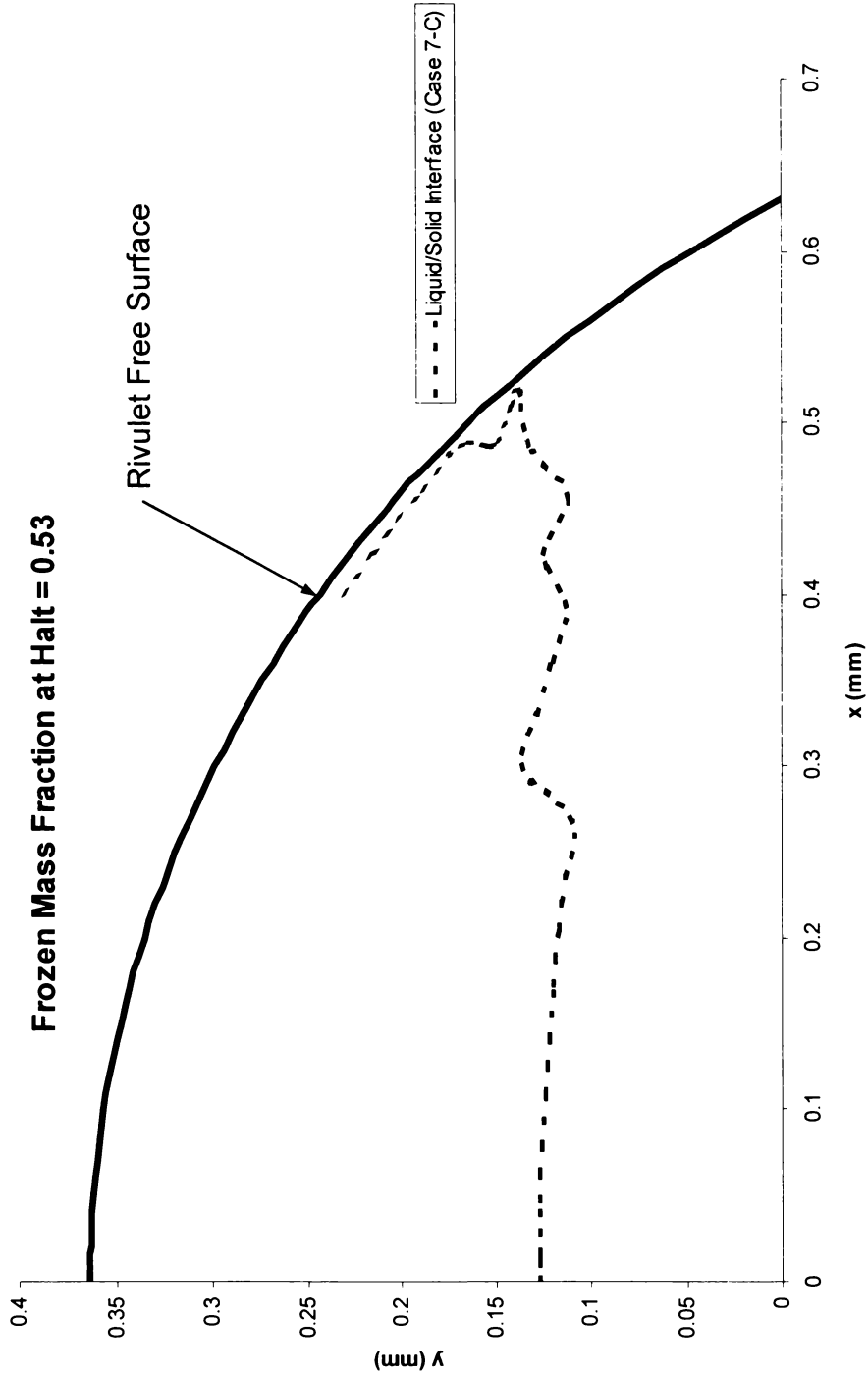


**Figure 52.** Case 7-C: Predicted Phase-Change Front Profile at Halt

necessary. Once  $F_1(\beta)$  was evaluated, the only unknown in equation (5.10) was the rivulet radius of curvature. From the calculated radii of curvature, the various rivulet widths were evaluated using the geometric relationship

$$w_r = 2(R \sin \beta). \quad (5.19)$$

The rivulet widths derived in this fashion were used as inputs in the numerical simulations for the subject test cases.

In each case, there is the primary phase front that propagates from the wall boundary inward toward the free surface. However, as observed in the previous figures, there exists also a secondary phase front that initiates at the free surface boundary. The secondary phase-change front, in each case, lies within the free surface boundary cells. Thus, there is not a completely frozen layer (cell width), or ice crust, at the free surface. The subject simulation assumes that this free surface slushy layer does not alter the momentum transport from the free surface to the primary phase-change front boundary. That is, it is assumed that this slushy layer does not impact the driving shear stress that is transmitted to the primary phase-change interface causing the frozen portion to essentially slide to the halt distance.

The development of an outer frozen shell would add complexities to the rivulet flow dynamics that are beyond the scope of the subject study. The assumption, however, that the bulk rivulet has reached the halt distance prior to any significant ice crust, or shell, being formed at the free surface is a valid one. Generally, the rivulets associated



with the ice accretion on airfoils and engine inlets have an initial temperature near the melting point,  $T_{mp}$ , and the thermal energy conduction into the wall dominates the process of latent heat removal. This phenomenon is seen in the more advanced propagation of the primary phase-change front relative to the secondary phase-change front propagation in Figures 47-52.

### **Rivulet Runback Length**

The results of each simulation case, including the case specific parameters, are summarized in Table 4. The predicted bulk rivulet halt distance ( $L_H$ ), the frozen fraction of the rivulet front at halt and the equivalent-mass rivulet extension ( $L_E$ ), are presented. Note that for cases 1-C, 3-C and 7-A, the conditions are such as to cause a “freeze choke” condition at the rivulet trailing edge (upstream freezing initiation station). Thus, equilibrium in the transport rate of thermal energy exists in the slushy cells and phase-change propagation halts. Thus, the equivalent-mass rivulet runback extensions presented for these cases are the rivulet extensions at the time corresponding to the onset of the “freeze choke” condition. In reality, liquid flow could continue downstream, limited only by the capacity of the upstream source. For cases 4-C, 7-C and NASAIR, the trailing edge completely freezes creating a “flow choke” condition. Herein, a completely frozen rivulet entrance chokes off further liquid flow that would otherwise follow the rivulet path downstream. Additional upstream liquid flow could, however, be deflected around the rivulet by the solid rivulet entrance and take an alternate path downstream, thus widening the wetted area of the original rivulet.

**Table 4: Halt Length, Frozen Fraction and Equivalent Mass Length of Freezing Rivulet Runback for Simulation Cases**

	<b>Rivulet Parameters</b>	<b>Predicted <math>L_H</math></b>	<b>Frozen Mass Fraction at Halt</b>	<b>Predicted <math>L_E</math></b>
<b>NASAIR</b>	$\beta = 40^\circ$ , $T_{in} = 273.15$ K, $T_{inf} = 266.0$ K, $T_w = 266.5$ K, $Ste = 0.0405$	32.1 mm (1.26 in)	0.63	77.7 mm <sup>(2)</sup> (3.1 in)
<b>Case 1-C</b>	$\beta = 38^\circ$ , $T_{in} = 276.7$ K, $T_{inf} = 271.1$ K, $T_w = 272.9$ K, $Ste = 0.00158$	472.5 mm (18.6 in)	0.70	1571.5 mm <sup>(1)</sup> (61.9 in)
<b>Case 3-C</b>	$\beta = 38^\circ$ , $T_{in} = 273.4$ K, $T_{inf} = 268.9$ K, $T_w = 270.6$ K, $Ste = 0.0155$	69.4 mm (2.7 in)	0.71	253.1 mm <sup>(1)</sup> (10.0 in)
<b>Case 4-C</b>	$\beta = 38^\circ$ , $T_{in} = 273.2$ K, $T_{inf} = 268.7$ K, $T_w = 271.1$ K, $Ste = 0.0125$	197.0 mm (7.8 in)	0.90	249.8 mm <sup>(2)</sup> (9.8 in)
<b>Case 7-A</b>	$\beta = 60^\circ$ , $T_{in} = 280.6$ K, $T_{inf} = 268.7$ K, $T_w = 271.1$ K, $Ste = 0.0125$	125.8 mm (5.0 in)	0.53	759.4 mm <sup>(1)</sup> (29.9 in)
<b>Case 7-C</b>	$\beta = 60^\circ$ , $T_{in} = 276.3$ K, $T_{inf} = 269.0$ K, $T_w = 270.7$ K, $Ste = 0.0147$	106.2 mm (4.2 in)	0.53	729.9 mm <sup>(2)</sup> (28.7 in)

1. Equivalent length at Freeze Choke.
2. Equivalent length at Flow Choke.

### Comparison of Predicted and Experimental Results

In Table 5 below, the bulk rivulet halt distances for the five experimental rivulets are compared to the halt distances evaluated using the “runback” numerical simulation for the same governing parameters. The comparative results of Table 5 show reasonably good agreement between the numerical and experimental simulations. Herein, the numerical halt distance predictions vary from the experimental results by an average of 27%, where the range of variation is 0.9% to 45%. Given the complexities associated with the simulation of shear driven freezing rivulet runback, and the necessity to apply simplifying assumptions to render the problem manageable, agreement within 50 % between predicted and measured results is considered reasonable.

**Table 5.** Comparison of Numerical and Experimental Bulk Rivulet Halt Distances

	<b>Rivulet Parameters</b>	<b>Predicted <math>L_H</math></b>	<b>Measured <math>L_H</math></b>	<b>% <math>\Delta L_H</math></b>
<b>Case 1-C</b>	$\beta = 38^\circ$ , $T_{in} = 276.6$ K, $T_{inf} = 271.9$ K, $T_w = 272.7$ K, $Ste = 0.00158$	472.5 mm (18.6in)	489 mm (19.3 in)	3.4
<b>Case 3-C</b>	$\beta = 38^\circ$ , $T_{in} = 273.2$ K, $T_{inf} = 269.7$ K, $T_w = 270.4$ K, $Ste = 0.0155$	69.4 mm (2.7 in)	127 mm (5.0 in)	45.3
<b>Case 4-C</b>	$\beta = 38^\circ$ , $T_{in} = 273.2$ K $T_{inf} = 270.8$ K, $T_w = 270.9$ K, $Ste = 0.0125$	197.0 mm (7.8 in)	140 mm (5.5 in)	40.7
<b>Case 7-A</b>	$\beta = 60^\circ$ , $T_{in} = 280.4$ K, $T_{inf} = 269.8$ K, $T_w = 270.6$ K, $Ste = 0.0125$	125.8 mm (5.0 in)	127 mm (5.0 in)	0.94
<b>Case 7-C</b>	$\beta = 60^\circ$ , $T_{in} = 276.2$ K, $T_{inf} = 269.8$ K, $T_w = 270.6$ K, $Ste = 0.0147$	106.2 mm (4.2 in)	185 mm (7.3 in)	42.6

## **Parametric Study Results**

A parametric study was performed to determine which case specific environmental parameters have the greatest impact on the runback halt length and equivalent runback length. The study was constrained by four rivulet sizes, wherein the rivulet cross-sectional areas were determined by the rivulet widths and contact angles shown in Table 6 below. Thus, the parametric cases were denoted as  $A_{r\_1}$ ,  $A_{r\_2}$ ,  $A_{r\_3}$  and  $A_{r\_4}$  according to their cross-sectional area. The parameters varied were threefold, namely;  $T_w$ ,  $T_{inf}$  and  $U_{inf}$ . Certainly this selection of parameters is not exhaustive, however, it does represent a subset that has a marked impact on the runback halt length. The baseline values, when two of these parameters are held constant while the third varies, are  $T_w = 268.15$  K,  $T_{inf} = 268.0$  K and  $U_{inf} = 44.7$  m/s (100 mph). The initial uniform temperature of each rivulet was  $T_{in} = T_{mp} = 273.15$  K, which is physically reasonable for rivulet runback in glaze ice accretion conditions. Thus, the freezing proceeds as a “One-Phase Stefan Problem”, wherein thermal energy is transported only through the solid phase as discussed in Chapter II. The parametric range of these parameters and their associated results are presented in Tables 6-8.

The parametric trends distinguishable from the tabular data are captured pictorially in Figures 53-55. Not all of the parametric data sets were amenable to plotting on the same axis set. However, the trends are well established, and one can easily make a mental link from the tabular data to an associated curve and its position relative to the plotted curves.

**Table 6:** Parametric Results for the Wall Temperature,  $T_w$

	Ar_1: $w_r = 1.0$ mm, $\beta = 30^\circ$			Ar_2: $w_r = 1.5$ mm, $\beta = 40^\circ$			Ar_3: $w_r = 2.5$ mm, $\beta = 50^\circ$			Ar_4: $w_r = 3.0$ mm, $\beta = 60^\circ$		
	$L_H$ (mm)	$L_E$ (mm)	$F_f$	$L_H$ (mm)	$L_E$ (mm)	$F_f$	$L_H$ (mm)	$L_E$ (mm)	$F_f$	$L_H$ (mm)	$L_E$ (mm)	$F_f$
$T_w$ (K)												
260	5.5	7.7	0.84	15.7	34.0	0.66	5.4	175.0	0.27	0.32	533.9	0.10
265	8.7	12.1	0.84	24.9	53.4	0.66	8.6	271.6	0.27	0.40	826.3	0.10
270	21.0	29.3	0.84	61.3	129.0	0.66	21.4	628.4	0.27	0.81	1894.2	0.10
273	164.2	221.4	0.84	653.5	1077.8	0.66	354.0	3527.6	0.27	2.0	9054.6	0.10

**Table 7.** Parametric Results for the Freestream Temperature,  $T_{inf}$

		$A_{r\_1}$ : $w_r = 1.0$ mm, $\beta = 30^\circ$			$A_{r\_2}$ : $w_r = 1.5$ mm, $\beta = 40^\circ$			$A_{r\_3}$ : $w_r = 2.5$ mm, $\beta = 50^\circ$			$A_{r\_4}$ : $w_r = 3.0$ mm, $\beta = 60^\circ$		
		$L_H$ (mm)	$L_E$ (mm)	$F_f$	$L_H$ (mm)	$L_E$ (mm)	$F_f$	$L_H$ (mm)	$L_E$ (mm)	$F_f$	$L_H$ (mm)	$L_E$ (mm)	$F_f$
$T_{inf}$ (K)	260	13.3	18.6	0.84	38.8	81.7	0.66	13.7	399.7	0.27	0.57	1206.7	0.10
265	13.5	19.0	0.84	39.3	83.4	0.66	13.7	413.2	0.27	0.57	1250.5	0.10	
270	13.8	19.4	0.84	39.9	85.1	0.66	13.6	427.4	0.27	0.65	1297.1	0.10	
273	14.0	19.6	0.84	40.2	86.3	0.66	13.9	437.0	0.27	0.65	1327.5	0.10	

**Table 8:** Parametric Results for Freestream Velocity,  $U_{inf}$

		Ar_1: $w_r = 1.0$ mm, $\beta = 30^\circ$			Ar_2: $w_r = 1.5$ mm, $\beta = 40^\circ$			Ar_3: $w_r = 2.5$ mm, $\beta = 50^\circ$			Ar_4: $w_r = 3.0$ mm, $\beta = 60^\circ$		
		$L_H$ (mm)	$L_E$ (mm)	$F_f$	$L_H$ (mm)	$L_E$ (mm)	$F_f$	$L_H$ (mm)	$L_E$ (mm)	$F_f$	$L_H$ (mm)	$L_E$ (mm)	$F_f$
$U_{inf}$ (m/s)													
25		0.60	2.6	0.53	0.014	16.0	0.10	0.086	146.9	0.10	0.22	461.0	0.10
35		5.0	8.6	0.74	6.4	35.4	0.47	0.12	265.6	0.10	0.41	832.5	0.10
55		27.3	35.3	0.89	110.6	175.2	0.77	190.9	777.7	0.50	52.0	1887.7	0.24
65		44.6	55.3	0.92	213.3	300.1	0.83	636.8	1423.3	0.63	575.1	3033.8	0.44

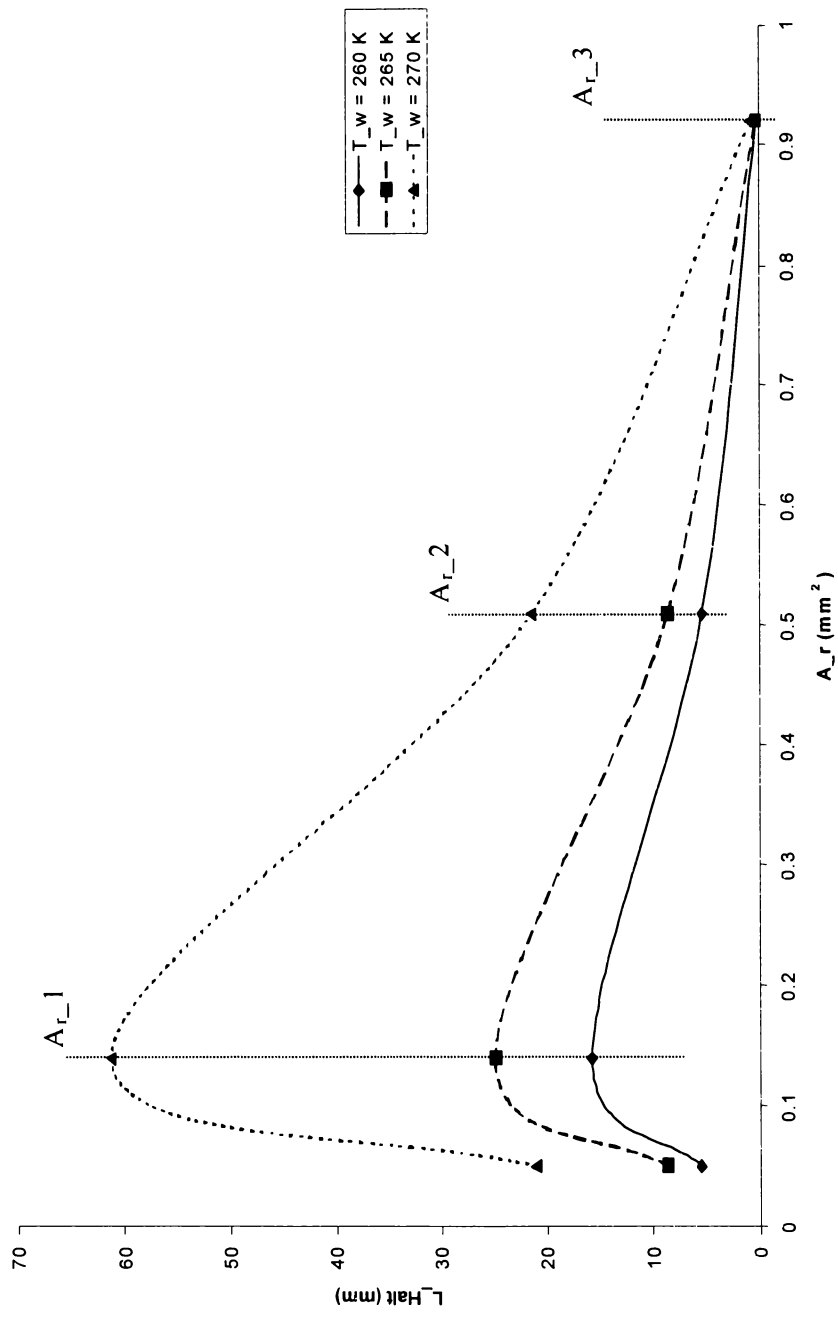


**Figure 53:** Parametric Results for the Wall Temperature,  $T_w$



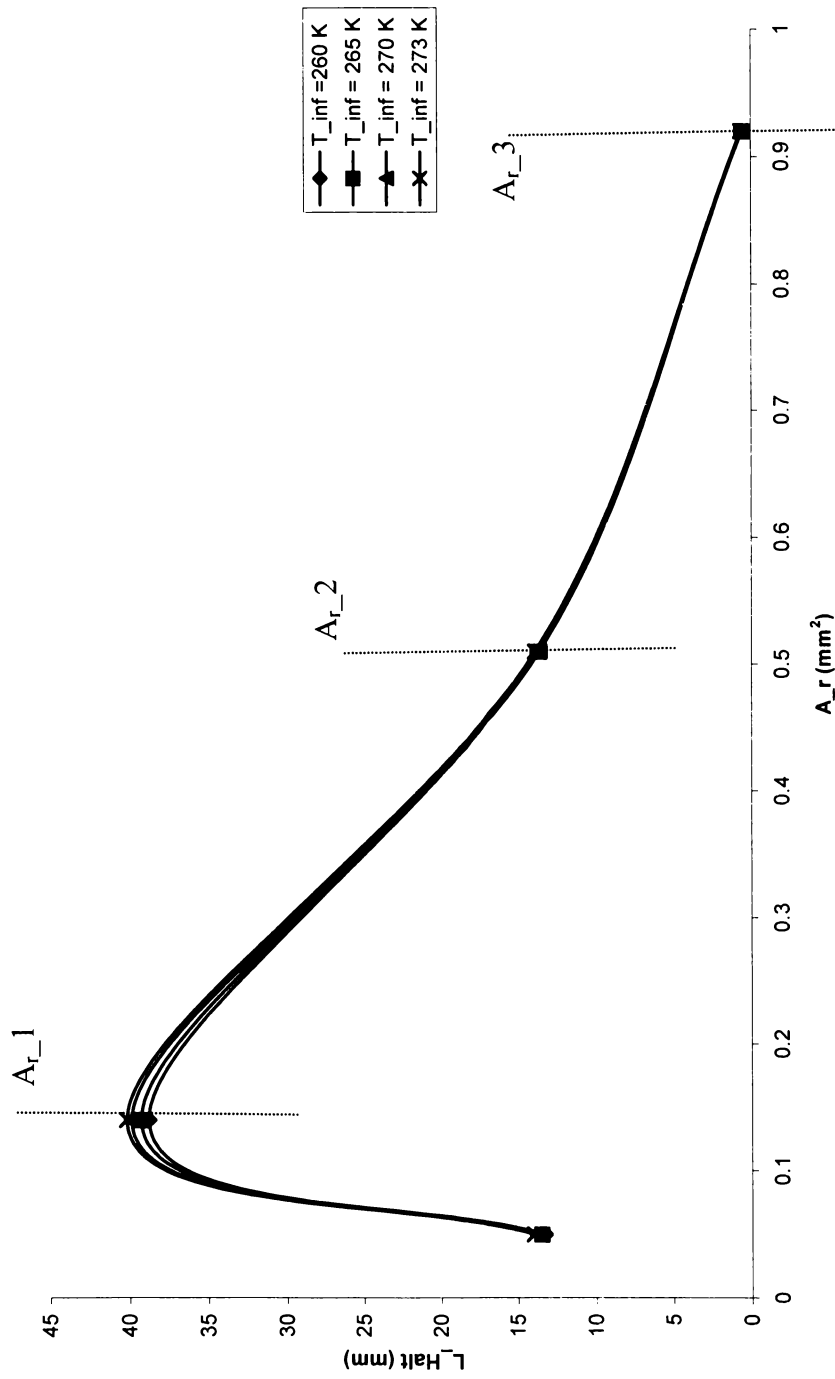


**Figure 54:** Parametric Results for the Freestream Temperature,  $T_{inf}$

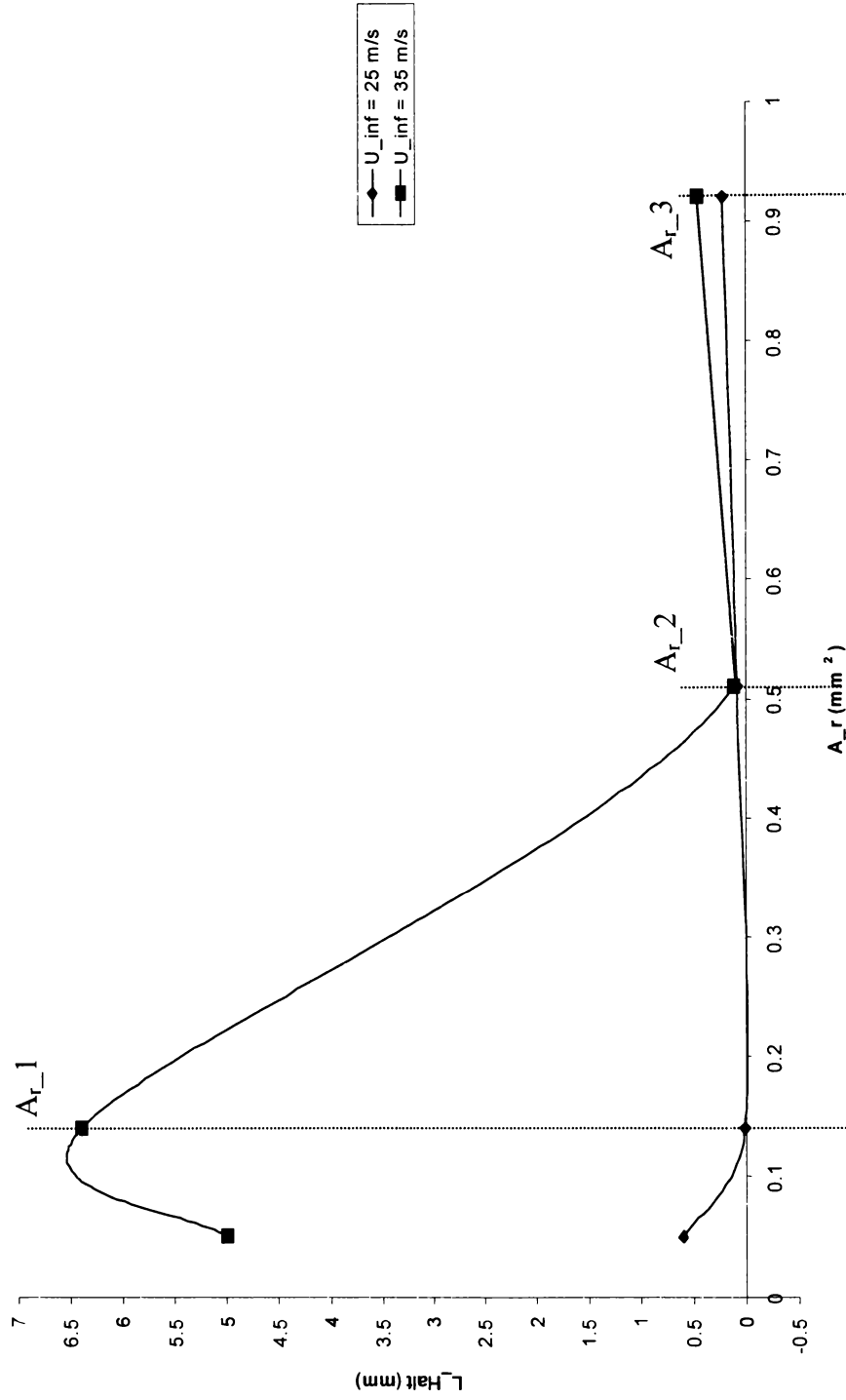


**Figure 55:** Parametric Results for the Freestream Velocity,  $U_{inf}$

## Conclusions

Figures 53 and 54 and Tables 6 and 7 reveal a local maximum in halt distance associated with the  $A_2$  rivulet cross-section. This trend is reasonable, given that the halt criterion is based on the ratio of the shear force at the phase-change interface and the sliding friction force at the wall boundary. The surface area over which the interfacial shear force acts varies as the phase front propagates, while the surface area over which the sliding friction force acts is constant for a given rivulet size. The resultant effect of the interplay between these forces from one rivulet size to another, and during the freezing process is the substance of the tabular data. For a given rivulet, the variation in halt distance is slight when  $T_{inf}$  is the parametric parameter. Conversely, the halt distance varies significantly as  $T_w$  varies. Note, that in Tables 6 and 7, for a given rivulet, the frozen fraction does not change with the changing parametric parameter. This is because the frozen fraction is related to the liquid mass fraction, which is used to define the halting criterion (see equation 5.1). When either the wall or freestream temperature is the parametric variable, the frozen fraction of the rivulet leading edge at halt decreases monotonically with increasing rivulet cross-sectional area. Accordingly, the equivalent runback length increases monotonically as the rivulet cross-sectional area increases. Clearly, the wall temperature is a major player in the resultant halt and equivalent rivulet runback distances in freezing shear driven rivulet flow.

The effect of variation in freestream velocity on the halt length and runback equivalent length is best captured in Table 8. Figure 55 shows the curvature differences for the halt length as a function of rivulet cross-sectional area for two freestream

velocities. An evident trend is the monotonically increasing halt and equivalent lengths for a given rivulet size with variation of freestream velocity. As the rivulet size increases, the effect of variations in freestream velocity on the bulk rivulet halt distance is more significant.

### Summary

A summary of the primary features of the parametric study is presented below.

- $A_r$  – constant
  - As  $T_w$  increases –  $L_H$  increases monotonically (significantly)
  - As  $T_{inf}$  increases -  $L_H$  increases monotonically (slightly)
  - As  $U_{inf}$  increases -  $L_H$  increases monotonically (markedly)
  - As  $U_{inf}$  increases -  $F_r$  increases
- $T_w$  or  $T_{inf}$  - constant
  - As  $A_r$  increases -  $L_H$  obtains a maximum
  - As  $A_r$  increases --  $L_E$  increases
  - As  $A_r$  increases –  $F_r$  decreases
- $U_{inf}$  - constant
  - As  $A_r$  increases -  $L_H$  obtains local maxima and minima (difficult to resolve with few data points)
  - As  $A_r$  increases –  $L_E$  increases
  - As  $A_r$  increases –  $F_r$  decreases

## CHAPTER VI

### CONCLUDING REMARKS

The development and validation of a numerical simulation of freezing shear driven rivulets was the substance of this work. A discussion of the icing environment, including fundamental phenomena associated with ice accretion was presented. Conditions associated with the establishment of a “runback” zone, wherein thin liquid films are want to breakdown and rivulet flow emerges, were highlighted. The utility of the enthalpy method formulation of the Stefan Problem was presented as a robust and physically sound means of capturing the phase-change front propagation.

The development of the freezing rivulet runback simulation incorporated two primary models; namely, the “stationary” freezing rivulet model and the “runback” freezing rivulet model. The former provided a simpler methodology by which the modeling of the fundamental physics of the Stefan problem was benchmarked. Additionally, the utility of the enthalpy method formulation coupled with the Gauss-Seidel numerical technique was established using the “stationary” simulation. The “stationary” model was modified by addition of a convective enthalpy term to simulate the thermal energy transport associated with the motion of a traveling rivulet front. From this modified “stationary” freezing rivulet model; the “runback” model was developed. The “runback” model attempted to capture the physics of freezing shear driven rivulet runback by dividing the observed phenomena into freezing runback modes. These modes encompass the freezing runback problem, including the initialization of phase-change, subsequent runback with a frozen fraction to the point of halt, complete freeze of the

rivulet front and the complete freeze, or freeze choke, of the rivulet trailing edge (station of phase-change initiation). An equivalent mass rivulet extension length was also established using conservation of mass and an associated rivulet size to identify the continuation of rivulet or coalesced beaded flow downstream of the bulk rivulet. An empirical based non-dimensional parameter was formulated which established the criterion for the “bulk rivulet” halt and associated runback distance.

A parametric study revealed that the bulk freezing rivulet halt distance for a given rivulet size was markedly affected by the substrate, or wall, temperature. Likewise, the freestream velocity had a significant impact on runback distance before any frozen fraction was deposited. Both of these parametric parameters have a primary influence on the empirical halting parameter,  $W_i$ . The former impacts the thermal energy transfer potential at the wall, and the latter impacts the momentum transfer potential at the rivulet free surface. By holding the environmental parameters constant, and changing the rivulet size with the contact angle and the rivulet width, a rivulet size was revealed that resulted in a maximum bulk rivulet halt distance.

An experimental simulation conducted in the Icing Research Tunnel (IRT) at NASA Glenn provided a set of test cases from which bulk rivulet halt distances were ascertained and compared with the numerical simulations. The correlation between numerical and experimental simulations was reasonably good, suggesting that the physics-based numerical models are well formulated and applicable. Close observations of the experimental test behavior were applied to the numerical models to enhance their utility and improve the overall performance of the freezing shear driven rivulet runback

code. Despite the subjectivism inherent in the experimental observations, a solid collection of freezing rivulet runback phenomena was obtained on video and employed to guide and validate the subject numerical simulation.

Then subject study culminates in a foundation work from which further investigations and model enhancements related to the freezing of shear driven rivulet runback can be motivated. Indeed, parametric studies of rivulet growth can now be performed to understand the general behavior of rivulets under a wide range of humidity, freestream velocity and temperature conditions. The “runback” model provides the basis for a freezing rivulet runback module that could be incorporated into an ice accretion code. A few recommendations for consideration in further studies of the freezing rivulet runback problem are detailed below.

### **Recommendations**

The complex phenomena and accompanying short time scales associated with freezing rivulet runback speak of a need for further investigations. A more detailed investigation of the aerodynamic interactions with the rivulet structure is certainly warranted. This would include gaining further understanding of the role aerodynamic forces play in the instability and subsequent breakdown of rivulet flow into beads as the rivulet runs back and freezes, and also on rivulet shapes and geometries. Further investigations would also include obtaining insights into the rivulet shape as a function of liquid freezing rates during runback. As the rivulet structure freezes from the wall toward the free surface during runback, the liquid/solid interface transitions from one of

liquid/wall substrate to a liquid/ice interface. An important undertaking is to obtain insight into the interfacial phenomena between the solid and its melt, and to ascertain the resultant effects on the rivulet shape and associated motion. Therefore, questions such as whether any significant alteration in the rivulet shape by a change in surface tension values at the solid/gas interface and the solid/ liquid interface can be posed and addressed numerically.

Finally, a deeper understanding of the details of the freezing of rivulet runback downstream of the bulk rivulet front halt would be desirable. The author recommends a series of experimental simulations with rivulets at an initial temperature near the phase-change temperature. Herein, additional data points could be obtained for the bulk rivulet front halt distance database, as well as, details of the subsequent downstream flow phenomena and travel extent.



## **LIST OF REFERENCES**

## LIST OF REFERENCES

1. Lankford, D. W., "The Improved K-ICE Model for Multiphase Flow Including Ice Accretion," Sverdrup Technology, Inc., Memorandum, Arnold Air Force Base, TN, September 30, 1996.
2. Wright, W. B., "Users Manual for the Improved NASA Lewis Ice Accretion Code LEWICE 1.6," NASA CR-198355, June 1995.
3. Jones, R. R. III, and Lankford, D. W., "Demonstration of Physics Based Models for the Simulation of Airbreathing Propulsion System Ice Ingestion," Sverdrup Technology, Inc./AEDC Group, Arnold Air Force Base, TN, November, 1995.
4. Hall, E. J., and Delaney, R. A., "Investigation of Advanced Counterrotation Blade Configuration Concepts for High Speed Turboprop Systems," NASA CR-187126, January 1993.
5. DeAngelis, B. C., and Loth, E., "Computations of Turbulent Droplet Dispersion for Wind Tunnel Icing Tests," AIAA Paper 96-0634, Jan. 1996.
6. Lankford, D. W., "Integrated Modeling and Test Environments Computational Technology Area," Sverdrup Technology, Inc./AEDC Group, Executive Summary, Arnold Air Force Base, TN.
7. Macklin, W. C., and Payne, G. S., "A Theoretical Study of the Ice Accretion Process," Quarterly Journal of the Royal Meteorological Society, Vol. 93, 1967, pp. 195-213.
8. Lozowski, E. P., and Gates, E. M., "On the Modeling of Ice Accretion," Freezing and Melting Heat Transfer in Engineering, Chapter 19, Hemisphere Publishing Corp., New York, 1991, pp. 616-660.
9. Hansman, J. R., Yamaguchi, K., Berkowitz, B., and Potapczuk, M., "Modeling of Surface Roughness Effects on Glaze Ice Accretion," Journal of Thermophysics, Vol. 5, No. 1, 1991, pp. 54-60.
10. Yamaguchi, K., and Hansman, R. J., "Heat Transfer on Accreting Ice Surfaces," Journal of Aircraft, Vol. 29, No. 1, 1992, pp. 108-113.
11. Yamaguchi, K., Hansman, R. J., and Kazmierczak, M., "Deterministic Multi-Zone Ice Accretion Modeling," AIAA Paper 91-0265, Jan. 1991.

12. Hansman, R. J., "Analysis of Surface Roughness Generation in Aircraft Ice Accretion," AIAA Paper 92-0298, Jan. 1992.
13. Hansman, R. J., and Turnock, S. R., "Investigation of Surface Water Behavior During Glaze Ice Accretion," Journal of Aircraft, Vol. 26, No. 2, 1989, pp. 140-147.
14. Hedde, T., and Guffond, D., "Improvement of the ONERA 3D Icing Code, Comparison with 3D Experimental Shapes," AIAA Paper 93-0169, Jan. 1993.
15. NASA Glenn Research Center, Icing Research Branch Archives, Lewis Field, Cleveland, Ohio.
16. Al-Khalil, K. M., "Numerical Simulation of an Aircraft Anti-Icing System Incorporating a Rivulet Model for the Runback Water," Ph.D. Thesis, The University of Toledo, Jun. 1991.
17. Al-Khalil, K. M., Keith, T. G., Jr., and DeWitt, K. J., "Development of an Improved Model for Runback Water on Aircraft Surfaces," AIAA Paper 92-0042, Jan. 1992.
18. Mikielewicz, J., and Moszynski, J. R., "Breakdown of a Shear Driven Liquid Film," Pol. Akad. Nauk., Prace Instytutu Maszyn Przeplywowych, No. 66, 1975, pp.3-11.
19. Landau, L.D., and Lifshitz, E.M., Fluid Mechanics, Course of Theoretical Physics, Vol. 6, Pergamon Press, Oxford, 1959, pp. 230-237.
20. Alexiades, V., and Solomon, A.D., Mathematical Modeling of Melting and Freezing Processes, Hemisphere Publishing Corporation, 1993.
21. Libby, P.A., and Chen, S., "The Growth of a Deposited Layer on a Cold Surface," International Journal of Heat and Mass Transfer, Pergamon Press, Oxford, 1965, Vol. 8, pp. 395-402.
22. Lapadula, C., and Mueller, W. K., "Heat Conduction with Solidification and a Convective Boundary Condition at the Freezing Front," International Journal of Heat and Mass Transfer, Pergamon Press, Oxford, 1966, Vol. 9, pp. 702-704.
23. Voller, V., and Cross, M., "Accurate Solutions of Moving Boundary Problems Using the Enthalpy Method," International Journal of Heat and Mass Transfer, Pergamon Press, Oxford, 1981, Vol. 24, pp. 545-556.
24. Soeder, R.H, et al., "NASA Lewis Icing Research Tunnel User Manual," NASA Technical Memorandum 107159, June 1996.
25. Davies, J.T. and Rideal, E.K., Interfacial Phenomena, 2<sup>nd</sup> Edition, Academic Press, New York, 1963.

26. Video footage of Thermal Code Validation Test #1 conducted in the Icing Research Tunnel (IRT) at NASA Glenn Research Center, April 1996. Received from William Wright, NYMA, Inc., December 4, 1997.
27. Incropera, F.P., and DeWitt, D.P., Introduction to Heat Transfer, Second Edition, John Wiley & Sons, Inc., New York, 1990, pp. 360-371.
28. White, F.M., Heat Transfer, Addison-Wesley Publishing Company, Massachusetts, 1984, pp. 306-307.
29. Bird, R.B., Stewart, W.E., and Lightfoot, E.N., Transport Phenomena, John Wiley & Sons, Inc., New York, 1960.
30. Willbanks, C.E., and Schulz, R.J., "Analytical Study of Icing Simulation for Turbine Engines in Altitude Test Cells," Journal of Aircraft, Vol. 12, No.12, 1975, pp. 960-966.
31. Burden, R.L. and Faires, J.D., Numerical Analysis, 5<sup>th</sup> Edition, PWS Publishing Company, Boston, 1993, pp. 160-161.
32. Kneile, K., "Private Communication", Arnold Engineering Development Center, Tullahoma, Tennessee.
33. Dorsey, N.E., Properties of Ordinary Water-Substance, Reinhold Publishing Corporation, New York, 1940.
34. Bankoff, S.G., "Minimum Thickness of a Draining Liquid Film," International Journal of Heat and Mass Transfer, Pergamon Press, Great Britain, Vol. 14, 1971, pp. 2143-2146.
35. Yen, Y.C. and Tien, C., "Laminar Heat Transfer Over a Melting Plate, the Modified Leveque Problem," Journal of Geophysical Research, Vol. 68, No. 12, June 1963, pp. 3673-3678.
36. Schlichting, H., Boundary Layer Theory, Pergamon Press, London, 1955.
37. Pozvonkov, F.M., Shurgalski, E.F. and Akselrod, L.S., "Heat Transfer at a Melting Flat Surface Under Conditions of Forced Convection and Laminar Boundary Layer," International Journal of Heat and Mass Transfer, Pergamon Press, Great Britain, Vol. 13, 1970, pp. 957-962.
38. White, F.M., Viscous Fluid Flow, McGraw-Hill, Inc., New York, 1991, pp. 108-109.

## **APPENDIX**

## APPENDIX

### COEFFICIENTS AND INTEGRAL FUNCTIONS - ANALYTICAL RIVULET VELOCITY FIELD

An analytical, closed form, solution for the velocity field of a traveling rivulet was developed by Al-Khalil [16]. In the subject simulation of the freezing of shear driven rivulets, this analytical velocity field is employed. Expressions for the average and local rivulet velocities are contained in this work. Thus, for completeness, the coefficients and integral functions associated with these velocity relationships are included below.

$$a = \beta_d \text{ (degrees)}$$

$$b = \beta_r \text{ (radians)}$$

#### Coefficients

$$b_1 = 0.99444 + 1.3522E-3*a - 1.58975E-4*a^2 + 1.1778E-6*a^3$$

$$b_2 = (1.80005 - 6.6927E-3*a + 1.29684E-3*a^2 - 4.047837E-5*a^3 + 6.442231E-7*a^4 - 4.071E-9*a^5) * (1. - \cos(b))^2$$

$$b_3 = (0.2177 + 1.7861E-3*a + 1.6869E-4*a^2 - 2.14556E-6*a^3) * (1. - \cos(b))$$

$$b_4 = (-11.70748 + 0.0146353E-3*a + 7.02226E-3*a^2 - 1.44743E-4*a^3 + 9.29536E-7*a^4) * (1. - \cos(b))^3$$

$$bb_1 = b^1$$

$$bb_2 = b^2/(1 - \cos(b))^2$$

$$bb_3 = b^3/(1 - \cos(b))$$

$$bb_4 = b^4/(1 - \cos(b))^3$$

### **Integral Functions**

$$f_{20} = (-1./3.)*\sin(b)^3 + \sin(b) - b*\cos(b)$$

$$f_{22} = (1./16.)*\cos(b)*\sin(4b) - (1./5.)*\sin(b)^5 + (1./3.)*\cos(b)^2*\sin(b)^3 + \\ (1./3.)*\sin(b)^3 - (1./4.)*b*\cos(b)$$

$$f_{30} = (-1./4.)*\cos(b)^3*\sin(b) - (3./16.)*\sin(2b) - (3./2.)*b*\sin(b)^2 + (15./8.)*b$$

$$f_{32} = (-3./32.)*\cos(b)^2*\sin(4b) - (1./64.)*\sin(4b) + (1./48.)*\sin(2b)^3 + (3./5.)*\cos(b)* \\ \sin(b)^5 - (1./3.)*\cos(b)^3*\sin(b)^3 - \cos(b)*\sin(b)^3 + (3./8.)*b*\cos(b)^2 + (1./16.)*b$$

## VITA

The author was born in Sunset, Utah on July 17, 1964. At age ten, he and his family moved from Sunset, Utah to neighboring Roy, Utah, where he continued his formal public schooling; graduating from Roy High School in 1982. He then enrolled at Utah State University pursuing a Bachelor's degree in Mechanical Engineering. After his first year at USU, he accepted a call to serve a mission for The Church of Jesus Christ of Latter Day Saints to labor in the New York New York City Mission (Greek speaking) from 1983 to 1985. Upon returning from missionary labors, he resumed academic studies at USU and met a wonderful young lady, also attending USU. He and Janell Sorensen were married in June 1988 in the Logan Temple of The Church of Jesus Christ of Latter Day Saints. In 1989 he graduated with a Bachelor's degree in Mechanical Engineering and a minor in Modern Greek. He continued studies at USU and received a Master's degree in Mechanical Engineering in 1991. After working two and a half years at Lockheed in Fort Worth, TX, he entered the PhD program in Mechanical Engineering at the University of Tennessee Space Institute in August of 1994.

The author is presently employed at United Defense L.P., Armament Systems Division in Minneapolis, Minnesota, wherein he works in the Fluid and Thermal Sciences Group of the Applied Mechanics Department. He and his wife Janell have six wonderful boys: Stuart, Sean, Dallin, Derrick, Jacob and Joseph.